The Characteristic Properties of GeO_2 Monolayer on SiO_2, and the Structure and Performance of the Monolayer-Supported Rh Catalyst

（ゲルマニウム酸化物薄層の特性と
それを担体として用いた担持Rh触媒の構造と触媒作用）

奥村　和

学位論文

The Characteristic Properties of GeO_2 Monolayer on SiO_2, and the Structure and Performance of the Monolayer-Supported Rh Catalyst

（ゲルマニウム酸化物薄層の特性とそれを担体として用いた担持Rh触媒の構造と触媒作用）

平成8年12月博士（理学）申請

東京大学大学院理学系研究科
化学専攻
奥村　和

Contents

Chapter 1 General Introduction

This thesis deals with the study on GeO_2/SiO_2 (GeO_2 submonolayer supported on SiO_2), its interaction with Rh, and catalytic reactions. The whole investigation was performed in the laboratory of Professor Yasuhiro Iwasawa in Department of Chemistry, Graduate School of Science, The University of Tokyo.

Chapter 1 is the introduction, where background of this thesis is described. Chapter 2 is the preparation and characterization of GeO_2/SiO_2. The way of GeO_2 deposition on SiO_2 is mentioned. Chapter 3 treats with the structural change of Rh and Ge in Rh supported GeO_2/SiO_2 during reduction and oxidation treatments. Reversible formation of RhGe alloy or GeO_2 submonolayer and the comparison with the use of bulk-SiO_2 or GeO_2 support are explained. Chapter 4 deals with the study on the relation between the reduction temperature and the structure of $Rh/GeO_2/SiO_2$ catalyst, where Rh carbonyl complex, $Rh_6(CO)_{16}$ was used as precursor for the $Rh/GeO_2/SiO_2$ catalyst. And its application to the catalytic reaction. Chapter 5 describes the general conclusions of this thesis.

In this study, GeO_2 submonolayer was prepared on SiO_2 surface, and applied as catalyst support. Several points can be given on the advantages of the use of monolayer oxide as catalyst support. Firstly, it becomes easy to extract the structural information of catalyst surface compared with bulk oxides. Because it can be regarded as the substitute of the surface of bulk metal oxide, if the monolayer metal oxide has the same chemical property or local structure as bulk metal oxide. The subtle change on monolayer support surface during catalytic reaction, pretreatment or chemisorption can be easily detected on the monolayer support without intervention of inside portion as bulk support. Especially, XAFS spectroscopy is suitable for application to such systems, because it can measure only the averaged structure of a specific element owing to the property of bulk technique.

Second, appearance of new catalytic behavior or generation of novel catalyst component is

expected, which cannot find out on bulk metal oxide support, because sometimes monolayer oxides possess unique and different character form that of bulk oxides, such as generation of acidity on interface between monolayer oxides and connected support inorganic oxide. To achieve the above purpose, the structural change of support surface as well as metal supported on it was followed on behalf of the GeO_2 monolayer/SiO_2 support during interaction with Rh particles.

Finally, I have applied this metal supported on monolayer oxide to the catalytic reaction to make good use of the advantageous character of the monolayer support. This study may serve for the understanding of the support role in catalyst.

1-1 Synthesis, Characterization of Atomic Layer Oxides and Application to Catalysts

Whereas sometimes the characterization of the structure of the usual supported metal oxide is complicated and difficult because the supported oxide simultaneously has several different structures and chemical states, atomic layer oxide is advantageous in this point because of its homogeneity in structure, thus it is promising and valuable to design a new material with atomic layer oxide. Besides, atomic layer oxides are promising models of mixed oxide catalysts. To make use of such advantages of atomic layer oxides, a number of oxides have been synthesized on highly divided inorganic supports.

There are many methods to deposit metal oxides on porous support surfaces. The impregnation in solution is most frequently carried out. However, oxides or salts in solution tend to precipitate and crystallize rather than to form layer structure during evaporation of the solvent, because the interaction of compound in the solution and support surface is rather weak. Thus, chemical vapor deposition (CVD) method is usually adopted to synthesize atomic layer oxides, where the strong chemical interaction of support and the deposited compound occurs, which keeps up the atomic layer structure. Either the spontaneous dispersion of metal oxide or chemical reaction of precursor

of metal chlorides, metal alkoxides or allyls [1] with support surface have been commonly carried out in recent days.

Spontaneous dispersion is applicable to volatile metal oxides such as MoO_3, NiO or V_2O_5 [2]. The spontaneous dispersion proceeds when the metal oxide with dispersed phase is thermodynamically advantageous over crystal phase due to the formation of bonding between metal oxide and support surface. The preparation procedure is quite simple, the mechanical mixture or impregnated form of metal oxide or salts and support component is heated for a few hours at elevated temperature but well below the melting point of the precursor. The formation of the atomic layer has been mainly proved by the quantitative phase analysis of X-ray diffraction where diffraction lines begin to appear at a specific loading of metal oxide, the loading agreed with the calculated loading value from close-pack atomic layer model. The atomic layer oxides are also characterized by XPS, Ion scattering, Raman or EXAFS spectroscopy, and so on. The change in chemical properties of the deposited material leads to the change of surface acidity or chemisorption amount of probe gas.

Another way to synthesize the atomic layer oxide utilizes the chemical reaction of metal oxide precursor and hydroxyl groups of support surfaces by vapor deposition. In recent days, metal alkoxides are frequently used as precursor for metal oxides. Because this grafting method utilizes the chemical reaction between the alkoxide and the hydroxyl groups, the control of the number of surface hydroxyl groups by evacuation in the pre-treatment step becomes important subject [3]. Silica is one of the most frequently used oxide for support of atomic layer oxides with this method, because of its stability, mechanical strength and the existence of hydroxyl groups on the surface. Silica has several types of hydroxyl groups such as isolated single, or hydrogen-bonded hydroxyl groups. Its surface is totally hydroxylated and covered with physisorbed water in the initial untreated condition [4]. To remove physisorbed water on porous silica, heating above 473 K must necessary [5]. In the dehydration steps, firstly the hydrogen bonded hydroxyl groups and then the isolated ones are removed to give siloxane groups. Further heating causes

has been reported that the total number of hydroxyl groups on a fully hydroxylated silica surface is about 5.0/nm^2, this value is independent of the type of silica [6]. In the preparation of GeO_2/SiO_2 carried out in this thesis, the dehydration of silica was conducted at 473 K. In this condition, physisorbed water is removed and the hydroxyl groups remains on the surface.

In the old days, IR spectroscopy was mainly used to follow the reaction mechanisms during chemical vapor deposition. Disappearance of the hydroxyl groups was observed during deposition. For instance, the intera9ction of the titanium alkoxide with the isolated or hydrogen bonded hydroxyl groups on silica was studied by Srinivasan et al. [7]. They tried to find out the factors which control the loading and the stability of dispersed TiO_2 obtained by calcination of the attached alkoxide. On the basis of IR studies, they concluded that the hydroxyl groups that are capable of hydrogen bonding with neighboring hydroxyls were the preferred adsorption sites of $Ti(i\text{-}OC_3H_7)_4$, while the isolated hydroxyl groups were inert to the reaction with $Ti(i\text{-}OC_3H_7)_4$ [7].

Recently a number of instrumental techniques have been developed and applied to the synthesis and characterization of atomic layer oxides. Raman spectroscopy is a powerful technique to obtain molecular structure of the oxide layer because each molecule has a unique vibrational spectrum. The measurement can be preformed *in-situ* or under ambient conditions because this spectroscopy is no inherent limitations of conditions such as temperature or presence of gas phase. This technique was applied to the characterization of molybdenum oxide [8-10], tungsten oxide [11], rhenium oxide [12], niobium oxide [13], vanadium oxide [14,15] and nickel oxide [15]. In case of vanadium oxide, Raman spectroscopy is capable of discriminating the type of vanadia species from measurement of the stretching mode of the sample. Monomeric vanadyls, one- and two-dimensional vanadate chains, and crystal of V_2O_5 on the SiO_2, TiO_2 and Al_2O_3 were identified by Bell et al. [16].

Extended X-ray absorption fine structure (EXAFS) is used to characterize the local structure of supported oxides. Structure of Nb_2O_5 atomic layer supported on SiO_2 prepared from

$Nb(OC_2H_5)_5$ was determined by EXAFS analysis and the formation of atomic layer structure was strongly supported by the linear dependency of the coordination number of Nb-Si bond on niobium loading in the catalyst, together with the X-ray diffraction results [17]. The bond formation between loaded metal oixde and silica surface was also observed on ZrO_2 supported on SiO_2 [18]. Asakura et al. have prepared TiO_2 overlayer on SiO_2 surface using $Ti(i\text{-}OC_3H_7)_4$ [19]. The characterization by means of EXAFS, together with X-ray diffraction and X-ray fluorescence reveals that TiO_2 is deposited as one-atomic layer with anatase-like structure with the (101) orientation. The one-atomic-layer was proved from comparison of the coordination number of two types of Ti-Ti bonds with reference materials.

Ion scattering spectroscopy is sensitive to the top layer of the surface [20]. SiO_2 thin layer was deposited on ZrO_2 and TiO_2 surface by chemical vapor deposition of $Si(OMe)_4$ and characterized by ion scattering spectroscopy, together with Auger electron spectroscopy and temperature desorption method [21]. The nearly fully surface of ZrO_2 was covered with SiO_2, but it was not the case for TiO_2. The result was concluded from the measurement of the composition of the top atomic layer by ion scattering spectroscopy which shows that the SiO_2 is fully covered on TiO_2 surface.

Solid state NMR provides valuable information on the reactions of silanes on silica. Information of hydroxyl groups on silica can be obtained by ^1H and ^{29}Si CPMAS NMR spectroscopies. Using ^{29}Si CPMAS NMR spectroscopy, different silicon sites are identified, namely $O_2Si(OH)_2$, O_3SiOH and SiO_4 groups. These NMR techniques were also used for study of the morphology of silica [22] or hydroxyl groups on dehydrated or rehydrated silica [23].

X-ray photoelectron spectroscopy (XPS) is used to study the oxidation state of metal oxides. Gonzeález-Elipe et al. have applied XPS to the characterization of TiO_2 supported on SiO_2. TiO_2 thin layers were obtained by evaporation of Ti metal on to silica substrates in the presence of oxygen, and formation of cross-linking Ti-O-Si bonds decreases the positive charge of the Ti atoms at the interface and the mobility of the electrons in the titania phase [24].

Interestingly, the catalytic behavior of dispersed oxides is often remarkably different from that of bulk oxides. This behavior is mainly brought from the difference of crystal structure or the effect of bond formation between oxide and support surface.

Niwa et al. have deposited the Mo oxides on SnO_2 [25], FeO_3 [26], ZrO_2, TiO_2 and Al_2O_3 [27] by an impregnation method and the spread of molybdenum oxide in atomic layer was determined by the measurement of the surface area of deposited oxides by the benzaldehyde-ammonia titration method [28]. Among the catalysts, SnO_2-supported catalyst showed the highest turn-over frequency in methanol oxidation reaction. The generation of high activity was attributed to the formation of Mo oxide phase, the structure of which agrees with the active MoO_3 (111) face, confirmed from the measurement of EXAFS spectra [29].

Sato et al. have prepared the silica-supported boria catalyst by the chemical vapor deposition of $B(OEt)_4$ onto silica gel [30]. The catalyst was characterized by surface area measurement with BET method, SEM and temperature programmed desorption of pyridine. These experiments showed the uniform deposition of B_2O_3 compared with an impregnated catalyst. The catalyst prepared from $B(OEt)_4$ was highly active and selective to the the Beckmann rearrangement. The reason was attributed to a larger amount of effective acid sites in addition to the uniform acid strength.

In the oxidation of *o*-xylene over V_2O_5/TiO_2, the selectivity to phthalic anhydride greatly depends on the thickness of the V_2O_5 on TiO_2 surface [31]. This is also observed in the reduction of nitric oxide with ammonia on V_2O_5/TiO_2 [32]. Strong acid sites are generated on WO_3/Al_2O_3 [33] which is highly related with the cluster size of WO_3 where interaction of WO_3 and Al_2O_3 surface plays an important role.

Ti oxides [34] containing Ti-O-Si interface have attracted much attention relevant to the reactivity of oxidation [35] and to the chemical feature in relation with the SMSI effect of TiO_2 with an outgrowth of interest this phenomena. The catalysts are synthesized by either deposition of TiO_2 to SiO_2 surface or co-precipitation of the two precursors and calcination to obtain the mixed

oxide. A unique example of the dispersed TiO_2 is Ti-containing zeolites, which show various unique reaction such as oxidation of organic compounds with hydrogen peroxide [36]. Ko et al. have investigated the catalytic behavior of NiO impregnated on TiO_2-SiO_2 mixed oxide. The behavior of the mixed oxide was different from that of bulk TiO_2. They attributed the reason to the generation of acid sites at the interface of TiO_2 and SiO_2 where the acidity affects the catalytic behavior of the NiO catalyst [37].

On Nb_2O_5 atomic layers supported with Pt, the SMSI behavior was suppressed compared with the use of bulk oxide [38,39]. The catalyst was applied to the esterification of ethanol and showed 20 times higher activity than bulk Nb_2O_5 because of the generation of Lewis acid sites on the Nb_2O_5 atomic layer surface [40]. Pt-deposited TiO_2 atomic layer is also highly resistible to the high temperature reduction treatment compared with the Pt-deposited bulk TiO_2 which is a typical catalyst of SMSI effect. Another strange phenomenon was found on Pt-deposited TiO_2 atomic layer during reduction treatment, that is the transformation of TiO_2 atomic layer structure from anatase-like structure to rutile-like structure with the (110) orientation.

Probably, the modification of pore opening size of zeolite by deposition of atomic layer oxide is one of the must successful applications of atomic layer oxide to catalyst support. This kind of control became realized by grafting and hydrogenolysis of disilanes [41,42] or alkoxides, and more recent examples are the grafting of thermally stable -MgNp [43] or -$GeBu_3$ [44] fragments on zeolites. Examples of the deposition of alkoxide on zeolites can be seen in the aluminum [45], silicon [46-49], germanium [50] compounds. In these studies, large metal alkoxide molecules react exclusively with OH groups on the external surface of zeolites, because the size of the alkoxides is bigger than the pore-opening size which makes the molecules to hardly diffuse and react in the pore of zeolite. Thus this treatment changes neither pore size nor acidic properties of zeolite. HZSM-5 zeolite modified with SiO_2 atomic layer was used in the alkylation of toluene [51]. In this study, with the increase of the amount of deposited silica, the selectivity to *m*- and *o*-xylene decreases, whereas the fraction of *p*-xylene increases to more than 98 %. This effect was

considered to be caused by the narrowing of the pore-opening size of the zeolite.

As described above, a number of atomic layer oxides have been synthesized by chemical vapor deposition method and characterized with a variety of techniques. And unique behaviors of atomic layer oxides have been identified when it was used as catalyst itself or catalyst support.

1-2 Metal Support Interaction in Supported Catalysts

Transition-metal catalysts are usually dispersed as small particles on robust inorganic oxides in order to achieve a high metal surface area. Extensive studies have been conducted to show the effect of support composition on catalytic activity and selectivity of metals supported on them. While some studies revealed that the difference in activity was attributed to difference in metal dispersion, strong evidence has been recognized for the substantial influence of support on the properties of metals. Meanwhile, Tauster et al. reported the so called strong metal support interaction (SMSI) where H_2 and CO chemisorption was greatly suppressed for metals supported on TiO_2 and reduced at 773 K but normal reduction after 473 K [52], and much work has been carried out to elucidate the essence of this phenomenon. In the pioneer work on Pt/TiO_2, a bonding feature or electronic interaction between metal and support surface was emphasized to explain the SMSI. In addition to this, pill box morphology, local intermetallic bonding and decoration model have been proposed to explain the observed phenomena. For example, Baker et al. studied TEM and selected area electron diffraction patterns on Pt/TiO_2 [53,54]. They concluded that the platinum forms particles with a flat pill-box shape at the SMSI state. Upon reoxidation the metal particles recover the original hemispherical shapes. This reversible change of the pill-box morphology was considered to be a characteristic SMSI feature. On the other hand, some groups explained the SMSI effect by change in electronic properties of metal which altered by support metal oxide [55,56]. Sadeghi et al. studied the interaction of atomically thin Rh film on TiO_2 (110) surface and showed that the electron transfer occurred from the reduced TiO_2 surface to the Rh

film, using a variety of electron spectroscopies [57]. The electronic interaction between metal and support has also been reported in the experiments on powder catalyst systems. Koningsberger et al. used EXAFS and high-resolution transmission microscopy (HRTEM) technique to study the structure of a Rh/TiO_2 catalyst. They compared the structures obtained by reduction at low and high temperatures [58,59]. While they provided no information of the coverage of the metal particles by TiO_2 suboxides in the SMSI state, the effect of suppression of oxidation with oxygen was ascribed to the electronic interaction between Rh particles and TiO_x suboxide, compared with the use of Al_2O_3 support.

In these days, the decoration model is the most predominant explanation for the SMSI phenomenon. Decorated metal particles were directly observed for Rh/TiO_2 [60-62], Pt/TiO_2 [63] and Ru/TiO_2 [64] catalysts reduced at high temperatures by means of high resolution TEM. And several studies on model catalyst provided direct physical evidence for the coverage with a partially reduced metal oxides on metal surfaces [65-70]. In the study of Sadeghi et al, surface composition of Rh-covered TiO_2 single crystals suffered various thermal treatment was measured by AES as a function of sputtering depth [71]. The untreated sample showed a monotonic decrease in Rh signal and a monotonic increase in Ti and O signals. The sample reduced at high temperatures showed an increase of Rh signal and a decrease of Ti and O signals, followed by the arrival at a the maximum, and then a monotonic decrease in Rh signal and an increase in Ti and O signals. This phenomenon was explained in terms of Ti suboxide which covered the Rh particles during high temperature treatment.

In addition to this, direct bond formation between metal and support due to the formation of alloy or intermetallic compound is still plausible. Haller et al. analyzed the EXAFS spectra of a reduced Rh/TiO_2 catalyst and demonstrated the formation of direct Rh-Ti bonding in the catalyst reduced at 773 K. The distance of Rh-Ti bond was calculated to be 0.253-0.256 nm which is much shorter than the bond distance, 0.268 nm observed in the stable intermetallic compounds. This was taken as an evidence that Ti (or Rh) has some cationic character as a result of association

of oxygen. They also compared the XANES spectra of Rh/TiO_2 with those for several intermetallic compounds of Rh and Ti [72]. The results suggested that the same kind of Rh-Ti bonding as intermetallic compounds occurs on Rh/TiO_2 reduced at high temperatures [73], because the XANES spectra of the reduced Rh/TiO_2 can be decomposed into a linear combination of that of Rh metal and several intermetallic compounds of Rh and Ti. Wang et al. studied the Pt/TiO_2 system by combining HREM measurement and computer-simulated images. In addition to decoration of metal with amorphous TiO_2 at low temperature, the formation of Pt-Ti intermetallic compounds such as Pt_3Ti and PtTi was identified upon reduction at 773 and 973 K, respectively [74]. They also found the evidence of reversibility of SMSI effect by HREM technique.

It may be interesting to note the recent report conducted by Basset et al. who have tried to prepare and characterize the molecular analogous of supported metal particles to elucidate the essence of metal-support interaction using supramolecular approach [75]. Their interest is especially directed to the role of interface of metal and support. The concept is extrapolation of organometallic chemistry of metal complexes on support surface to the metal-support interaction of Rh metal and support surface. Using organometallic fragment, they showed that the coordinated OH groups participated in the reactivity of monomeric surface and non-coordinated OH groups facilitated the migration of surface species.

The SMSI effect explained above is deeply related with the change in reactivity of catalyst. The origin of support effect to the catalytic activity of loaded transition metal has been extensively discussed. Enhancement of activity of the hydrogenation of CO or CO_2 was most intensely studied. Bell and co-workers have studied the influence of metal oxides on the catalytic CO and CO_2 hydrogenations on transition metals [76-80] with expectation that highly active sites may occur in the interface of metal and metal oxide. They reported the combination studies of XPS, TEM, ^1H NMR, volumetric chemisorption and catalytic reactions applied to the planar model system, consists of a metal foil decorated with controlled quantities of metal oxide, or to the dispersed metal catalyst. In the studies of model catalyst composed of metal oxide islands

deposited on clean Rh foil, it was observed that the hydrogenation of CO_2 rate reaches a maximum value when the coverage of the metal oxides was 0.5 atomic layer. And the degree of rate enhancement was strongly correlated with the Lewis acidity of metal cation, such as Ti^{3+} when TiO_2 was used for decoration of the clean metal surface, which is proportional to the electronegativity. The Ti^{3+} signal observed in XPS showed maximum intensity when TiO_2 coverage reached the 0.5 atomic layer, indicating the Ti^{3+} was concentrated at the interface between the oxide layer and the clean metal substrate. The Monte Carlo simulation showed that the summation of the perimeter of TiO_2 islands became maximum quantity when TiO_2 coverage corresponds to 0.5 atomic layer. Their conclusion from these combined studies is that the Lewis acid sites exist in the boundary of TiO_2 and Pt enhances the rate determining step of CO_2-H_2 reaction.

Recent report on layer-by-layer Pt films grown on ZrO_2(100) provided the evidence for bridging CO species adsorbed at the Pt and ZrO_2 interface from the measurements of AES, TPD and HREELS [81]. Reducible oxides, such as TiO_2, MnO, CoO and Nb_2O_5 which show the SMSI effect were added to a SiO_2-supported catalyst. Promotion effect on catalytic reactions (for example, CO hydrogenation) was observed in these systems. Ichikawa et al. proposed the promotion of Fe oxide in the CO-H_2 reaction on Rh to be chemical interaction of Rh clusters with Fe^{3+} ions [82]. Lisitsyn et al. demonstrated that Ti ions on SiO_2 surface increased the dispersion of cobalt and led to increase in relative yield of light hydrocarbons and ethanol in CO hydrogenation [83]. The enhancement of activity in the catalytic oxidation of CO to CO_2 and NO_2 to N_2 without formation of NH_3 was observed in a Rh catalyst when CeO_2 was added to the catalyst support [84]. Guglielminotti et al. have studied the role of CeO_2 in NO-CO reaction on $Rh/CeO_2/SiO_2$ catalyst by FT-IR technique [85]. The role of CeO_2 was, in addition to the role in storage of oxygen, improvement of thermal stability of the support and maintenance of high dispersion of Rh^+ and prevention of agglomeration to Rh^0 metallic phase [86,87].

1-3 Characterization and Catalytic Reaction of Ge Containing Bimetallic Alloys

Bimetal catalysts containing Ni, Ru, Rh, Pd and Pt combined with Sn as the second metal have been extensively studied [88-91], where the interest of researchers ranges from the structure of bimetals in organometallic chemistry to the applications to so many kinds of catalytic reactions, such as NO-CO, reforming of alkanes and hydrogenation. Whereas Ge belongs to the same group in the periodic table as Sn, bimetal catalysts containing Ge has not been studied so much. However, in this decade, several groups have paid attention to this system. Most extensively studied is PtGe, in relation with the catalytic reaction of alkane reforming and hydrogenation of unsaturated compounds. The attention was mainly directed to the chemical state of Ge in alloy and the catalytic reaction was merely conducted as the test reaction to study the chemical state of Ge, except for the recent report by Borgana et al., where the thioresistance was studied with kinetic consideration [92]. Bouwman et al. studied the $PtGe/Al_2O_3$ catalyst and found that the fraction of Ge was in the zero valent state and it is probably alloyed with Pt by XPS measurement [93]. The studies on the chemical state of Ge can be exemplified as follows. Goldwasser et al. reported that the special property observed in catalysis for isomerization was due not to the dilution effect of Ge but to the electronic interaction was related in the phenomena. PtGe alloy formation was also reported by Miguel et al. on the basis of the result of TPR and test reactions [94]. They studied the valence state of Ge by hydrogen TPR with several hypothesis. At reduction temperatures lower than 623 K, germanium is located near platinum atom and provides only geometric effect, but at higher reduction temperatures, germanium becomes mainly zerovalent and modifies the electronic effect of platinum because the activity of cyclohexane hydrogenolysis is suppressed by 100 to 500 times lower than Pt/Al_2O_3 catalyst.

Catalytic hydrogenation on Ge-containing bimetallic alloy catalysts have been carried out by several groups and interesting results were reported. Galvagno et al. studied the effect of Ge together with Pt supported on Nylon and found that the addition of small amount of Ge to Pt

accelerated the selective hydrogenation of α,β-unsaturated aldehyde, namely cinnamaldehyde toward the corresponding unsaturated alcohol, cinnamyl alcohol under mild conditions [95]. The effect of Ge is so drastic as the addition of only a few atomic % Ge in the alloy increases the activity so much; While on the monometallic Pt sample, the selectivity to cinnamaledhyde was less than 2 %, the addition of only 0.2 atomic % Ge leads to a selectivity of 64 %, and 90 % when the Ge content is 7-10 %. As analogous to the PtSn/Nylon catalyst [96], it is proposed that the such a high activity was brought from the activation of the C=O bond through the enhancement of the positive charge of the carbon atom.

Structure and catalysis of bimetals composed of Pt or Ru and Sn, Pb, Ge, Al or Zn have been investigated [97,98]. In these catalysts, the attention was especially directed toward the bimetals containing Ge. They studied the topology of Rh particle modified by Ge in the hydrogenolysis of 2,2,3,3-tetramethylbutane as a probe molecule. The hydrogenolysis of 2,2,3,3-tetramethylbutane gives selectively 2,2,3-trimethylbutane and methane upon small Rh particles, whereas isobutane selectively forms on larger particles, which have more sites of high coordination. The addition of Sn or Pb favors the formation of isobutane, but the addition of equivalent amount of Ge promotes the demethylation. Thus they concluded that the Sn and Pb are concentrated at the sites of low coordination, while Ge appears to be randomly distributed at the surface of Rh particles. They also characterized Ru-Ge bimetal catalyst by EXAFS, TEM and XRD. Ru particles disperse as metal clusters composed of no more than 12 atoms by the addition of Ge. The main ground of this explanation is the attenuation of EXAFS oscillation by the addition of Ge to Ru. Hydrogenation of citral and cinnnamaldehyde was tried on Ge added Ru catalysts, but neither effect to activity nor selectivity was observed which is contrast to the above Galvagno's experiment where drastic effect of the on addition of small amount of Ge was observed in the hydrogenation of α,β-unsaturated alcohol.

Recently, Ge and Rh system has been started to study in the field of surface organometallic chemistry, which may be the extension of the chemistry of Rh-Sn system already studied [99].

Surface-stabilized germylene, $Rh_s[Ge(Ad)(H)]_y/SiO_2$ (Ad=Adamantyl) was synthesized by a controlled reaction between Rh/SiO_2 and $(Ad)GeH_3$ complex from gas phase by Basset et al. [100]. The surface reaction and characterization of the surface organometallic compounds was mainly followed by IR spectroscopy. The germanium complex does not react with silanol groups on the support, and the reaction exclusively proceeds on Rh surface through reductive elimination of H_2 from $(Ad)GeH_3$. The species present on the surface after grafting is supposed to be a kind of germylene (II) surface species stabilized by coordination of a surface rhodium atom.

As described above, study of Ge in bimetallic catalysts is limited to few examples, but several groups have found interesting aspects. It is promising to explore the Ge-promoting system in the field not only surface organometallic but catalyst chemistry.

1-4 References

[1] Y. Iwasawa, *"Tailored Metal Catalysts"*, ed., Y. Iwasawa, D. Reidel Publishing Company, Holland, (1986) P. 15.

[2] Y.-C. Xie and Y.-Q. Tang, *Adv. Catal.*, **37** (1988) 1.

[3] M. Niwa, *Shokubai*, **34** (1992) 221.

[4] J. H. De Boer and J. M. Vleeskens, *Proc. Kon. Ned. Akad. Wetensch.*, **B61** (1958) 2.

[5] B. A. Morrow, *Studies in Surface Science and Catalysis*, ed. J. L. G. Fierro, Elsevier Science Publishers, Amsterdam, **57** (1990) A166.

[6] L. T. Zhuravlev, *Langmuir*, **3** (1987) 316.

[7] S. Srinivasan, A. K. Datye, M. H. Smith and C. H. Peden, *J. Catal.*, **145** (1994) 575.

[8] G. L. Schrader, C. P. Chang, *J. Catal.*, **80** (1983) 369

[9] S. S. Chan, I. E. Wachs, L. L. Murrell, L. Wang and W. K. Hall, *J. Phys. Chem.*, **88** (1984) 5831.

[10] J. M. Stencel, L. E. Makovski, T. A. Sarkus, J. De Vries, R. Thomas and J. A. Moulijin, *J.*

Catal., **90** (1984) 314.

[11] E. Payen, S. Kasztelan, J. Grimblot, J. P. Bonnell, *Catal. Today*, **4** (1988) 57.

[12] K. P. J. Williams and K. Harrison, *J. Chem. Soc., Faraday Trans.*, **86** (1990) 1603.

[13] J. M. Jeng and I. E. Wachs, *J. Phys. Chem.*, **95** (1991) 7373.

[14] M. A. Vuurman and I. E. Wachs, *J. Phys. Chem.*, **96** (1992) 5008.

[15] T. J. Pines, C. H. Rochester and A. M. Ward, *J. Chem. Soc., Faraday Trans.*, **87** (1991) 653.

[16] G. T. Went, S. T. Oyama and A. T. Bell, *J. Phys. Chem.*, **94** (1990) 4240.

[17] K. Asakura and Y. Iwasawa, *J. Phys. Chem.*, **95** (1991) 1711.

[18] K. Okumura and Y. Iwasawa, *J. Catal.*, **164** (1996) 440.

[19] K. Asakura, J. Inukai and Y. Iwasawa, *J. Phys. Chem.*, **96** (1992) 829.

[20] L. Marchut, T. M. Buck, G. H. Wheatley and C. J. McMahon, Jr, *Surf. Sci.*, **141** (1984) 539.

[21] T. Jin, T. Okuhara and J. M. White, *J. Chem. Soc., Chem. Commun.*, (1987) 1248.

[22] A. Tuel, H. Hommel, A. P. Lerand, Y. Chevallier and J. C. Moravski, *Colloids Surf.*, **45** (1990) 413.

[23] D. W. Sindorf, G. E. Maciel, *J. Am. Chem. Soc.*, **105** (1983) 1487.

[24] G. Lassaletta, A. Fernández, J. P. Espinós and A. R. González-Elipe, *J. Phys. Chem.*, **99** (1995) 1484.

[25] M. Niwa, H. Yamada and Y. Murakami, *J. Catal.*, **134** (1992) 331.

[26] H. Yamada, M. Niwa and Y. Murakami, *J. Catal.*, **96** (1993) 113.

[27] Y. Matsuoka, M. Niwa and Y. Murakami, *J. Phys. Chem.*, **94** (1990) 1477.

[28] M. Niwa, S. Inagaki and Y. Murakami, *J. Phys. Chem.*, **89** (1985) 3869.

[29] M. Niwa, M. Sano, H. Yamada and Y. Murakami, *J. Catal.*, **151** (1995) 285.

[30] S. Sato, K. Urabe and Y. Izumi, *J. Catal.*, **102** (1986) 99.

[31] I. E. Wachs, S. S. Chan, C. C. Cherish and R. Y. Saleh, *Stud. Surf. Sci. Catal.*, **19** (1984)

275.

[32] A. Baiker, P. Dollenmeier, M. Glinski and A. Reller, *Appl. Catal.*, **35** (1987) 351.

[33] L. L. Murrell, *J. Catal.*, **79** (1983) 203.

[34] H. H. Kung, *Stud. Surf. Sci. Catal.*, **45** (1889) .

[35] S. Imamura, S. Ishida, H. Tarumoto, Y. Saito and T. Ito, *J. Chem. Soc., FaradayTrans.*, **89** (1993) 757.

[36] Y. Ohnishi and T. Hamamura, *Bull. Chem. Soc. Jpn.*, **43** (1970) 996.

[37] E. I. Ko, J.-P. Chen and J. G. Weissman, *J. Catal.*, **105** (1987) 511.

[38] K. Asakura and Y. Iwasawa, *Chem. Lett.*, (1988) 633.

[39] K. Asakura and Y. Iwasawa, *Chem. Lett.*, (1986) 859.

[40] M. Shirai, K. Asakura and Y. Iwasawa, *J. Phys. Chem.*, **95** (1991) 9999.

[41] Y. Yan, J. Verbiest, P. de Hulster, E. F. Vansant, *J. Chem. Soc., FaradayTrans.*, **85** (1989) 3095.

[42] Y. Yan and E. F. Vansant, *J. Phys. Chem.*, **94** (1990) 2582.

[43] A. Théolier, E. Custodero, A. Choplin, J.-M. Basset and J. F. Joly, *J. Am. Chem. Soc.*, **115** (1995) 722.

[44] C. Nédez, A. Choplin, J. Corler,J-M. Basset,J.-F. Joly and E. Benazzi, *J. Mol. Catal.*, **92** (1994) L239.

[45] H. E. Bergna, M. Keane, Jr, D. H. Ralston, G. C. Sonnichsen, L. Abrahams and R. D. Shannon, *J. Catal.*, **115** (1989) 148.

[46] H. Kuno, M. Shibagaki, K. Takahashi, I. Honda and H. Matsushita, *Bull. Chem. Soc. Jpn.*, **64** (1991) 2508.

[47] H. E. Bergna, M. Keane, Jr, D. H. Ralston, G. C. Sonnichsen, L. Abrahams and R. D. Shannon, *J. Catal.*, **115** (1989) 148.

[48] T. Hibino, M. Niwa, Y. Murakami, M. Sano,S. Komai and T. Hanaichi, *J. Phys. Chem.*, **93** (1989) 7847.

[49] M. Niwa, S. Kato, T. Hattori and Y. Murakami, *J. Chem. Soc., FaradayTrans.*, **80** (1984) 3135.

[50] T. Hibino, M. Niwa, Y. Murakami and M. Sano, *J. Chem. Soc., FaradayTrans.*, **85** (1989) 2327.

[51] T. Hibino, M. Niwa and Y. Murakami, *J. Catal.*, **128** (1991) 551.

[52] S. J. Tauster, S. C. Fung and R. L. Garten, *J. Am. Chem. Soc.*, **100** (1978) 170.

[53] R. T. K. Baker, E. B. Prestidge and R. L. Garten, *J. Catal.*, **56** (1979) 390.

[54] R. T. K. Baker, E. B. Prestidge and R. L. Garten, *J. Catal.*, **59** (1979) 293.

[55] G.-M. Schwab, *Adv. Catal.*, **27** (1978) 1.

[56] F. Solymosi, *Catal. Rev.*, **1** (1967) 233.

[57] H. R. Sadeghi, H. R. Henrich, *J. Catal.*, **87** (1984) 279.

[58] J. H. A. Martens, R. Prins, H. Zandbergen and D. C. Koningsberger, *J. Phys. Chem.*, **92** (1988) 1903.

[59] D. C. Koningsberger, J. H. A. Martens, R. Prins, D. R. Short and D. E. Sayers, *J. Phys. Chem.*, **90** (1986) 3047.

[60] A. D. Logan, E. J. Brauunschweig,A. K. Datye and D. J. Smith, *J. Catal.*, **118** (1989) 227.

[61] A. D. Logan, E. J. Braunschweig, A. K. Datye and D. J. Smith, *Langmuir*, **4** (1988) 827.

[62] S. Bernal, J. J. Calvino, M. A. Cauqui, G. A. Cifredo, A. Jobacho and J. M. Rodreíguez-Izquierdo, *Appl. Catal. A*, **99** (1993) 1.

[63] A. K. Datye, D. S. Kalakkad, M. H. Yao and D. J. Smith, *J. Catal.*, **155** (1995) 148.

[64] T. Komaya, A. T. Bell, Z. Weng-Sieh, R. Gronsky, F. Engelke, T. S. King and M. Pruski, *J. Catal.*, **149** (1994) 142.

[65] Y.-M. Sun, D. N. Belton and J. M. White, *J. Phys. Chem.*, **90** (1986) 5178.

[66] Y.-W. Chung, G. Xiong and C.-C. Kao, *J. Catal.*, **85** (1984) 237.

[67] S. Takatani and Y. Chung, *J. Catal.*, **90** (1984) 75.

[68] C. S. Ko and R. J. Gorte, *J. Catal.*, **90** (1984) 59.

[69] D. N. Belton, Y.-M. Sun and J. M. White, *J. Phys. Chem.*, **88** (1984) 5172.

[70] G. P. Raupp and J. A. Dumesic, *J. Catal.*, **95** (1985) 587.

[71] H. R. Sadeghi and V. E. Henrich, *J. Catal.*, **87** (1984) 279.

[72] S. Sakellson, S. McMillan and G. L. Haller, *J. Phys. Chem.*, **90** (1986) 1733.

[73] D. E. Resasco, R. S. Weber, S. Sakelton, M. McMillan and G. L. Haller, *J. Phys. Chem.*, **92** (1988) 189.

[74] L. Wang, G. W. Qiao, H. Q. Ye, K. H. Kuo and X. Y. Chen, *Proceedings 9th International Congress Catalysis* (Calgary), eds. M. J. Phillips and M. Ternan, The Chem. Inst. Canada, Ottawa, **3** (1988) 1253.

[75] C. C. Santini, S. L. Scott and J.-M. Basset, *J. Mol. Catal. A: Chemical*, **107** (1996) 263.

[76] A. T. Bell, *J. Mol. Catal. A: Chemical*, **100** (1995) 1.

[77] A. B. Boffa, C. Lin, A. T. Bell and G. A. Somorjai, *Catal. Lett.*, **27** (1994) 243.

[78] A. Boffa, C. Lin, A. T. Bell and G. A. Somorjai, *J. Catal.*, **149** (1994) 149.

[79] T. Koyama, A. T. Bell, Z. Weng-Sieh, R. Gronsky, F. Engelke, T. S. King and M. Pruski, *J. Catal.*, **149** (1994) 142.

[80] T. Koyama, A. T. Bell, Z. Weng-Sieh, R. Gronsky, F. Engelke, T. S. King and M. Pruski, *J. Catal.*, **150** (1994) 400.

[81] P. A. Dilara and J. M. Vohs, *J. Phys. Chem.*, **99** (1995) 17259.

[82] A. Fukuoka, T. Kimura, N. Kosugi, H. Kuroda, Y. Minai, Y. Sakai, T. Tominaga and M. Ichikawa, *J. Catal.*, **126** (1990) 434.

[83] A. S. Lisitsyn, A. V. Golovin, V. L. Kuznetsov and Yu I. Yermakov, *J. Catal.*, **95** (1985) 527.

[84] K. C. Taylor, *Catal. Rev.-Sci. Eng.*, **35** (1993) 457.

[85] E. Guglielminotti and F. Boccuzzi, *J. Mol. Catal. A: Chemical*, **104** (1996) 273.

[86] C. C. Santini, J.-M. Basset, B. Fontal, J. Krause, S. Shore and C. Charrier, *J. Chem. Soc., Chem. Commun.*, (1981) 512.

[87] A. Choplin, B. Besson, L. D'Omelas, R. Sanchez-Delgado and J.-M. Basset, *J. Am. Chem. Soc.*, **110** (1988) 2783.

[88] K. Tomishige, K. Asakura and Y. Iwasawa, *J. Catal.*, **157** (1995) 472.

[89] K. Tomishige, K. Asakura and Y. Iwasawa, *J. Catal.*, **149** (1994) 70.

[90] J.-M. Basset, J. P. Candy, P. Dufour, C. Santini and A. Choplin, *Catal. Today*, **6** (1989) 1.

[91] J.-M. Basset, J. P. Candy, A. Choplin, C. Nédez and F. Quignard, *Mater. Chem. Phys.*, **29** (1991) 5.

[92] A. Borgana, T. F. Garetto, A. Monzón and C. R. Apesteguía, *J. Catal.*, **146** (1994) 69.

[93] R. Bouwman and P. Biloen, *Appl. Catal.*, **48** (1977) 209.

[94] S. R. D. Miguel, O. A. Scelza and A. A. Castro, *Appl. Catal.*, **44** (1988) 23.

[95] S. Galvagno, Z. Poltarzewski, A. Donato, G. Neri and R. Pietropaolo, *J. Chem. Soc., Chem. Commun.*, (1986) 1729.

[96] Z. Poltarzewski, S. Galvagno, R. Pietropaolo and P. Staiti, *J. Catal.*, **102** (1986) 190.

[97] G. C. Bond and J. C. Slaa, *J. Mol Catal. A: Chemical*, **98** (1995) 81.

[98] A. Goursot, B. Coq, L. de Ménprval, T. Tazi, F. Figueras and D. R. Salahub, *Z. Phys. D-Atoms Molecules and Clusters*, **19** (1991) 367.

[99] B. Didillon, J. P. Candy, A. El. Mansour, C. Houtmann and J.-M. Basset, *J. Mol. Catal.*, **74** (1992) 43.

[100] M. Taoufik, C. C. Santini, J.-P. Candy, A. de Mallmann and J.-M. Basset, *J. Am. Chem. Soc.*, **118** (1996) 4167.

Chapter 2 Characterization of GeO_2 submonolayers on SiO_2 Prepared by Chemical Vapor Deposition of $Ge(OMe)_4$ by EXAFS, FT-IR and XRD

Abstract

GeO_2 submonolayers on SiO_2 surfaces were prepared by chemical vapor deposition (CVD) reaction of $Ge(OMe)_4$ with OH groups on SiO_2 at 393 K, followed by calcination at 693 K. The characterization of the obtained GeO_2/SiO_2 was conducted by FT-IR, XRD and EXAFS. Isolated OH groups of SiO_2 preferentially reacted with $Ge(OMe)_4$. The Si-OH peak disappeared once by the CVD reaction of $Ge(OMe)_4$, and half of the original Si-OH peak appeared again after the calcination. The linear increase of Ge-OH peak and the linear decrease of Si-OH peak with increasing Ge loading suggest a monolayer growth of GeO_2. The coverage of GeO_2 layers at saturation for the sample prepared by the one-time CVD process was estimated to be 1/5 monolayer of the SiO_2 surface which corresponds to 7.4 wt% Ge loading. There existed only isolated Ge-OH groups on the GeO_2 layers, which is contrasted to the case of bulk-GeO_2 which shows both isolated and hydrogen-bonded OH groups. The surface of the GeO_2 layers on SiO_2 has no acidic character, whereas GeO_2/Al_2O_3 showed both Brönsted and Lewis acid sites. EXAFS spectra showed significantly lower Ge-Ge signal compared with that for bulk-GeO_2. The local structure around Ge in the GeO_2/SiO_2 was determined to be similar to the hexagonal type GeO_2.

2-1 Introduction

Inorganic oxide monolayers developed on the other oxide surfaces have attracted attention in terms of preparation of new type of surface materials with unique catalytic performance [1]. The simplest way to produce monolayer catalysts is to use an appropriate combination of overlayer

oxide and substrate oxide such as V_2O_5 on TiO_2 and MoO_3 on TiO_2. In these systems the overlayer oxides wet well the substrate surfaces and spontaneously spread over the surfaces as monolayers by heat treatment. On the other hand, chemical reactions between surface OH groups and precursor complexes are the other way to synthesize monolayer materials, which do not show the spontaneous spread to monolayer. The surface reaction technique by using alkoxides as precursors has successfully applied to the synthesis of monolayer oxides with well-defined structures; e.g. ZrO_2/ZSM-5 [2], Nb_2O_5/SiO_2 [3-5] and TiO_2/SiO_2 [6]. These samples have been employed to unique catalysts which converted methanol to isopentane selectively [2], and catalyzed esterification of acetic acid with ethanol and intramolecular dehydration of ethanol, and also employed as a support for Pt [6]. Recently, GeO_2 monolayers were prepared on Al_2O_3 and zeolite surfaces by use of Ge organometallic compounds [7-9]. It has been reported that Brönsted acidity was generated on the GeO_2 layers deposited on Al_2O_3, and Ge-O-Ge networks were formed on mordenite. GeO_2 has also been deposited on SiO_2 by chemical vapor deposition (CVD) of $GeCl_4$ and subsequent hydrolysis [10].

In this study I have synthesized GeO_2 layers on SiO_2 by CVD reaction of $Ge(OMe)_4$ with surface OH groups of SiO_2, followed by calcination. The aim of the study is to estimate the reactivity of different kinds of OH groups at SiO_2 surface with $Ge(OMe)_4$, to characterize the structure and growth mode of GeO_2 overlayers on SiO_2 by FT-IR, XRD and EXAFS, and to examine the difference in the reactivities of Ge-OH groups on the GeO_2 layer and Si-OH groups on the SiO_2 support to $Ge(OMe)_4$ to provide a possible way to prepare layer-by-layer structure of GeO_2.

2-2 Experimental

2-2-1 Preparation of GeO_2/SiO_2

Preparation of GeO_2/SiO_2 was carried out in a closed circulating system. $Ge(OMe)_4$ as precursor was purchased from Soekawa Chemicals Co. (99.999 %), and purified by distillation in vacuum line before use. SiO_2 (Aerosil 300; 300 m^2g^{-1} or ox-50; 50 m^2g^{-1}) was evacuated at 473 K for 1 h to remove physisorbed water, and exposed to given amounts of $Ge(OMe)_4$ vapor at 393 K for 1 h, followed by evacuation at 473 K to remove the unreacted $Ge(OMe)_4$ and the organic products. The obtained sample was calcined at 693 K for 1 h under 20.0 kPa of oxygen in the closed circulating system. The evolved CO_2 and H_2O were removed by a trap with liquid N_2. Maximum Ge loading on SiO_2 (Aerosil 300) by the CVD reaction with excess amount of $Ge(OMe)_4$ was 7.4 wt%. The preparation conditions were varied in the CVD temperature range 353-423 K and in the CVD period from 1 h to 5 h, but no change was observed with the Ge loading. To obtain the samples with more than 7.4 wt% loading of Ge, the above procedure was repeated two or three times. The Ge loading was determined on a X-ray fluorescence spectrometer (SEIKO SEA-2010) by using weighted GeO_2 diluted with SiO_2 as reference.

2-2-2 FT-IR Measurement

FT-IR spectra were measured on a JASCO FT-IR 230 spectrometer with 2 cm^{-1} resolution. The spectra were recorded in an *in-situ* IR cell with two NaCl windows which was combined in a closed circulating system. The sample was pressed to a wafer of 2 cm in diameter. Preparation of GeO_2/SiO_2 and subsequent treatments were carried out *in-situ* in the cell , because of the instability of GeO_2/SiO_2 to moisture. Typically, a SiO_2 (50 mg) disk was placed in the IR cell, evacuated at 473 K and reacted with a given amount of $Ge(OMe)_4$ vapor at 393 K, followed by evacuation at

473 K and calcination under circulating oxygen (20.0 kPa) at 693 K for 1 h.

2-2-3 Ge K-edge XAFS Measurement

X-ray absorption fine structure (XAFS) spectra at Ge K-edge were measured at the beam line 7C in Photon Factory of the National Laboratory for High-Energy Physics (KEK-PF) (Proposal No.94G-203). The beam line is equipped with a sagittal focusing Si(111) double crystal monochromator. The monochrometer was detuned to 70 % in order to remove the higher harmonics. The storage ring energy was 2.5 GeV with a ring current of 250-350 mA. All spectra were recorded at room temperature in a transmission mode. The sample was transferred to glass cells with two Kapton windows which were connected to a closed circulating system without contacting air. Two ion chambers filled with N_2 100 % and Ar 15 %／N_2 85 % were used as X-ray detectors for I_0 (before sample) and I (after sample), respectively.

For extended X-ray absorption fine structure (EXAFS) analysis, the oscillation was extracted from EXAFS data by a spline smoothing method [11]. The oscillation was normalized by edge height around 50 eV above the threshold. The energy dependence of the edge height was corrected by the McMaster equation [12]. The Fourier transformation of the k^3-weighted EXAFS oscillation from k space to r space to obtain a radial distribution function was performed over the range 30-140 nm^{-1}. The inversely Fourier filtered data were analyzed by a curve fitting method based on eq (1).

$$\chi(k)=\Sigma N_j F_j(k)\exp(-2\sigma_j^2 k_j^2)\sin(2kr_j+\phi_j(k))/kr_j^2 \qquad (1)$$
$$k_j=(k^2-2m\Delta E_{0j}/\hbar^2)^{1/2}$$

where N_j, r_j, σ_j and ΔE_{0j} represent coordination number, bond distance, Debye-Waller factor and difference of the threshold energy between reference and sample, respectively. $F_j(k)$ and $\phi_j(k)$ represent amplitude and phase shift functions, respectively. For the curve fitting analysis, empirical phase shift and amplitude functions were extracted from hexagonal type GeO_2 as the

reference compound. Error of the analysis was estimated by R factor (R_f) calculated by eq (2).

$$R_f = \int | k^3\chi(k)^{obs} - k^3\chi(k)^{calc} |^2 dk \Big/ \int | k^3\chi(k)^{obs} |^2 dk \quad (2)$$

The error bars in the present curve fitting analysis for bond distance and coordination number are estimated to be ± 0.003 nm and ± 20 %, respectively. The above analysis of EXAFS data was performed using the "REX" program (RIGAKU).

2-3 Results and Discussion

2-3-1 Characterization of GeO_2 supported on SiO_2 by FT-IR and XRD

Figure 1 shows the relation between the amount of $Ge(OMe)_4$ exposed to the pretreated SiO_2 in a closed circulating system and the Ge wt% in the obtained GeO_2/SiO_2 sample. The Ge/SiO_2 weight ratio increased linearly until it reached saturation at 7.4 wt%. Introduction of $Ge(OMe)_4$ vapor more than 1.3 kPa to the system did not raise the Ge loading at saturation significantly as shown in figure 1. Thus 7.4 wt% was the maximum Ge loading attained by the one-time CVD process of $Ge(OMe)_4$ on SiO_2.

FT-IR spectra after the reaction of $Ge(OMe)_4$ with SiO_2 surface and the calcination of the obtained sample were measured to examine the CVD process on SiO_2 pretreated for 1 h at 473 K (Figure 2 (A)) and at 723 K (Figure 2 (B)). In figure 2 (A) spectrum (a) for the 473 K-treated SiO_2 shows a sharp peak at 3745 cm^{-1} and a broad one at 3650 cm^{-1} which have been assigned to isolated and hydrogen bonded OH groups, respectively. After the CVD reaction with excess amount of $Ge(OMe)_4$ (spectrum (b)), most of all the isolated OH groups disappeared, and the peaks at 2989, 2946 and 2843 cm^{-1} due to the C-H stretching modes and at 1465 and 1452 cm^{-1} due to the bending modes developed, which may originate from the surface $Ge(OMe)_x$ ($x \leqq 4$), because they coincide with the peaks for $Ge(OMe)_4$ [13]. The intensity of the broad band for the

hydrogen bonded hydroxyl groups also decreased by the CVD of $Ge(OMe)_4$, and a new peak at 3450 cm^{-1} appeared, which may be due to OH groups also interacted with $Ge(OMe)_x$. After calcination of the $Ge(OMe)_x/SiO_2$ sample, the methoxy groups completely disappeared and the two absorption bands appeared at 3745 cm^{-1} and 3676 cm^{-1}. The former band is identical to the isolated OH groups originally bound on SiO_2 which once disappeared by the CVD reaction with $Ge(OMe)_4$ and reappeared with half of the original intensity. The new peak of 3676 cm^{-1} is assignable to isolated OH groups on the GeO_2 overlayer deposited on SiO_2, because the observed wavenumber agrees well with isolated OH groups on bulk-GeO_2 reported in the literature [14,15]. Both isolated and hydrogen bonded OH groups are observed on bulk-GeO_2, whereas the hydrogen bonded OH groups were not present on the deposited GeO_2 layers.

The reactivity of hydroxyl groups on SiO_2 pretreated at 723 K with $Ge(OMe)_4$ was also examined by FT-IR in figure 2 (B). The averaged number of surface OH groups on silica can be controlled by changing evacuation temperature [16,17]. Most of physisorbed water is removed at 473 K, leaving a saturated amount of OH groups (ca. 5 OH nm^{-2}), while strongly-hydrogen bonded OH groups and a part of the weakly hydrogen-bonded OH groups are removed by evacuation at 723 K. As shown in figure 2 (B) most of the hydrogen bonded OH groups were removed, and the isolated OH groups were retained on the SiO_2 surface treated at 723 K. The preferential reaction of the isolated OH groups on the 723 K-treated SiO_2 with $Ge(OMe)_4$ was observed in figure 2 (B) similarly to the case for the 423 K-treated SiO_2 (Figure 2 (A)). A new peak at 3420 cm^{-1} appeared, which may be due to OH groups interacted with surface $Ge(OMe)_x$ species. By calcination of the obtained $Ge(OMe)_x/SiO_2$ sample at 693 K the isolated OH groups appeared again and the new peak at 3677 cm^{-1} also appeared, which is assigned to isolated OH groups on the deposited GeO_2 layers. These feature is similar to that observed with the 423 K treated SiO_2.

The CVD of $Ge(OMe)_4$ was also performed on the low surface area SiO_2 (ox-50) whose surface area is 1/6 of Aerosil 300, to check influence of the surface area on the CVD process. The

similar FT-IR spectra were obtained as shown in figure 3, which indicates the CVD process to form GeO_2 overlayers is independent of the kind of SiO_2.

After the CVD reaction with $Ge(OMe)_4$ at 393 K the sample was evacuated at 473 K for 2 h to remove the excess unreacted $Ge(OMe)_4$, but the Si-OH peak at 3745 cm^{-1} remained unchanged and the methoxy peaks retained their intensity. The peak of the isolated Si-OH groups was recovered only after calcination of the sample at 723 K. The X-ray fluorescence analysis showed no change of the Ge loading in GeO_2/SiO_2 before and after the calcination, which implies that the reappearance of the Si-OH peak is not due to desorption of the deposited GeO_2.

Figure 4 shows the typical FT-IR spectra of GeO_2/SiO_2 with different Ge loadings prepared by varying the amount of $Ge(OMe)_4$ vapor (up to 7.4 wt%) exposed to SiO_2. The samples with Ge loadings of more than 7.4 wt% were prepared by further CVD of the 7.4 wt% GeO_2/SiO_2 sample with $Ge(OMe)_4$ vapor at 393 K, followed by calcination at 693 K. The intensity of the Ge-OH peak at 3676 cm^{-1} increased with an increase of Ge loading, while the intensity of the Si-OH peak at 3745 cm^{-1} decreased as Ge loading increased. Figure 5 shows the plots of their intensities against the Ge wt%. The linear increase of Ge-OH intensity and reversely the linear decrease of Si-OH intensity were observed in the range of Ge loading 0-7.4 wt%. The isolated Si-OH intensity for the sample with the Ge loading of 7.4 wt% decreased to half of the original Si-OH intensity before Ge deposition, at which the Ge-OH intensity was nearly the same as the Si-OH intensity. The CVD of $Ge(OMe)_4$ consumed the isolated OH groups on the SiO_2 surface and the produced GeO_2 overlayers possessed isolated Ge-OH groups. The number of the isolated Ge-OH groups per Ge atom in GeO_2/SiO_2 can be estimated from comparison of the Ge loading with the intensity of the Ge-OH groups observed in the FT-IR spectra, assuming that the absorption coefficients of O-H stretching peaks are similar between Ge-OH groups on GeO_2 and Si-OH groups on SiO_2. The density of isolated OH groups on SiO_2 evacuated at 473 K was estimated to be 2 OH nm^{-2} by ^1H MAS NMR [21]. According to their estimation, on GeO_2/SiO_2 (7.4 wt%) the amount of Si-OH groups decreased to 1 OH nm^{-2} and simultaneously the same number of Ge-OH grew. From

the number of the Ge-OH groups and the Ge loading it can also be estimated that one Ge-OH group exists per two Ge atoms in the GeO_2/SiO_2. The loading of Ge corresponds to occupation of 1/5 monolayer of the silica surface when the Ge loading is 7.4 wt%, assuming that 2-dimensional [GeO_2] unit area has 0.1 nm^2.

I have tried to obtain GeO_2 fullmonolayer on the SiO_2 surface by repeated $Ge(OMe)_4$-CVD calcination cycles. To know the reactivity of $Ge(OMe)_4$ with the SiO_2 surface and the GeO_2 layer (GeO_2/SiO_2; 7.4 wt%) obtained by one CVD-calcination cycle using excess $Ge(OMe)_4$, a small amount of $Ge(OMe)_4$ vapor (67 Pa) was introduced to the 7.4 wt% GeO_2/SiO_2 at 393 K. Figure 6 shows the drastic decrease of the Ge-OH peak by the reaction of $Ge(OMe)_4$ with the GeO_2/SiO_2. On the contrary, the Si-OH peak little reduced. It suggests that $Ge(OMe)_4$ vapor reacts preferentially with the Ge-OH groups on the GeO_2 submonolayers rather than the Si-OH groups on the exposed SiO_2 surface as shown in figure 7. The break in the lines in figure 5 suggests the change in the growth mode of GeO_2 layer. It may be difficult to obtain fullmonolayer of GeO_2 on SiO_2 surface under the present CVD conditions. However, these results present a possible way for layer-by-layer growth of GeO_2 by the repeated deposition procedure.

The phenomena that the saturated amount of Ge deposited in the one-time CVD process by using excess $Ge(OMe)_4$ was about 1/5 monolayer of the SiO_2 surface and that the Si-OH peak once disappeared by the CVD reaction with $Ge(OMe)_4$ at 393 K and appeared again by calcination of the $Ge(OMe)_x/SiO_2$ at 693 K may be explained as follows. As the amount of the disappeared Si-OH groups was equal to the amount of Ge loading as discussed above, it seems that the reaction of Si-OH with $Ge(OMe)_4$ at 393 K took place stoichiometrically as follows:

$$Si\text{-}OH + Ge(OMe)_4 \rightarrow Si\text{-}O\text{-}Ge(OMe)_3 + MeOH,$$

$$Si\text{-}OH + MeOH \rightarrow Si\text{-}O\text{-}Me + H_2O$$

Calcination of the Si-OMe group results in the formation of Si-OH group again. Alternatively, the CVD reaction may occur as follows:

$$2\ Si\text{-}OH + Ge(OMe)_4 \rightarrow \begin{matrix} Si\text{-}O \\ Si\text{-}O \end{matrix} \diagdown\!\diagup Ge \diagdown\!\diagup \begin{matrix} OMe \\ OMe \end{matrix} + 2\ MeOH$$

In this case the reaction of Me-OH with Si-OH is excluded. The obtained $(Si\text{-}O)_2Ge(OMe)_2$ species may be transformed to Si-OH (recovered) and $Si\text{-}O\text{-}GeO_x$. However, the concentration of the isolated Si-OH groups on the SiO_2 surface has been suggested to be as small as 2 OH/nm^2. The probability of the reaction of a $Ge(OMe)_4$ molecule with two Si-OH groups should be small. The 1:1 stoichiometry between the amount of Si-OH disappeared and the amount of Ge loaded by the CVD is assumed to be due to the surface chemical process. If Ge species is incorporated into the SiO_2 bulk, the intensities of Si-OH and Ge-OH peaks would not change linearly as a function of Ge loading unlike the result of figure 5. The 1/5 monolayer coverage of GeO_2 at saturation in the one-time CVD process indicates that the coverage of GeO_2 was limited by the Si-OH quantity and that $Ge(OMe)_4$ did not react with other surface sites like Si-O-Si.

Figure 8 shows the XRD pattern of GeO_2/SiO_2. No diffraction line was detected with the 1～3 times CVD samples, which demonstrates that the deposition of GeO_2 on SiO_2 did not grow to 3-dimensional crystals.

Figure 9 shows FT-IR spectra of the GeO_2/SiO_2 sample preserved under moisture, together with the fresh GeO_2/SiO_2. Moisture significantly decreased the Ge-OH peak intensity (3676 cm^{-1}). This change is possibly caused by crystallization of the GeO_2 overlayers and the decrease of GeO_2 surface area. The crystallization of the GeO_2 overlayers was evidenced by the growth of diffraction line at $2\theta=25.5^\circ$ as shown in figure 8 (d). The ease of destruction of the GeO_2 structure with moisture may be related to the crystal structure of GeO_2, which was similar to the water-soluble hexagonal type GeO_2 as characterized by EXAFS (discussed hereinafter). It was supposed that the crystallization of the GeO_2 submonolayer to the 3-dimensional GeO_2 caused the reappearance of the SiO_2 surface which was covered by GeO_2 layers and hence the reappearance of Si-OH groups, but Si-OH peak intensity did not increase on exposure to moisture. However, the peak became somewhat broader due to the overlap of a new peak at 3741 cm^{-1} with the original Si-OH peak at 3745 cm^{-1}. Morrow et al. observed appearance of a band at 3742 cm^{-1} during rehydration when small quantity of water was added to the fully dehydrated silica [18-20]. They

attributed the new band to the weakly interacting pair of vicinal single silanols. In the present case, vicinal OH pairs originate from the Si-OH groups grown by the hydration of Si-O-Ge bond.

Figure 10 shows the FT-IR spectra of pyridine adsorbed on GeO_2/SiO_2 to examine the acidic character of GeO_2/SiO_2. There are neither strong Brönsted nor Lewis sites on SiO_2 surfaces [21]. The spectrum after the adsorption of pyridine and subsequent evacuation at room temperature shows two bands at 1445 cm^{-1} and 1596 cm^{-1} in the region of ring vibration of pyridine. It is known that adsorption of pyridine on Brönsted acid sites yields pyridinium ion with an absorption band at 1540 cm^{-1} [22]. Pyridine coordinated on Lewis acid sites has a band at 1440-1465 cm^{-1} and the frequency depends on the strength of bonding. By evacuation at 373 K the adsorbed pyridine disappeared. Thus there is no pyridine strongly adsorbed on GeO_2/SiO_2, indicating no Brönsted and Lewis acid sites on the surface. This is contrasted to the report on GeO_2/Al_2O_3 where both types of acidic sites were detected from the IR measurement of adsorbed pyridine [9]. The reason of neutrality of the GeO_2 layers on SiO_2 may be ascribed to the neutral character of the Ge-O-Si bond at the interface and also to the equivalent valency of Ge and Si atoms.

2-3-2 Characterization of GeO_2 Supported on SiO_2 by EXAFS

EXAFS spectra for GeO_2/SiO_2 were measured to characterize the local structure around Ge atom. Figure 11 shows the EXAFS oscillations ($k^3\chi(k)$) at Ge K-edge and their Fourier transformations (FT) for the GeO_2/SiO_2 samples with different Ge loadings and for bulk-GeO_2 (hexagonal type). The spectra of figure 11 (a)-(d) are similar with each other, but the feature is considerably different from that of the bulk-GeO_2 (Figure 11 (e)). The intense peak for bulk-GeO_2 at 0.28 nm (phase shift uncorrected) attributed to Ge-Ge bond remarkably reduced in GeO_2/SiO_2, but the peak height and position of the Ge-O bond observed at 0.14 nm (phase shift uncorrected) did not change in these GeO_2/SiO_2 samples. Similar results were obtained on GeO_2 supported on a low surface area SiO_2 (ox-50). The low intensity of Ge-Ge peak for GeO_2/SiO_2 was

independent of Ge loading in the range ≦7.4 wt% Ge. The Ge-Ge contribution in the EXAFS spectra a little increased above this loading (two- or three-times CVD samples), which is apparent by the rapid wave observed around 98 and 118 nm^{-1} in the $k^3\chi(k)$ spectra as indicated by arrows (Figure 11 (d)). This observation suggests the existence of Ge-O-Ge networks in the GeO_2 overlayer on SiO_2. The constant height of the Ge-Ge peak for the samples with Ge loadings below 7.4 wt% implies that the GeO_2 submonolayers grow as islands with an identical dimension and the number of islands increases with the increase in Ge loading. Table 1 summarizes the curve fitting results of the EXAFS data for GeO_2/SiO_2 as well as the crystallographic data for hexagonal and tetragonal GeO_2 [23,24]. Bond distances determined by the curve fitting analysis were 0.172-0.173 nm for Ge-O and 0.306-0.313 nm for Ge-Ge. Compared with the structural data for the two kinds of GeO_2, the local structure around Ge in GeO_2/SiO_2 was similar to that for hexagonal GeO_2. The EXAFS data for the as-CVD sample before calcination in figure 11 (a) is essentially the same as those for the calcined samples. This suggests that fundamental frame of the GeO_2 layer on SiO_2 was similar before and after calcination and the Ge-Ge bonding has already existed before calcination. The Si-O-$Ge(OMe)_3$ species may be assembled through the methoxy linkage leading Ge-O-Ge network. The formation of a similar network structure has been proposed in the process of deposition of $Si(OMe)_4$ on mordenite by IR and gas-phase analysis [25].

2-4 Conclusions

Formation of GeO_2 overlayers on SiO_2 was achieved by the chemical reaction of $Ge(OMe)_4$ vapor with OH groups on SiO_2 surface. The reaction occurred preferentially with the isolated OH groups of SiO_2. Monolayer growth of GeO_2 (Ge loading < 7.4 wt%) on SiO_2 was characterized by FT-IR, XRD pattern and Ge K-edge EXAFS. Neither Brönsted nor Lewis acidic characters were detected on GeO_2/SiO_2. The GeO_2/SiO_2 showed Ge-O-Ge networks and the existence of one isolated OH group per two Ge atoms. The local structure of Ge in GeO_2/SiO_2 was similar to that

for hexagonal GeO_2 as characterized by EXAFS. The maximum Ge loading obtained by the 1-time CVD process on SiO_2 (Aerosil 300) was 7.4 wt% which corresponds to 1/5 of the GeO_2 full-monolayer over the SiO_2 surface. The repeated CVD processes resulted in the multi layer growth of GeO_2 on the first GeO_2 overlayer as suggested by FT-IR.

2-5 References

[1] Y.-C. Xie and Y.-Q. Tang, *Adv. Catal.*, **37** (1988) 1.

[2] K. Asakura, M. Aoki, M.and Y. Iwasawa, *Catal. Lett.* **1** (1988) 395.

[3] K. Asakura and Y. Iwasawa, *Chem. Lett.* (1986) 859.

[4] M. Shirai, K. Asakura and Y. Iwasawa, *J. Phys. Chem.*, **95** (1991) 9999.

[5] K. Asakura and Y. Iwasawa, *Chem. Lett.* (1988) 633.

[6] K. Asakura, J. Inukai and Y. Iwasawa, *J. Phys. Chem.* **96** (1992) 829.

[7] T. Hibino, M. Niwa, Y. Murakami and M. Sano, *J. Chem. Soc., Faraday Trans.1* **85** (1989) 2327.

[8] T. Hibino, M. Niwa, Y. Murakami, M. Sano, S. Komai and T. Hanaichi, *J. Phys. Chem.* **93** (1989) 7847.

[9] N. Katada, M. Niwa and M. Sano, *Catal. Lett.* **32** (1995) 131.

[10] V. M. Gun'ko, E. F. Voronin, V. I. Zarko and E. M. Pakhlov, *Langmuir* **13** (1997) 250.

[11] Y. Iwasawa, (eds.) *X-ray Absorption Fine Structure for Catalysts and Surfaces*; World Scientific: Singapore, 1996.

[12] W. H. McMaster, N. Kerr Del Grande, N. Mallet and J. H. Hubell, *Comparison of X-ray Cross Section*; National Technical Information Service: Springfield, 1969.

[13] O. H. Johnson and H. E. Fritz, *J. Am. Chem. Soc.* **75** (1953) 718.

[14] J. C. McManus, K. Matsushita and M. J. D. Low, *Can. J. Chem.* **47** (1969) 1077.

[15] A. Metcalfe and S. U. Shankar, *J. Chem. Soc., Faraday Trans.1* **76** (1980) 489.

[16] Y. Iwasawa, (ed.) *Tailored Metal Catalysts*; Reidel: Dortrecht, 1986.

[17] L. T. Zhuravlev, *Langmuir* , **3** (1987) 316.

[18] B. A. Morrow and I. A. Cody, *J. Phys. Chem.*, **79** (1975) 761.

[19] B. A. Morrow, I. A. Cody and L. S. M. Lee, *J. Phys. Chem.*, **80** (1976) 2761.

[20] B. A. Morrow and A. J. McFarlan, *J. Phys. Chem.*, **96** (1992) 1395.

[21] S. Haukka and A. Root, *J. Phys. Chem.*, **98** (1994) 1695.

[22] E. P. Parry, *J. Catal.*, **2** (1963) 371.

[23] W. H. Bauer and A. A. Khan, *Acta Cryst.*, **B272** (1971) 133.

[24] G. M. Smith and P. B. Isaacs, *Acta Cryst.*, **17** (1964) 842.

[25] M. Niwa, Y. Kawashima, T. Hibino and Y. Murakami, *J. Chem. Soc., FaradayTrans.1*, **4** (1988) 4327.

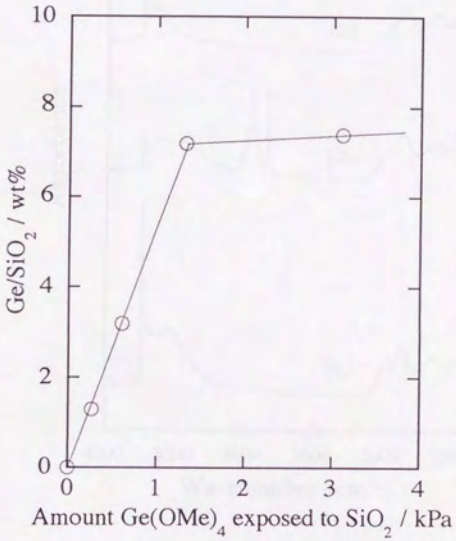

Figure 1. Relation between given amounts of $Ge(OMe)_4$ exposed to SiO_2 at 393 K and Ge/SiO_2 weight ratios in the obtained GeO_2/SiO_2.

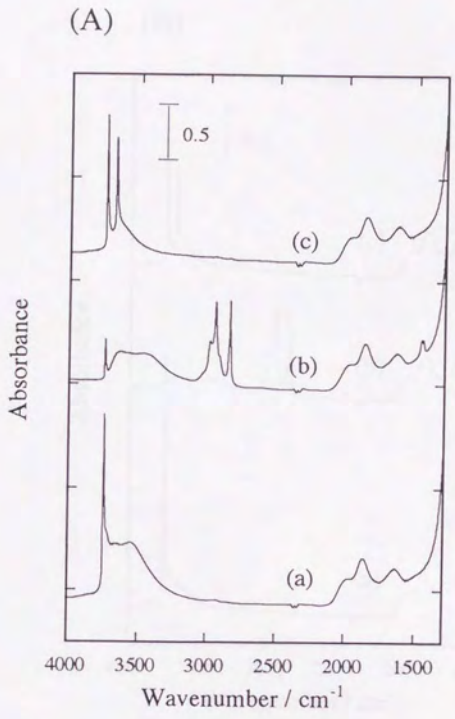

Figure 2 (A). FT-IR spectra of (a) SiO_2 evacuated at 473 K for 1 h, (b) after CVD reaction with excess $Ge(OMe)_4$ at 393 K followed by evacuated at 473 K, (c) after calcination of (b) at 693 K for 1 h.

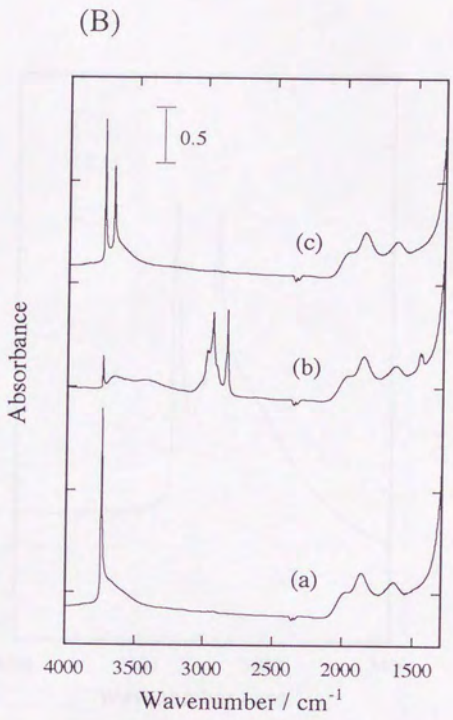

Figure 2 (B). FT-IR spectra of (a) SiO_2 evacuated at 723 K for 1 h, (b) after CVD reaction with excess $Ge(OMe)_4$ at 393 K followed by evacuated at 473 K, (c) after calcination of (b) at 693 K for 1 h.

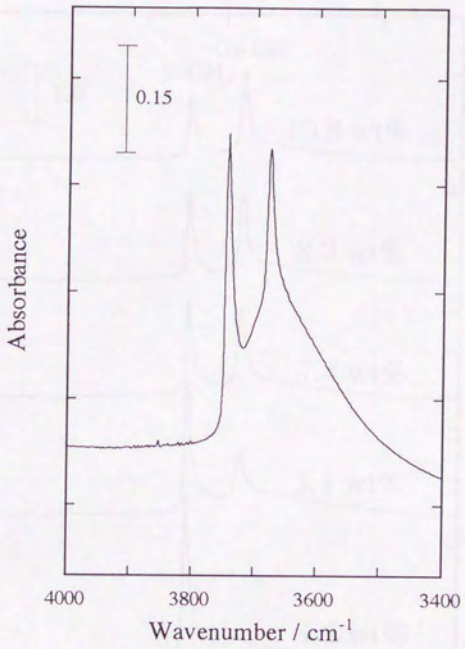

Figure 3. FT-IR spectra of GeO_2/SiO_2 (SiO_2: ox-50).

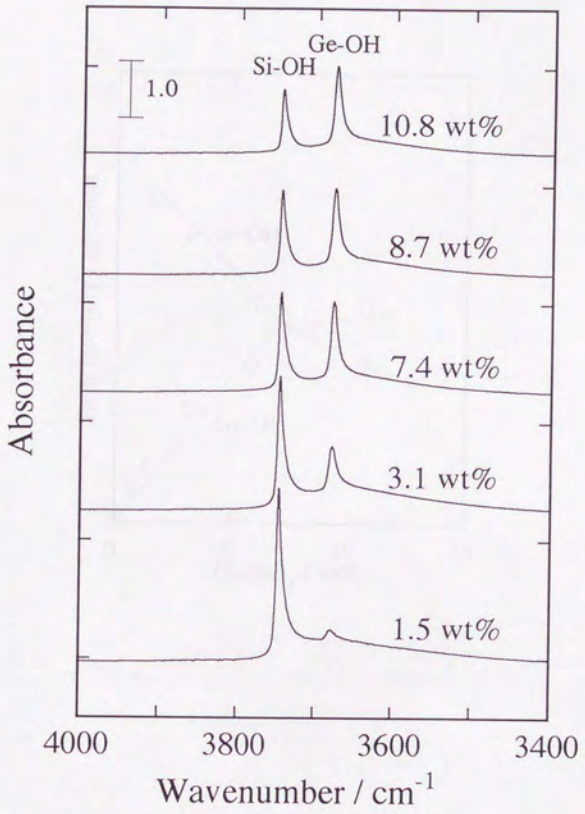

Figure 4. FT-IR spectra of GeO_2/SiO_2 with different Ge loadings prepared by one-time CVD process with various amounts of $Ge(OMe)_4$ (less than 7.4 wt%), and by repeated CVD processes (above 8.7 wt%).

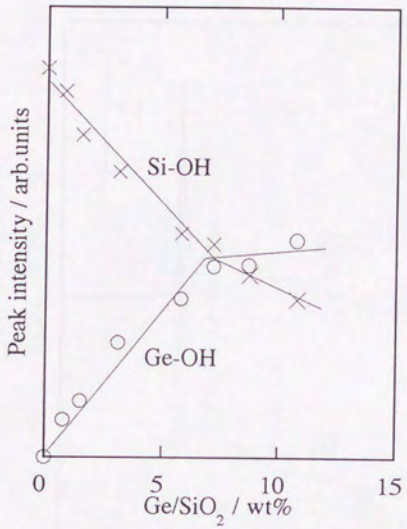

Figure 5. Intensity of Ge-OH (3676 cm^{-1}) and Si-OH (3745 cm^{-1}) peaks for GeO_2/SiO_2 as a function of Ge wt%; ○: Ge-OH, ×: Si-OH.

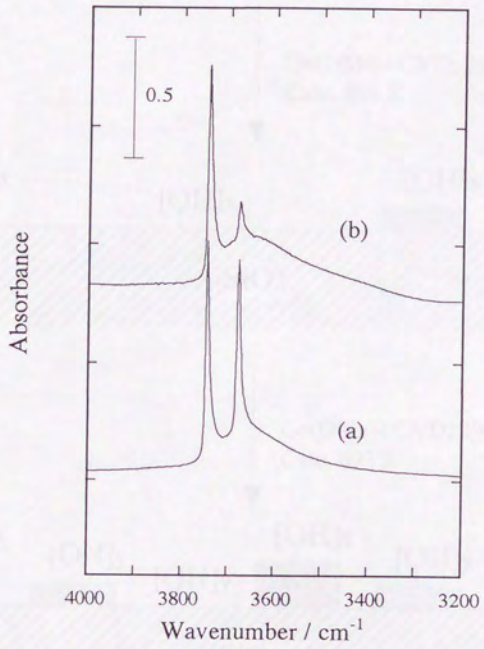

Figure 6. FT-IR spectra of (a) GeO_2/SiO_2 (Ge: 7.4 wt%) and (b) after exposure of (a) to a small amount (67 Pa) of $Ge(OMe)_4$ to (a) at 393 K.

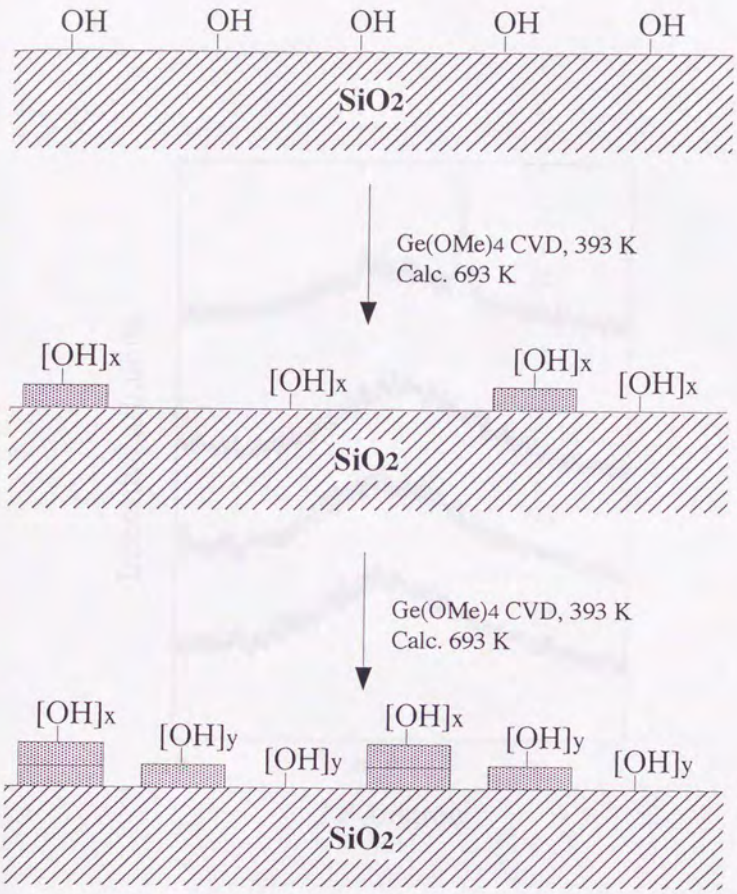

Figure 7. Simplified scheme for the CVD process for formation of GeO_2 sub-monolayers on SiO_2.

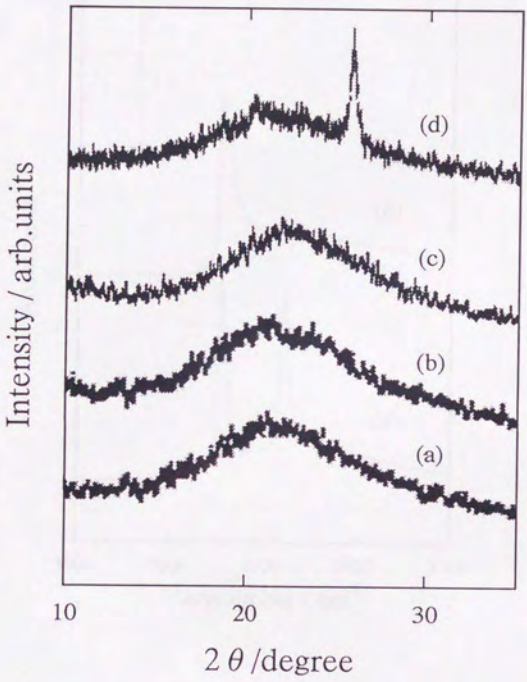

Figure 8. X-ray diffraction patterns of GeO_2/SiO_2 prepared by repeated CVD processes; (a) 1-time CVD, (b) 2-times CVD, (c) 3-times CVD; (d) GeO_2/SiO_2 exposed to moisture-saturated air.

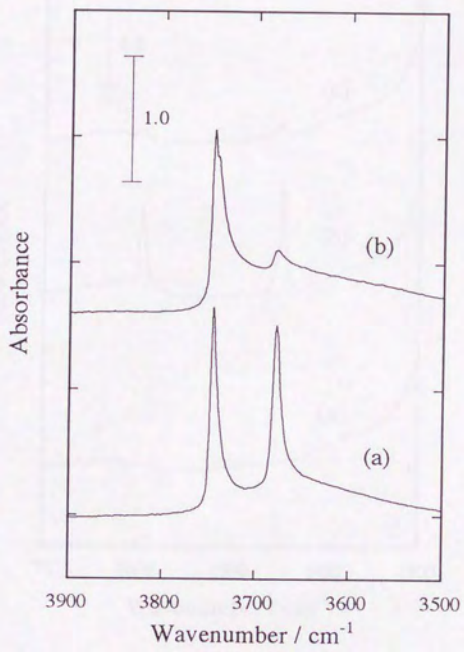

Figure 9. FT-IR spectra of (a) GeO_2/SiO_2 (Ge: 7.4 wt%) and (b) GeO_2/SiO_2 exposed to moisture-saturated air.

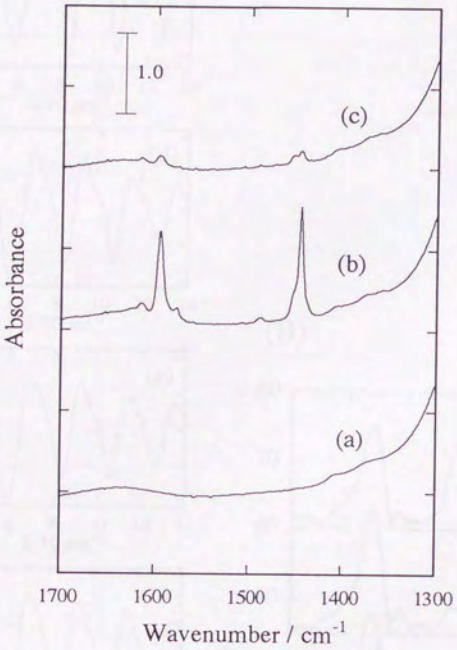

Figure 10. FT-IR spectra of (a) GeO_2/SiO_2 (Ge 7.4 wt%), (b) after exposure to 6.6 kPa of pyridine, followed by evacuation at room temperature and (c) after evacuation of (b) at 373 K.

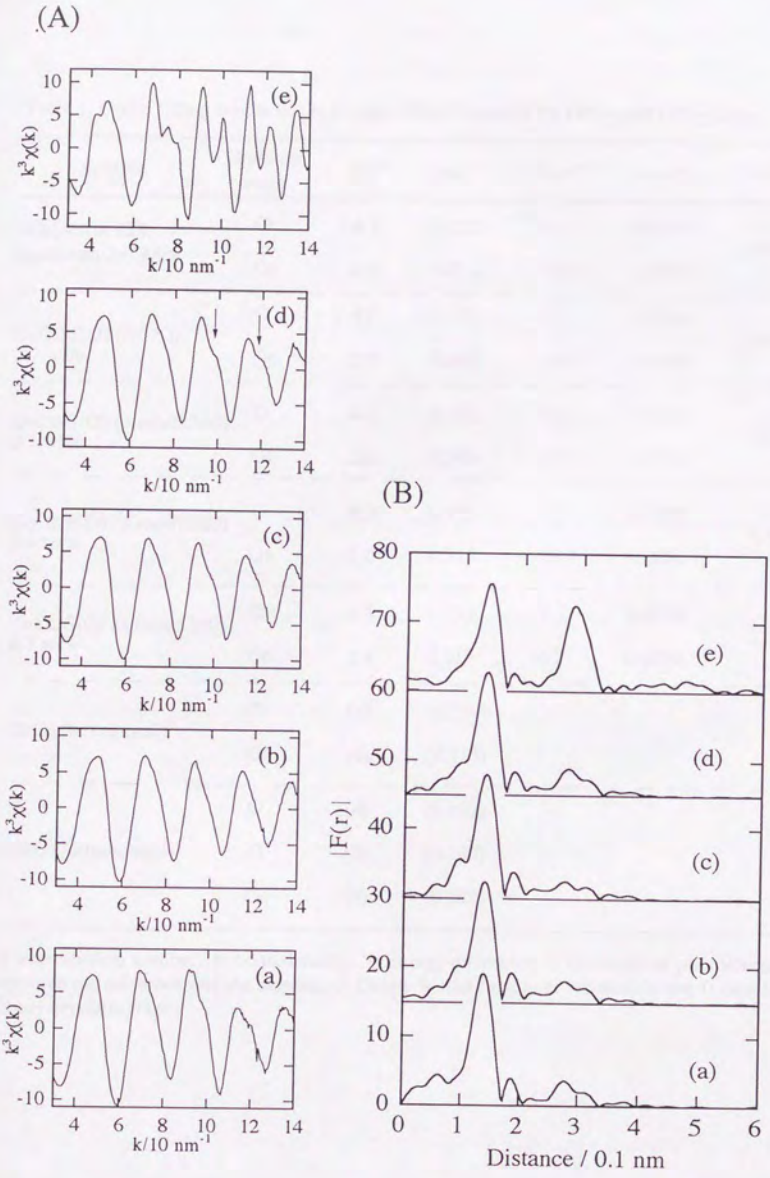

Figure 11. Ge K-edge EXAFS oscillations (A) and Fourier transforms (B); (a) as-$Ge(OMe)_4$ reacted (no calcination); (b) GeO_2/SiO_2 (3.2 wt%), (c)7.4 wt%, (d) 8.3 wt%; (e) GeO_2 (hexagonal type).

Table 1. Curve fitting results of Ge K-edge EXAFS spectra for GeO_2 and GeO_2/SiO_2.

Sample	Scatterer atom	CN[a]	r/nm[b]	ΔE_0/eV[c]	σ/nm[d]	R_f/%[e]
SiO_2 (Aerosil 300) reacted with $Ge(OMe)_4$	O	4.1	0.172	-2.4	0.0050	5.9
	Ge	2.3	0.311	-10.0	0.0089	
GeO_2/SiO_2 (ox-50) 1.7 wt%	O	4.6	0.172	-1.2	0.0061	3.8
	Ge	2.8	0.307	-16.6	0.0098	
GeO_2/SiO_2 (Aerosil 300) 3.1 wt%	O	4.1	0.173	-0.2	0.0052	3.5
	Ge	2.0	0.306	-19.9	0.0105	
GeO_2/SiO_2 (Aerosil 300) 7.4 wt%	O	3.9	0.173	-1.5	0.0052	4.4
	Ge	2.0	0.311	-10.0	0.0086	
GeO_2/SiO_2 (Aerosil 300) 8.7 wt%	O	4.5	0.173	-1.5	0.0059	2.6
	Ge	2.4	0.313	-6.2	0.0083	
GeO_2 (hexagonal)[f]	O	(4)	(0.174)			
	Ge	(4)	(0.315)			
GeO_2 (tetragonal)[f]	O	(4)	(0.187)			
	O	(2)	(0.190)			
	Ge	(8)	(0.342)			

a: coordination number, b: bond distance, c: energy difference in the origin of photoelectron between the reference and the sample, d: Debye-Waller factor, e: residual factor, f: data from X-ray crystallography.

Chapter 3 Reversible Structural Change of Rh Particles Supported on GeO_2 Submonolayers/SiO_2 in Reduction and Oxidation by XAFS, XRD, TEM and FT-IR

Abstract

The behaviors of Rh particles and GeO_2 submonolayers supported on SiO_2 in oxidation and reduction were investigated to reveal structural change in the outmost support surface of supported metal catalysts by means of XAFS, XRD, TEM and FT-IR. Partial reduction of the GeO_2 overlayers in $Rh/GeO_2/SiO_2$ occurred to form RhGe alloy particles by reduction with H_2 at 423-723 K, as proved by direct Rh-Ge bonding observed by EXAFS at both Rh and Ge K-edges. The RhGe alloy particles were transformed to Rh oxides and GeO_2 submonolayers by calcination at 673 K, and reversely these oxide phases were converted to the RhGe alloy particles by reduction at 423-723 K again. These transformations on SiO_2 reversibly took place in the oxidation-reduction treatments. This is a unique structural change at the Rh/GeO_2 overlayer interface in contrast to the behaviors of Rh and Ge on bulk GeO_2 which were irreversible due to subsidence of Rh into GeO_2 bulk.

3-1 Introduction

In supported metal catalysts the principal role of support is to disperse the metals and to prevent them form sintering under catalytic conditions. In addition to these physical interactions, catalyst supports often affect the catalytic properties of metals on them through electronic or structural interactions. However, we have few pieces of information about the structural change of metal-support interface, because the investigation of structural change of support surfaces demands surface sensitive techniques to discriminate it from that of the bulk. EXAFS spectroscopy have been applied to two model systems for this purpose though EXAFS

is not a surface spectroscopy; monolayer-oxide or thin layer-oxide samples specially prepared as target interfaces. One is the dispersed thin-layer ZrO_2 on Pd [1]. The other is monolayer oxides deposited on the other oxide surfaces as supports for metals, such as $Pt/Nb_2O_5/SiO_2$ [2] and Pd/La_2O_3/ZSM-5 [3], which showed unique catalytic properties. It was also found that irreversible structure change in the TiO_2 monolayer of $Pt/TiO_2/SiO_2$ occurred in the oxidation-reduction treatments [4]. Designed metal sites at oxide surfaces by using appropriate metal complex precursors have also been characterized by EXAFS. For example, Rh dimers attached on SiO_2 were observed to show dynamical structure change including metal-metal bond formation and breaking which promoted catalytic ethene hydroformylation [5].

To select the kind of monolayer metal-oxide suitable for the above purpose, I have prepared several monolayer oxides deposited on SiO_2 and the interaction with Rh was studied by IR measurement of CO as a probe molecule. The prepared oxides were TiO_2/SiO_2, ZrO_2/SiO_2, Nb_2O_5/SiO_2 and GeO_2/SiO_2. When TiO_2/SiO_2, ZrO_2/SiO_2 and Nb_2O_5/SiO_2 were used as supports for Rh, no difference from the IR spectra of CO on Rh/SiO_2 was observed. On the other hand the $Rh/GeO_2/SiO_2$ reduced above 523 K showed only linear CO at 2074 cm^{-1}, which was different from the others which showed linear, bridge and germinal CO peaks, suggesting the occurrence of chemical and structural Rh-GeO_2 interaction.

GeO_2 is the same family as SiO_2 and has similar structure and valency. In the previous chapter GeO_2 submonolayer (one-atomic layer) was prepared on SiO_2 surface and characterized to have a similar structure to hexagonal GeO_2 with Ge-O and Ge-Ge bonds at 0.173 nm and 0.311 nm, respectively. The GeO_2 submonolayer surface showed almost no Brönsted and Lewis acidity, indicating that Ge-O-Si bonding is rather covalent and neutral due to the similar character and structure between GeO_2 and SiO_2. The spectroscopic characterization of the outmost surface of oxide supports which directly interacts with supported metal and metal oxide particles is usually difficult because of the presence of the oxide bulk. The GeO_2 submonolayer may be regarded as a model of the outmost surface of SiO_2 support and characterized separately

from the SiO_2 support. Besides the GeO_2 submonolayer system may provide new surface phenomenon different from the bulk GeO_2.

In the present study I preformed the EXAFS analysis of Rh/GeO_2 submonolayer/SiO_2 under oxidation and reduction together with XRD, TEM and FT-IR to find the reversible structural change of the Rh/GeO_2 interface, where Rh was deposited on GeO_2 submonolayers supported on SiO_2 to more clearly extract the information on the metal/oxide structural change. The GeO_2/SiO_2 was prepared by CVD of $Ge(OMe)_4$ on SiO_2 surface as reported in chapter 2. The behavior of the Rh/GeO_2 submonolayer/SiO_2 was compared with those of Rh particles on bulk GeO_2 and SiO_2.

3-2 Experimental

3-2-1 Sample Preparation

GeO_2 overlayers on silica (Aerosil 300) were prepared by a chemical vapor deposition (CVD) method using $Ge(OMe)_4$ as precursor. The detail of the synthesis of the monolayers was already reported elsewhere in chapter 2. The samples are denoted as GeO_2/SiO_2. The coverage of GeO_2 prepared by one-time CVD procedure was 0.2 monolayer which corresponds to 7.4 wt% loading of Ge on the SiO_2. In this study the loading of Ge was fixed at 7.4 wt% otherwise especially noted. All handling of the GeO_2/SiO_2 was conducted without exposing to air to avoid destruction of the GeO_2 overlayer caused by moisture in the atmosphere.

A given amount of Rh dimer complex, $[Rh(C_5Me_5)Me]_2(\mu\text{-}CH_2)_2$ was dissolved in chloroform which had been purified by reflux over dried molecular sieves followed by distillation before use. The chloroform solution of the complex and the GeO_2/SiO_2 were mixed and stirred for 1 h at room temperature. The deep red solution of the Rh complex became transparent, which indicates that attachment of the complex on the support was completed. The

solvent was removed by evacuation and the obtained sample was transferred to a U-shaped tube reactor which was combined in a closed circulating system (dead volume: 210 cm^3). The sample was oxidized at 673 K under circulating oxygen (20.0 kPa) with a liq. N_2 trap to remove the remaining ligands on Rh in the closed circulating system. Subsequently, the oxidized sample was reduced with H_2 (13.3 kPa) at given temperatures in the range 423-723 K. These samples are denoted as $Rh/GeO_2/SiO_2$ (1). The sample (1) reduced at 723 K was oxidized with O_2 at 673 K and reduced with H_2 in the temperature range 423-723 K again. These are denoted as $Rh/GeO_2/SiO_2$ (2). The loading of Rh was 2.0 wt%. The Rh dimer was also supported on bulk GeO_2 (hexagonal type) (Rh 2.0 wt%) and treated similarly to the case of $Rh/GeO_2/SiO_2$.

3-2-2 XAFS Analysis

X-ray absorption fine structure (XAFS) spectra at Rh and Ge K-edges were measured at room temperature in a transmission mode at the beam lines 10B and 7C of Photon Factory in the National Laboratory for High-Energy Physics (KEK-PF), respectively (Proposal No.94G-203). The storage ring energy was operated at 2.5 GeV with a ring current of 250-350 mA. The 10B and 7C stations are equipped with a Si(311) channel cut monochromator and a Si(111) sagittal focusing double crystal monochromator, respectively. In order to remove the higher harmonics, the monochromators were detuned to 70 %. The sample was transferred to glass cells with two Kapton windows connected to a closed circulating system without contacting air. For the measurement of Rh K-edge spectra two ion chambers filled with Ar and Kr were used as detectors of I_0 and I, respectively, and two ion chambers filled with N_2 100 % and Ar 15 % /N_2 85 % were used for the measurement of Ge K-edge spectra.

Extended X-ray absorption fine structure (EXAFS) analysis was carried out similarly as reported in section 2-2-3. For the curve fitting analysis, the empirical phase shift and amplitude

functions for Rh-Rh, Ge-Ge, Rh-O and Ge-O were extracted from the data for Rh metal, Ge metal, Rh_2O_3 and GeO_2 (hexagonal), respectively.

3-2-3 FT-IR Measurement

FT-IR spectra were measured on a JASCO FT-IR 230 spectrometer with 2 cm^{-1} resolution. The spectra were scanned and summed up by 128 times. The measurement was conducted in an *in-situ* IR cell combined in a closed circulating system. The sample was pressed into a wafer with diameter of 2 cm. Preparation and treatments of $Rh/GeO_2/SiO_2$ were carried out under *in-situ* conditions. The spectra for the adsorbed CO were obtained by subtracting the spectrum of gaseous CO from the spectrum measured under 13.3 kPa CO.

3-3 Results

3-3-1 Rh K-edge XAFS

Figure 1 shows the $k^3\chi(k)$ oscillations, their associated Fourier transforms and curve fitting analyses for the EXAFS data at Rh K-edge for $Rh/GeO_2/SiO_2$ (1) (Rh: 2.0 wt%) after oxidation and successive reduction treatments. The curve fitting results are listed in table 1. In the Fourier transform in figure 1 (B) (a') for the fresh calcined sample (1), two peaks were observed at 0.16 nm and 0.26 nm (phase shift uncorrected), which correspond to Rh-O and Rh-Rh bonds of Rh oxide, respectively. Similar results were also obtained on Rh/SiO_2 calcined at 673 K as shown in figure 3. By reducing the calcined sample at 423 K the two peaks disappeared and a single peak around 0.25 nm developed (Figure 1 (B) (b')). The peak was analyzed to be due to Rh-Rh bond by the curve fitting technique in figure 1 (C) (b"). The determined Rh-Rh distance (0.266 nm) in table 1 agrees with Rh-Rh nearest neighbor bond distance in Rh metal. After

further reduction at 523 K, the intensity became smaller (Figure 1 (B) (c')) and the intensity further decreased by reduction at 623 K (Figure 1 (B) (d')), which was accompanied by the shift of peak position to shorter length as shown in figure 1 (B) (b')-(d') and table 1. The curve fitting analysis was carried out for the inversely Fourier transformed data over 0.15-0.30 nm. When the peak was assumed to be composed of Rh-Rh alone, the calculated curve did not sufficiently reproduce the observed data. The observed EXAFS oscillation was successfully reproduced only by the addition of Rh-Ge bonding besides Rh-Rh bonding as shown in figure 1 (C). The distances of Rh-Rh and Rh-Ge bonds were determined at 0.264-0.266 nm and 0.236-0.242 nm, respectively in table 1. The above results suggest that the GeO_2 overlayers were partially reduced to Ge metal which incorporated into Rh metallic particles to form RhGe alloy particles by reduction with H_2 above 523 K.

Upon oxidation of the 723 K-reduced $Rh/GeO_2/SiO_2$ (1), the EXAFS feature changed drastically from figure 1 (A) (e) to figure 2 (A) (f) and from figure 1 (B) (e') to figure 2 (B) (f'). Destruction of the RhGe alloy particles to Rh oxides took place because the obtained spectra are similar to those measured for the calcined $Rh/GeO_2/SiO_2$ (1) after the first calcination step. However, the EXAFS oscillation (Figure 2 (A) (g)) and the Fourier transform (Figure 2 (B) (g')) for the $Rh/GeO_2/SiO_2$ (2) reduced at 423 K in the second cycle were entirely different from those (Figure 1 (A) (b) and Figure 1 (B) (b')) for the $Rh/GeO_2/SiO_2$ (1) reduced in the first cycle. The inversely Fourier transformed data were never fitted with single Rh-Rh wave, but were reproduced only by two-waves (Rh-Rh+Rh-Ge). The best fit results are shown in figure 2 (C) (g") and table 2. During the second reduction procedure, the intensity of the single peak in Fourier transform gradually increased with rise of the reduction temperature, which was accompanied with the shift of peak position to the shorter length. The tendency of the intensity change is reverse against that in the first reduction step. The curve fitting results in table 2 and figure 2 (C) showed the increase in the coordination number of Rh-Ge bond. The coordination number of Rh-Rh bond decreased with rise of the reduction temperature from 423

K to 523 K and kept nearly constant at 523-723 K. In every RhGe alloy particle on the $Rh/GeO_2/SiO_2$ (2) reduced at 423-723 K the fitted distances of Rh-Rh and Rh-Ge bonds remained constant as shown in table 2.

Figure 4 shows the Rh K-edge XANES spectra of $Rh/GeO_2/SiO_2$ (1) and (2). Gradual attenuation of the peak intensity was observed with an increase in the reduction temperature.

Figure 5 shows the EXAFS spectra for $Rh/GeO_2/SiO_2$ (1) reduced at 723 K (RhGe alloy) followed by contact with 13.3 kPa of dry oxygen (a) or 13.3 kPa of oxygen containing 1.3 kPa of H_2O vapor (b). These exposures were conducted at room temperature. The Fourier transform spectrum after exposure to dry oxygen showed two peaks which were analyzed to be due to Rh-O and Rh-Rh by the curve fitting technique as shown in figure 5 (a") and table 3. There was no contribution of Rh-Ge. The calculated Rh-Rh distance of 0.265 nm agrees with the bond distance of Rh metal. On the other hand, the spectrum (Figure 5 (b)) measured after contact with oxygen containing moisture was surprisingly different from the spectrum after contact with dry oxygen (Figure 5 (a)). The EXAFS analysis revealed Rh-O and Rh-Rh bonds at the distances of 0.207 nm and 0.276 nm, respectively, which correspond to those of Rh oxides [6].

3-3-2 Ge K-edge XAFS

To examine the behavior of the GeO_2 submonolayer on SiO_2 in oxidation and reduction, XAFS spectra at Ge K-edge were measured. Figure 6 shows the Fourier transforms of the EXAFS data for $Rh/GeO_2/SiO_2$ (1) with different Ge loadings of 1.3-7.4 wt% after reduction at 723 K. Growth of a new peak around 0.21 nm (phase shift uncorrected) was observed with decreasing Ge loading. To extract the oscillation from the new peak, the moieties of Ge-O and Ge-Ge which partially overlap in this region were extracted as follows. The Ge K-edge EXAFS oscillation for GeO_2/SiO_2 was subtracted from that for $Rh/GeO_2/SiO_2$ (1), where the

oscillations were normalized for Ge-O by multiplication of the ratio of Ge-O intensities calculated from the spectra of both samples. Figure 7 shows the k^3-weighted EXAFS difference spectra thus obtained. As for the 3.2 wt% GeO_2 sample the S/N ratio of the spectrum was low, and the oscillation only over 40-100 nm^{-1} was presented in figure 7. I have applied Ge-Ge or Ge-Rh wave to the extracted wave in the curve fitting analysis. The curve fitting results are shown in figure 7 and the fitted parameters are listed in table 4. Figure 7 (c") shows the fitting curve assuming Ge-Ge bonding, but the Ge-Ge wave did not fit with the extracted oscillation. The reasonable result was attained by Ge-Rh bonding (Figure 7 (c')). The bond distance for Ge-Rh in Rh/1.3 wt% GeO_2/SiO_2 was calculated to be 0.239 nm (Table 4), which is close to the distance (0.240 ± 0.003 nm) for Rh-Ge determined from the Rh K-edge EXAFS. Thus it is evident that RhGe alloy particles with direct Rh-Ge bonds were produced. In table 4, the curve fitting results of $Rh/GeO_2/SiO_2$ (1) with other Ge loadings are also listed. The results show the increase in the coordination number of Ge-Rh with a decrease of Ge loading, while the Ge-Rh bond distance is almost constant.

X-ray absorption near-edge structure provides more information about the valence state of Ge atoms in $Rh/GeO_2/SiO_2$ (1). Figure 8 (a)-(c) are the Ge K-edge XANES spectra of GeO_2/SiO_2, $Rh/GeO_2/SiO_2$ (1) reduced at 723 K, and Ge powder. Although the position of the threshold did not change after the deposition of Rh on the GeO_2/SiO_2 and after the reduction of the $Rh/GeO_2/SiO_2$ at 723 K, a small shoulder appeared around 11107 eV in the reduced $Rh/GeO_2/SiO_2$ (1). To see more clearly the shoulder structure, I differentiated the spectra against photon energy as shown in figure 8 (d)-(f). The shoulder structure appeared at 11105 eV in the first derivative of the XANES spectrum of $Rh/GeO_2/SiO_2$ (1), which corresponds to the peak position the Ge metallic powder, indicating the presence of Ge atoms probably in the metallic state in the reduced $Rh/GeO_2/SiO_2$ (1).

On the other hand no reduction occurred with GeO_2/SiO_2 without Rh as evidenced by the XANES of figure 8 (e) and the EXAFS of figure 6 (a). The reduction of GeO_2/SiO_2 may occur

by spillover hydrogen coming from Rh metal particles.

The RhGe alloy particles in $Rh/GeO_2/SiO_2$ (1) reduced at 723 K were reoxidized with O_2 at 673 K to form Rh oxide (denoted as RhO_x) and GeO_2. Interestingly, no X-ray diffraction pattern due to GeO_2 particles was observed. I measured Ge K-edge EXAFS spectra of the $Rh/GeO_2/SiO_2$ sample reoxidized with O_2 at 673 K. I also measured the EXAFS of the reoxidized Rh/1.3 wt% GeO_2/SiO_2 sample, because Ge-Rh bonding was clearly detected with the reduced state of this sample as shown in figure 6 (e) and table 4. Figure 9 shows the k^3-weighted EXAFS oscillations and their Fourier transforms of Rh/1.3wt% GeO_2/SiO_2 after oxidation at 673 K, reduction at 723 K, and reoxidation at 673 K. From comparison of figure 9 (a) and (c), it is concluded that the RhGe bimetallic particles in the reduced sample are destroyed and the initial $RhO_x/GeO_2/SiO_2$ was recovered in the reoxidized sample (2). No increase in Ge-Ge peak intensity in figure 9 (c) compared to that in figure 9 (a) indicates the regeneration of the original GeO_2 overlayer structure without aggregation to GeO_2 bulk particles. The regeneration of the submonolayer structure after the reoxidation was also supported by IR observation of surface OH groups on the GeO_2 layer. The intensity of ν(GeO-H) peaks did not change between the original calcined $Rh/GeO_2/SiO_2$ sample (1) and the reoxidized sample (2) after the reduction at 723 K.

3-3-3 Particle Size Distribution by TEM

The size distributions of Rh particles in $Rh/GeO_2/SiO_2$ (1) reduced at 423 K and 723 K and $Rh/GeO_2/SiO_2$ (2) reduced at 723 K in the second oxidation -reduction cycles were estimated by transmission electron microscope (TEM). The histograms of size distribution of the particles are shown in figure 10. The size distribution was somewhat narrower with the sample reduced at 723 K than with the 423 K-reduced sample. The average particle sizes are 2.0 nm, 2.1 nm and 2.3 nm for the samples reduced at 423 K (first), 723 K (first) and 723 K (second),

respectively. The average size and size distribution of the Rh particles were preserved after the repeated treatments of oxidation at 673 K and reduction at 723 K.

3-3-4 Observation of CO Adsorbed on $Rh/GeO_2/SiO_2$ by FT-IR

Figure 11 shows the FT-IR spectra of adsorbed CO on $Rh/GeO_2/SiO_2$ (1) reduced at 423-723 K and on Rh/SiO_2 reduced at 723 K. The spectra were measured under 13.3 kPa of CO. In the CO spectrum for Rh/SiO_2, three kinds of peaks appeared. An intense peak at 2080 cm^{-1} can be assigned to linear CO on Rh , and a peak at 2036 cm^{-1} and a shoulder peak at 2105 cm^{-1} can be assigned to the symmetric and asymmetric stretching modes of geminal CO species, respectively. A broad peak at 1870 cm^{-1} is assignable to the bridge CO on neighboring Rh sites. On $Rh/GeO_2/SiO_2$ (1) reduced at 423 K there existed a linear CO peak and small bridge and geminal CO peaks. After reduction above 523 K, the bridge and geminal CO species disappeared completely. The peak position of linear CO, 2075 cm^{-1} is lower by 5 cm^{-1} than that observed with Rh/SiO_2. On the sample (2) reduced after reoxidation, CO adsorbed in the linear form. The intensity and position of the linear CO peaks were the same as those in the first reduction step.

Figure 12 shows the change of the amount of adsorbed CO measured under 13.3 kPa CO at 273 K. The adsorbed amounts were determined by subtracting the amount of physisorbed CO in the second measurement from the adsorbed amount observed in the first measurement. Although a higher value was recorded after the first reduction of $Rh/GeO_2/SiO_2$ at 423 K, the measured amounts were among CO/Rh=0.3～0.4 independent of the reduction temperature and the repeated treatment.

3-3-5 Rh K-edge and Ge K-edge XAFS for Rh/bulk-GeO_2

XAFS spectra for Rh/bulk-GeO_2 reduced at 723 K were also measured at both Rh and Ge edges. Rh K-edge EXAFS spectra and the curve fitting analysis are shown in figure 13. The determined parameters are listed in table 5. Although the spectrum is a little noisy because of the large X-ray absorption coefficient due to the bulk GeO_2 support compared with the GeO_2 submonolayer/SiO_2, the curve fitting in figure 13 (c) was successfully performed and indicated RhGe alloy formation (Table 5). The Rh-Ge distance was determined as 0.246 nm, which is longer than the observed Rh-Ge bond (0.240 nm) distance in the RhGe alloy particles on the GeO_2 layer/SiO_2.

EXAFS spectra at Ge K-edge and the curve fitting analysis are shown in figure 14. Besides two peaks attributed to Ge-O and Ge-O-Ge bonds, which are originally seen in GeO_2, a new peak appeared at 0.21 nm (phase shift uncorrected). The curve fitting analysis with three waves (Ge-O and two Ge-Ge bonds) was achieved in figure 14 (c). In contrast to the case of Rh/GeO_2/SiO_2 the addition of Ge-Rh parameter did not give any good fitting. The determined distance of 0.246 nm corresponds to the Ge-Ge distance in Ge metal. On the other hand, the similar reduction treatment of bulk GeO_2 without Rh did not cause any change in both XANES and EXAFS spectra. The reduction of GeO_2 is possible by the coexistence of Rh metal particles.

3-3-6 Observation of CO Adsorbed on Rh/bulk-GeO_2 by FT-IR

Figure 15 shows FT-IR spectra of adsorbed CO on Rh/bulk-GeO_2 reduced at 423 K (a) and at 523 K (b), and successively calcined at 673 K followed by reduction at 423 K (c). A linear CO peak at 2074 cm^{-1} was observed after reduction at 423 K. The peak position is almost the same as that for the RhGe alloy particles on the GeO_2 layer/SiO_2. The linear CO peak almost

disappeared by reduction at 523 K, which was accompanied by the decrease of Ge-OH peak. At the same time, the transparency of IR beam became much worse, probably because Ge metal was formed on the surface of bulk GeO_2 as characterized by the Ge K-edge EXAFS. After calcination at 673 K and reduction at 423 K, the Ge-OH intensity recovered nearly to the initial level, but CO did not adsorb on the sample any more as shown in figure 15 (c), which indicates irreversible behavior of Rh particle on bulk GeO_2. This result is contrasted to that on $Rh/GeO_2/SiO_2$ which showed the reversible behavior of Rh/GeO_2 overlayer on SiO_2 in the repeated oxidation-reduction treatments.

3-4 Discussion

3-4-1 RhGe Alloy Formation on GeO_2 submonolayer

GeO_2/SiO_2 was not reduced by H_2 at 723 K, whereas in the presence of Rh the partial reduction of the submonolayer GeO_2 on SiO_2 took place even at 423 K. As a result of the reduction, Rh-Ge bimetallic particles were formed on the GeO_2/SiO_2 as characterized by EXAFS at Rh K-edge (Figures 1 and 2, Tables 1 and 2) and at Ge K-edge (Figures 6 and 7, and Table 4) and XANES (Figure 8). The Rh-Ge bond distance was determined as 0.240 ± 0.003 nm, which was independent of the reduction temperature (423-723 K), the Ge loading up to 7.4 wt% and the repetition of oxidation-reduction treatments. The determined bond length is much shorter than those (0.252-0.257 nm) of intermetallic compounds of Rh-Ge such as Rh_2Ge, RhGe and $RhGe_4$ [7-9]. The length is also much shorter than the sum (0.257 nm) of the metallic radii of both elements, i.e., 0.12249 nm for Ge and 0.13451 nm for Rh metal. This fact indicates that the Rh-Ge bonding in the RhGe alloy particles on GeO_2/SiO_2 has a covalent character rather than a metallic one. Furthermore, it is to be noted that the Rh-Rh bond length 0.266 ± 0.003 nm $Rh/GeO_2/SiO_2$ (1) reduced at 423 K in the first reduction process is similar

to the Rh-Rh bonding in Rh foil and is not so affected by the Rh-Ge bonding. The Rh-Rh distance in the $Rh/GeO_2/SiO_2$ (2) reduced at 723 K in the second reduction process decreases to 0.262 nm. This means that the RhGe bimetal does not form solid solution structure, but probably the RhGe bimetallic phase is gradually formed from the surface of the Rh particles on GeO_2/SiO_2 during the reduction.

While the covalent Rh-Ge bond character was suggested from EXAFS, the linear CO peak shifted only by 4 cm^{-1} by RhGe alloy formation as shown in figure 11. The electronic effect of Ge on Rh seems small or negligible in the RhGe particles generated on the GeO_2 layer/SiO_2. The result is different from that observed on RhSn alloy particles on SiO_2, where the CO peak shift as large as 50 cm^{-1} to lower wavenumber was observed probably due to the electronic modification of Rh by Sn [10-12].

Recently, the structure and catalysis of supported Rh or Ru catalysts doped with Ge have been studied extensively [13-24]. In these studies, a significant decrease in the peak intensity in Fourier transforms of Rh or Ru K-edge EXAFS spectra for Rh or Ru/SiO_2 by the addition of Ge is observed, which is similar to my present observation in figure 1. Because direct Rh-Ge or Ru-Ge bond was not detected except for one sample, it was concluded that the intensity change was brought from the scission and redispersion of the metal particles to small clusters composed of only ten atoms or so as a result of the Ge addition [13-24]. On the contrary, in the present $Rh/GeO_2/SiO_2$ system the averaged size and size distribution of the Rh particles determined by TEM did not show significant difference among the samples (1) reduced at low and high temperatures and the sample (2) reduced again after calcination as shown in the histograms of figure 10. The decrease in the intensity of the EXAFS Fourier transform after the high temperature reduction should be referred to the alloy formation of Rh with Ge. One explanation to this is the cancellation of EXAFS oscillations by overlapping of Rh-Ge and Rh-Rh waves when RhGe alloy particles are formed. The slight increase of peak intensity in the Fourier transforms during the second reduction treatments in figure 2 may be due to the increase

in the coordination number of Rh-Ge bond in the RhGe alloy particles as shown in table 2.

The new feature is also observed in the EXAFS spectra measured at Ge K-edge for Rh/1.3-7.4 wt% GeO_2 layers/SiO_2 (1) reduced at 723 K (Figures 6-8). The curve fitting analysis for the new peak around 0.21 nm (phase shift uncorrected) in figure 6 by Ge-Ge wave was unsuccessful and the best fit results were obtained by the curve fitting analysis by Ge-Rh wave as shown in figure 7. The formation of metallic Ge is also confirmed by XANES (Figure 8). These results mean that the reduced Ge atoms do not remain on the SiO_2 support but incorporate into the Rh particles. The Ge-Rh intensity grew as the Ge loading in GeO_2/SiO_2 decreased (Table 4). This means that the portion of Ge incorporated to the Rh particles in GeO_2 on SiO_2 increases as the Ge loading decreases because the EXAFS technique gives the averaged information on the structure around a specific element. The Rh particles may be located closely with the GeO_2 submonolayers on SiO_2 and probably located on the GeO_2 layers. Otherwise, the portion of reduced GeO_2 in the 1.3 wt% GeO_2/SiO_2 would have been smaller unlike the result.

The Rh K-edge EXAFS data of the reduced Rh/GeO_2/SiO_2 (1) demonstrate that Rh-O bond and metallic Rh-Rh bond appear by exposing to dry oxygen at room temperature, and hence that the surface of the RhGe alloy particles is oxidized. The reason of the resistance to oxidation of inner Rh under dry oxygen may be due to the existence of Ge which prevents the particle being further oxidized. The oxidation of Rh to Rh oxide at room temperature occurred by contact with oxygen containing moisture as evidenced by EXAFS (Figure 5 and Table 3). Deep oxidation of the RhGe alloy particles was also observed with Ge which was converted to 3-dimensional crystalline GeO_2.

3-4-2 Behavior of Ge in Rh/GeO_2/SiO_2 in Oxidation and Reduction

Several experiments were carried out to study the behavior of Ge in the Rh/GeO_2/SiO_2

sample during repeated oxidation and reduction treatments. The reoxidation of the reduced $Rh/GeO_2/SiO_2$ (1) at 673 K destroyed the RhGe alloy structure as shown in figures 1 and 2. The results of EXAFS and XRD indicate that the RhGe alloy particles on the GeO_2 submonolayers supported on SiO_2 are transformed to the original Rh oxides on the GeO_2 overlayers on SiO_2 again. No three-dimensional GeO_2 particles were formed by repeated reduction-oxidation cycles. The structural change in the reduction and oxidation is illustrated in figure 16. This structure change is unique by the following reasons. Bulk GeO_2 particle is more stable than the submonolayer GeO_2 on SiO_2 because the submonolayer GeO_2 was only formed by the reaction of $Ge(OMe)_4$ vapor surface OH groups of SiO_2, followed by calcination at 673 K, and was never produced by the solid state reaction between GeO_2 and SiO_2 at high temperatures. In fact, once 3-dimensional GeO_2 particles were formed from the GeO_2 overlayer by exposing to H_2O vapor, they were stable against any treatment and were not converted to the original submonolayer GeO_2. The monolayer GeO_2 may be a thermodynamically metastable state. It has been demonstrated that volatile GeO (sublimation temperature 983 K [25]) is formed in the oxidation of CuGe alloy where Ge segregates on the surface [26]. In the RhGe particles on the GeO_2 submonolayers supported on SiO_2, $[GeO]_n$ may also be formed at the beginning of the oxidation and chemically attached on the SiO_2 surface to form the GeO_2 submonolayers. The transformation between $RhO_x/SiO_2/GeO_2$ and $RhGe/GeO_2/SiO_2$ reversibly takes place as illustrated in figure 16.

3-4-3 Comparison of $Rh/GeO_2/SiO_2$ and $Rh/bulk\text{-}GeO_2$

The most distinct difference in the behavior of Rh particles on the GeO_2 submonolayer on SiO_2 and bulk on GeO_2 is attributed to the reversibility of the formation of RhGe alloy particles under the reduction conditions. On the GeO_2/SiO_2, RhGe alloy particles were reversibly reproduced by the oxidation-reduction treatments as characterized by EXAFS. It is also

confirmed by the FT-IR spectra of adsorbed CO on the $Rh/GeO_2/SiO_2$ (1) and (2) which were identical between the first and second reduced samples as shown in figure 11 (d) and (e), respectively. The size distributions of the RhGe particles in these two samples are also almost the same as indicated in the TEM images of figure 10 (b) and (e).

When Rh/bulk-GeO_2 was reduced at 723 K, RhGe alloy particles were formed as proved by EXAFS (Figure 14 and Table 5), but the alloy surface is different from that of the $Rh/GeO_2/SiO_2$ as shown in figure 15. The spectrum of Rh/GeO_2 reduced at 423 K shows a linear CO peak at 2074 cm^{-1} which is similar to that observed on the reduced $Rh/GeO_2/SiO_2$ in figure 11. However, CO does not adsorb on Rh/GeO_2 after reduction at 523 K. The decrease of surface OH groups on the GeO_2 and the simultaneous reduction of IR transparency imply that the reduction of GeO_2 to metallic Ge occurs mainly on the surface in this condition. After calcination of the 523 K-reduced sample, followed by reduction at 423 K, no CO peak appeared as shown in figure 15. Thus the CO adsorption experiments also reveal the irreversible behavior of Rh on the bulk GeO_2 in the reduction-oxidation treatments. The RhGe alloy formation (Rh-Ge=0.246 nm) is evident from the EXAFS analysis at Rh K-edge (Table 5) and metallic Ge is also characterized by EXAFS at Ge K-edge (Figure 14 and Table 5). The Ge-OH groups reappears by reoxidation of the 523 K-reduced Rh/GeO_2 (Figure 15), indicating the oxidation of the metallic Ge to Ge oxides, whereas the subsequent reduction of the oxidized sample at 423 K never recovers the adsorption capacity for CO. Accordingly, it is likely that Rh forms RhGe alloy particles with the produced metallic Ge in the reduction conditions and the alloy particles incorporate into the GeO_2 bulk or at least below the surface, which can not come up to the GeO_2 surface. The behaviors of Rh and Ge on bulk GeO_2 is in much contrast to those on the submonolayer GeO_2. The difference between the two systems is attributed to the difference in easiness on the reduction between the bulk GeO_2 and the submonolayer GeO_2/SiO_2. The GeO_2 submonolayers are chemically attached on SiO_2 surface making Ge-O-Si bonds which regulate the reducibility of the GeO_2 species and the population of Ge atoms reduced and supplied to

form RhGe alloy particles.

3-5 Conclusions

(1) By using a Rh dimer $[Rh(C_5Me_5)Me]_2(\mu\text{-}CH_2)_2$ as precursor, Rh was supported on the GeO_2 submonolayers attached on SiO_2 to study how the GeO_2 layers are perturbed through the interaction with deposited Rh.

(2) The EXAFS analysis at both Rh and Ge K-edges revealed RhGe alloy formation by reduction with H_2 at 423-723 K, accompanied by the partial reduction of the GeO_2 submonolayers.

(3) While a part of GeO_2 layers is incorporated into the RhGe alloy particles, the other part of GeO_2 retains its submonolayer structure.

(4) The reversible behaviors of Rh and Ge in the reduction and oxidation steps were characterized by XAFS, XRD, TEM and FT-IR. Metallic Rh and Ge form RhGe alloy particles on the GeO_2/SiO_2 during reduction, and the Ge atoms alloyed with Rh come back to the GeO_2 submonolayers on SiO_2 by calcination of the alloy. The Rh atoms are reversibly transformed between RhGe alloy particles and Rh oxides on the GeO_2/SiO_2 surface.

(5) The reversible behavior of Rh in the $Rh/GeO_2/SiO_2$ sample is in contrast to the behavior of Rh in the Rh/bulk GeO_2 where Rh species are irreversibly transformed to RhGe alloy particles in the bulk GeO_2.

3-5 References

[1] K. Asakura and Y. Iwasawa, *J. Phys. Chem.*, **96** (1992) 7386.

[2] K. Asakura and Y. Iwasawa, *Chem. Lett.*, (1988) 633.

[3] A. Kase, K. Asakura, C. Egawa and Y. Iwasawa, *Chem. Lett.*, (1986) 855.

[4] K. Asakura, J. Inukai and Y. Iwasawa, *J. Phys. Chem.*, **96** (1992) 829.

[5] K. Asakura, K. Bando, Y. Iwasawa, H. Arakawa and K. Isobe, *J. Am. Chem. Soc.*, **112** (1990) 9098.

[6] J. B. A. D. van Zon, D. C. Koningsberger, H. F. J. van't Bilk and D. E. Sayers, *J. Chem. Phys.*, **82** (1985) 5742.

[7] S. Geller, *Acta Cryst.*, **8** (1955) 15.

[8] P. Villars and L. D. Calvert, "*Person's Handbook of Crystallographic Data for Intermetallic Phases*" Vol. 3, The Materials Internation Society, 1991, P. 3774.

[9] V. I. Larchev and S. V. Popova, *J. Less-Common Metals*, **98** (1984) L1.

[10] K. Tomishige, K. Asakura and Y. Iwasawa, *J. Catal.*, **149** (1994) 70.

[11] B. Didillon, C. Houtman, T. Shay, J. P. Candy and J. -M. Basset, *J. Am. Chem. Soc.*, **115** (1993) 9380.

[12] J. P. Candy, O. A. Ferretti, G. Mabilon, J. P. Bournonville, A. El Mansour, J. -M. Basset and G. Martino, *J. Catal.*, **115** (1988) 210.

[13] M. C. S. Sierra, J. G. Ruiz and M. G. Proietti, *J. Mol. Catal.*, **96** (1995) 65.

[14] J. J. Rehr, J. M. Leon, S. I. Zabinsky and R. C. Albers, *J. Am. Chem. Soc.* **113** (1991) 5135.

[15] B. Coq, E. Crabb, M. Warawdekar,G. C. Bond, J. C. Slaa, S. Galvagno, L. Mercadante, J. G. Ruiz, M. Conception and S. Sierra, *J. Mol. Catal.*, **92** (1994) 107.

[16] B. Coq, A. Goursot, T. Tazi, F. Figuéras and D. R. Salahub, *J. Am. Chem. Soc.*, **113** (1991) 1485.

[17] G. C. Bond and J. C. Slaa, *J. Mol. Catal.*, **101** (1995) 243.

[18] G. C. Bond and J. C. Slaa, *J. Mol. Catal.*, **89** (1994) 221.

[19] G. C. Bond and J. C. Slaa, *J. Mol. Catal. A: Chemical*, **98** (1995) 81.

[20] G. C. Bond and J. C. Slaa, *J. Mol. Catal.*, **96** (1995) 163.

[21] A. Goursot, L. Pedocchi and B. Coq, *J. Phys. Chem.*, **98** (1994) 8747.

[22] A. Goursot, B. Coq, L. de Ménprval, T. Tazi, F. Figueras and D. R. Salahub, *Z. Phys. D-Atoms Molecules and Clusters*, **19** (1991) 367.

[23] G. Neri, L. Mercadante, C. Milone, R. Pietropaolo and S. Galvagno, *J. Mol. Catal. A: Chemical*, **108** (1996) 41.

[24] G. C. Bond and J. C. Slaa, *J. Mol. Catal. A: Chemical*, **106** (1996) 135.

[25] G. V. Samsonov (eds.) *"The Oxide Handbook"*, IFI/PLENUM, New York-Washington-London, 1973.

[26] T. S. S. Kumar and M. S. Hegde, *Surf. Sci.*, **150** (1985) L123.

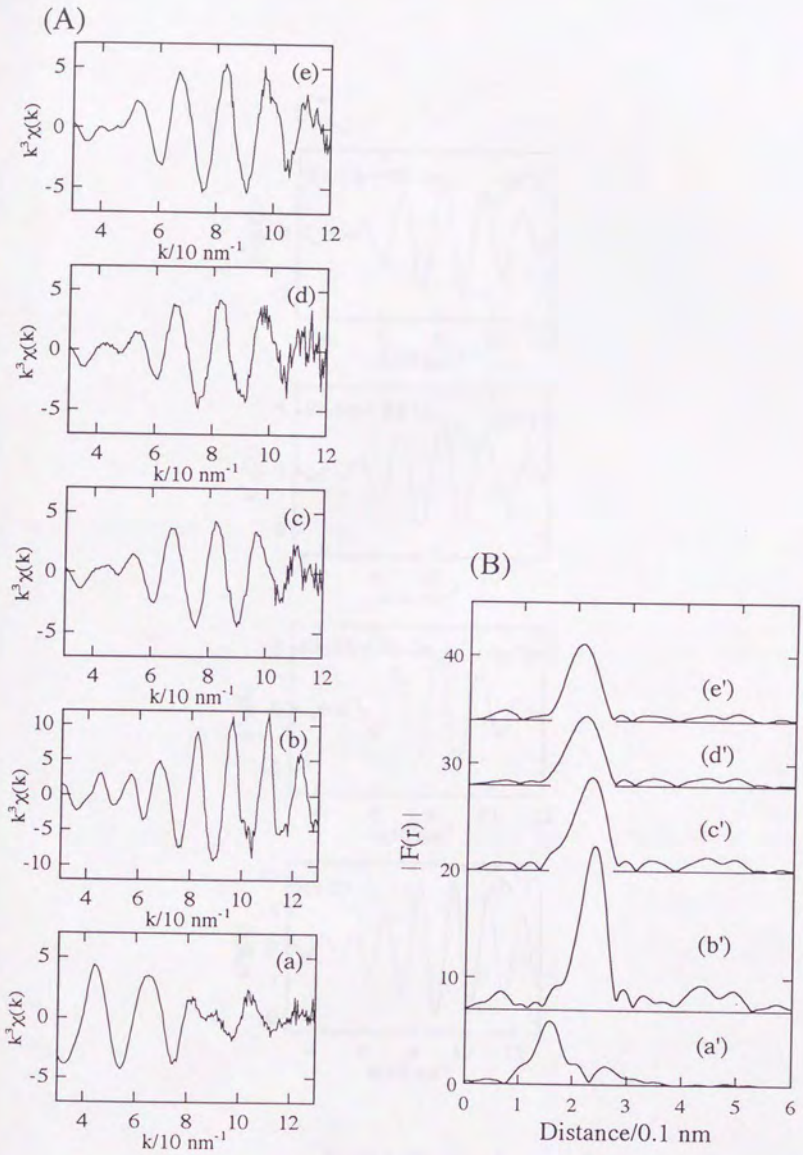

Figure 1. Rh K-edge EXAFS oscillations (A), their Fourier transforms (B), and curve fittings (C) for $Rh/GeO_2/SiO_2$ (1); (a, a') calcined at 673 K; (b, b', b") reduced at 423 K, (c, c', c") reduced at 523 K, (d, d', d") reduced at 623 K, (e, e', e") reduced at 723 K.

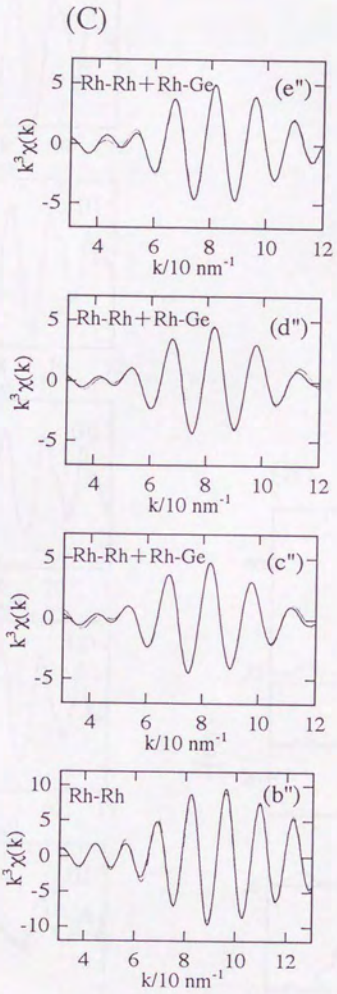

Figure 1. (Continued)

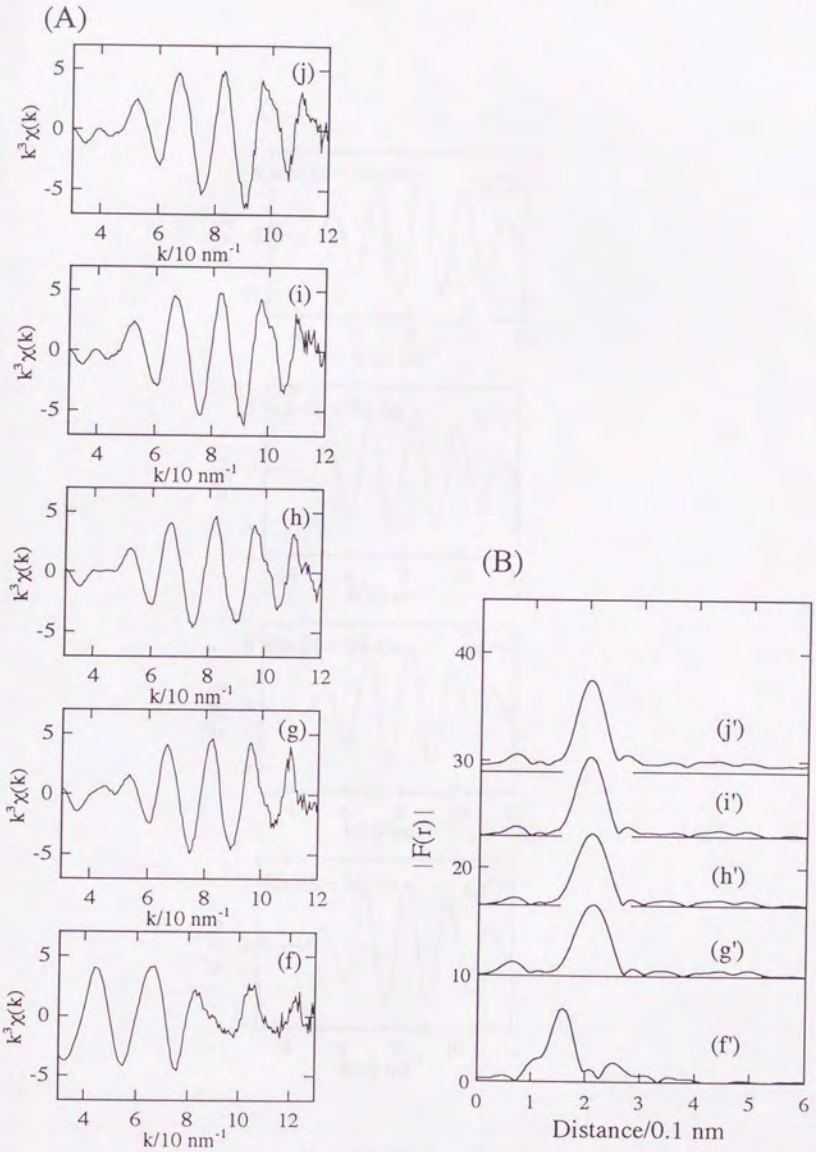

Figure 2. Rh K-edge EXAFS oscillations (A), their Fourier transforms (B), and curve fittings (C) for $Rh/GeO_2/SiO_2$ (2); (f, f') calcined at 673 K; (g, g', g") reduced at 423 K, (h, h', h") reduced at 523 K, (i, i', i") reduced at 623 K, (j, j', j") reduced at 723 K.

(C)

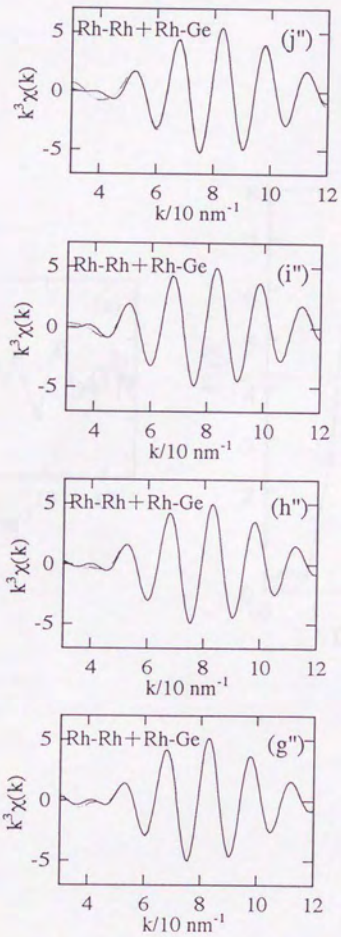

Figure 2. (Continued)

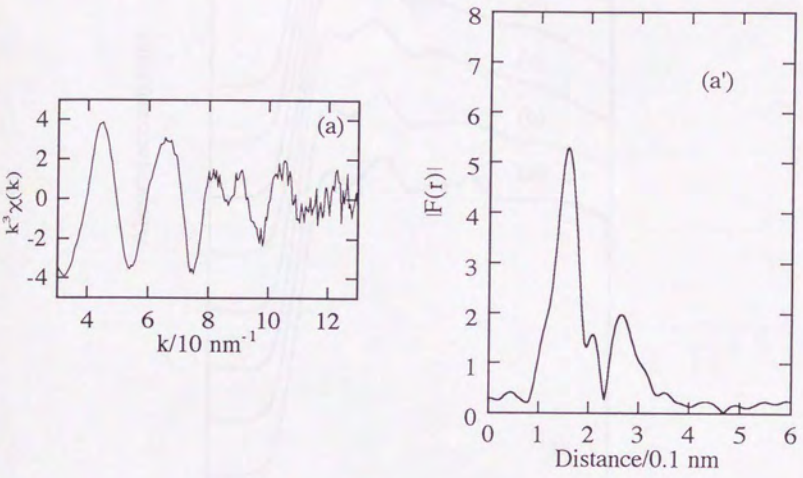

Figure 3. Rh K-edge EXAFS $k^3\chi(k)$ oscillations (a), their Fourier transforms (a') for Rh/SiO_2 (Rh: 2.0 wt%) calcined at 673 K; Deposition of Rh was carried out similarly on GeO_2/SiO_2.

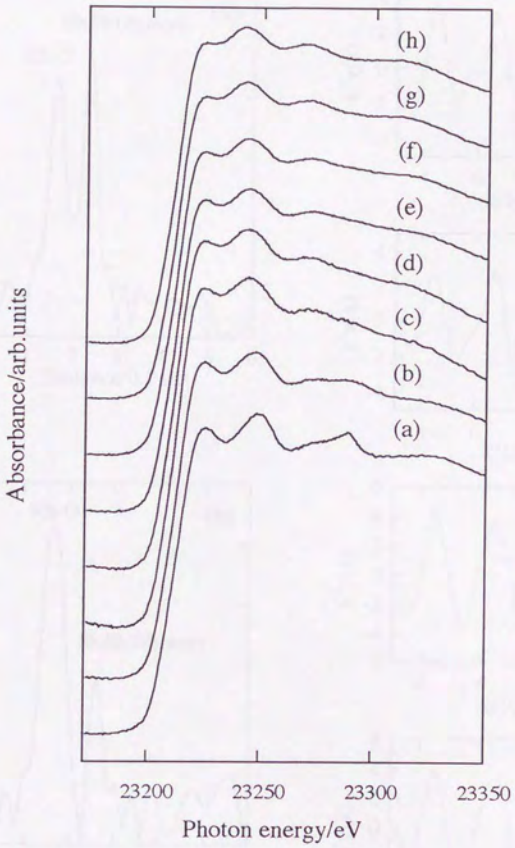

Figure 4. Rh K-edge XANES spectra for $Rh/GeO_2/SiO_2$ (1) (a-d) and $Rh/GeO_2/SiO_2$ (2) (e-h); reduced at (a, e) 423 K, (b, f) 523 K, (c, g) 623 K, (d, h) 723 K.

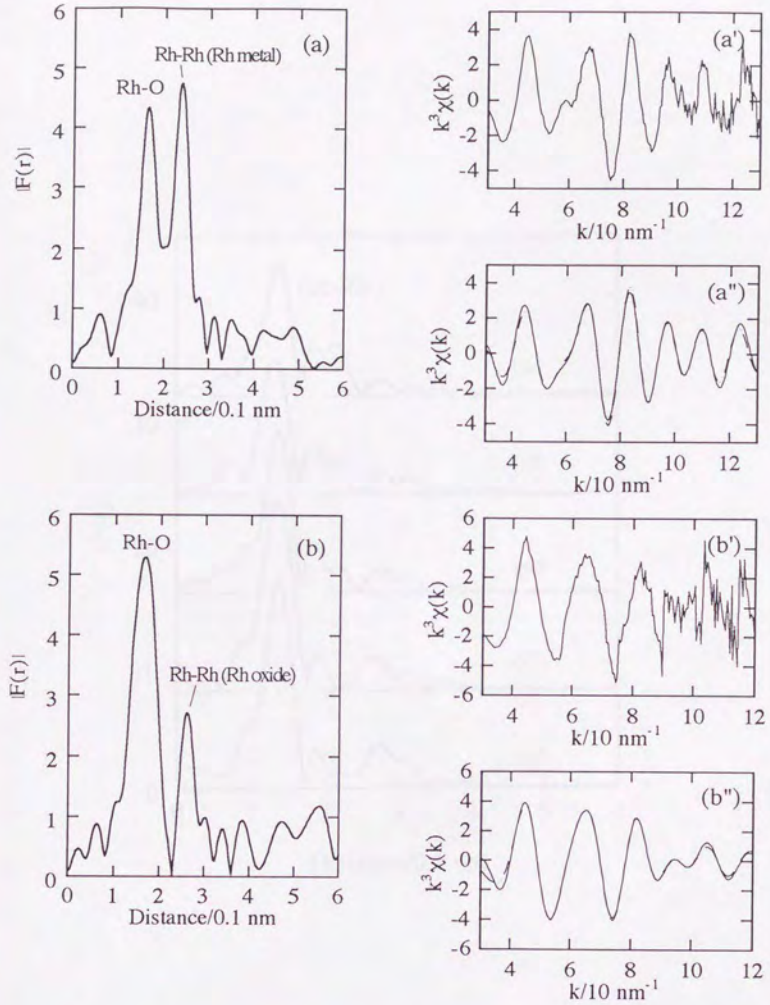

Figure 5. Rh K-edge XANES spectra for $Rh/GeO_2/SiO_2$ (1) reduced at 723 K followed by exposure to O_2 (a, a', a") and O_2 with H_2O vapor (b, b', b") at room temperature: (a, b) Fourier transforms, (a', b') $k^3\chi(k)$ and (a", b") curve fitting; (a") three-waves fitting (Rh-O, Rh-Rh and Rh-Rh); (b") two-waves fitting (Rh-O and Rh-Rh); solid line: observed, dotted line: calculated.

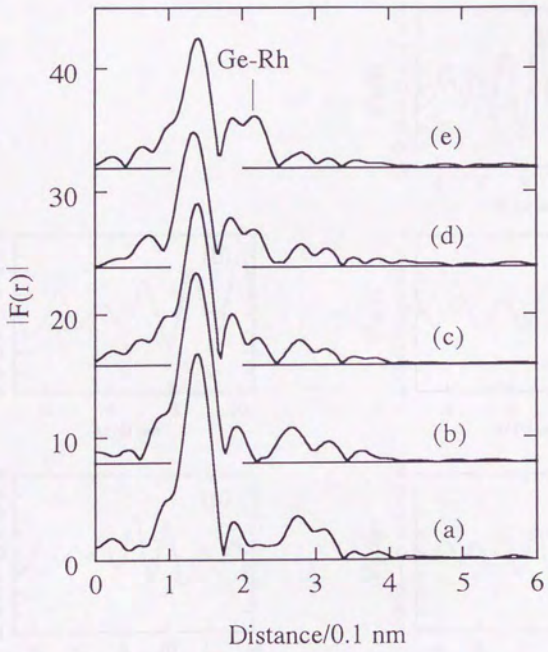

Figure 6.Ge K-edge EXAFS Fourier transforms for (a) GeO_2/SiO_2 (Ge 7.4 wt%), (b) GeO_2/SiO_2 (1) reduced at 723 K; $Rh/GeO_2/SiO_2$ reduced at 723 K: Ge loading (c) 7.4 wt%, (d) 3.2 wt% and (e) 1.3 wt%.

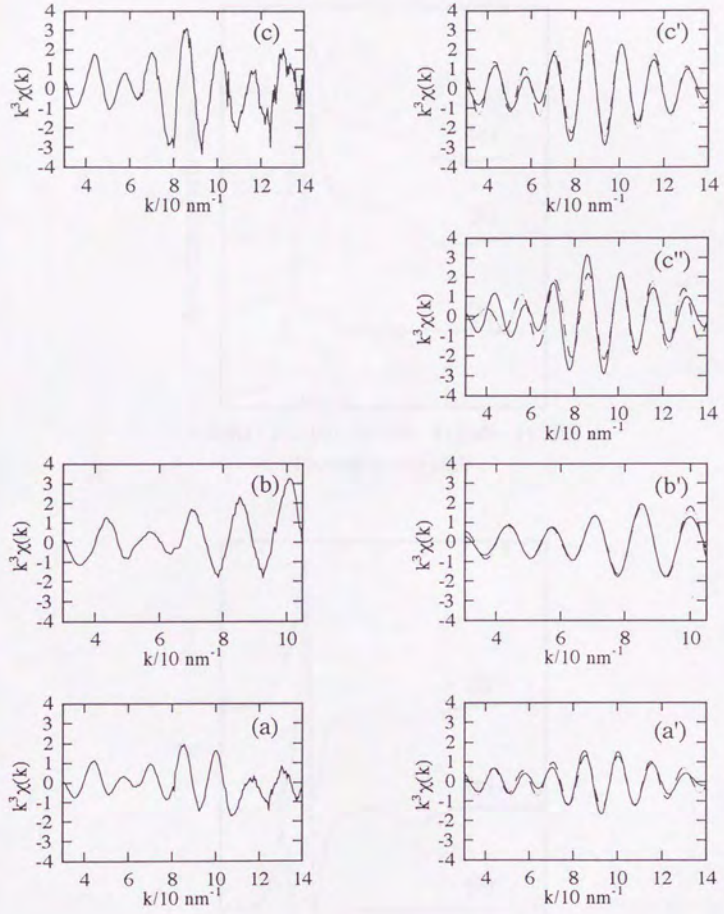

Figure 7. Ge K-edge EXAFS difference spectra after subtraction of the Ge-O oscillation in $Rh/GeO_2/SiO_2$ (1) reduced at 723 K; Ge loading: (a) 7.4 wt%, (b) 3.2 wt%, (c) 1.3 wt%; (a'), (b') and (c'): curve fitting analysis with Ge-Rh single wave; (c''): curve fitting trial by assuming Ge-Ge single wave; solid line: observed, dotted line: calculated.

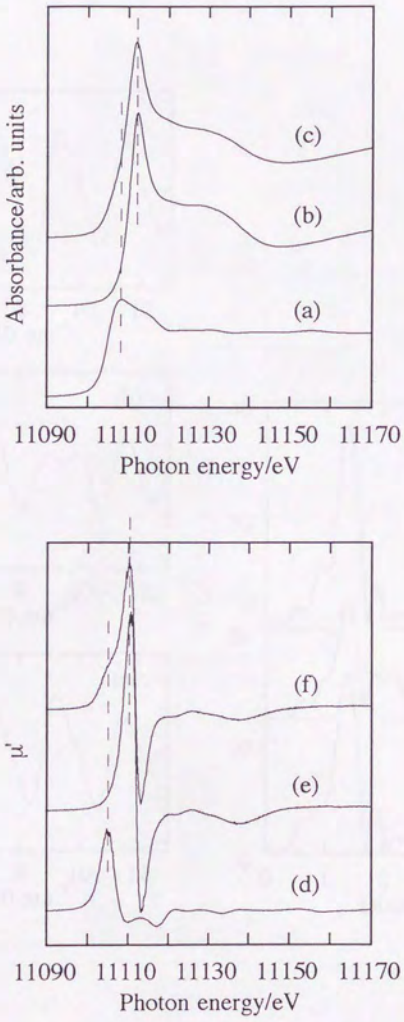

Figure 8. Ge K-edge XANES spectra (a, b, c) and their first derivatives (d, e, f) for Ge powder (a, d), GeO_2/SiO_2 (b, e), and $Rh/GeO_2/SiO_2$ (1) reduced at 723 K (c, f).

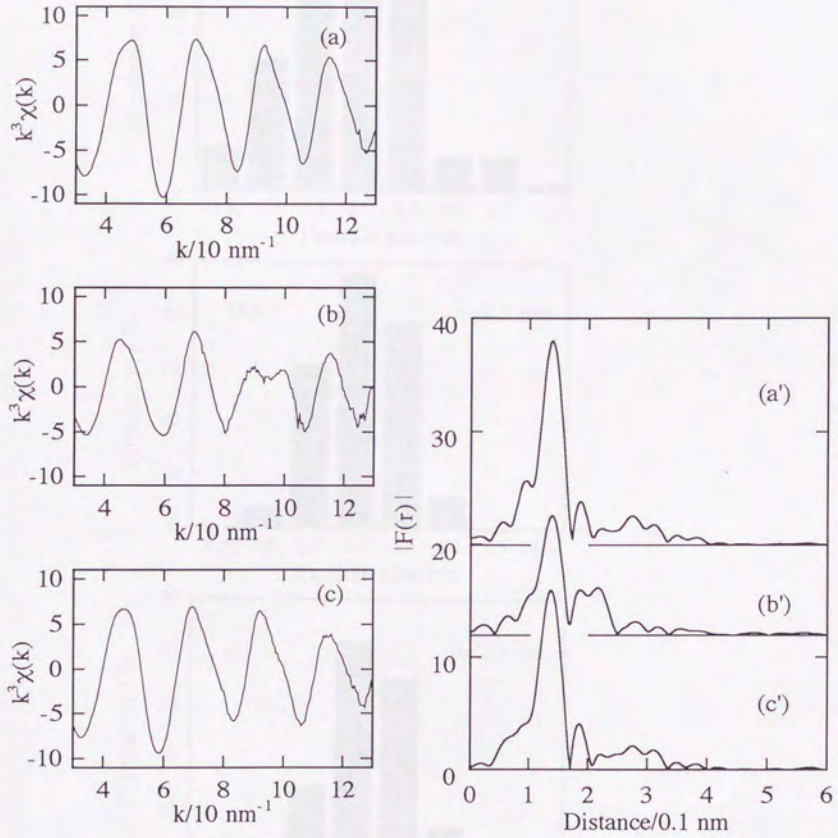

Figure 9. Ge K-edge EXAFS spectra for successively treated $Rh/GeO_2/SiO_2$ (Rh: 2.0 wt%, Ge: 1.3 wt%); (a), (a'): after incipient Rh deposition and calcination at 673 K; (b), (b'): after reduction at 723 K; (c), (c'): after reoxidation at 673 K; (a), (b), (c): Fourier transforms; (a'), (b'), (c'): $k^3\chi(k)$ oscillations.

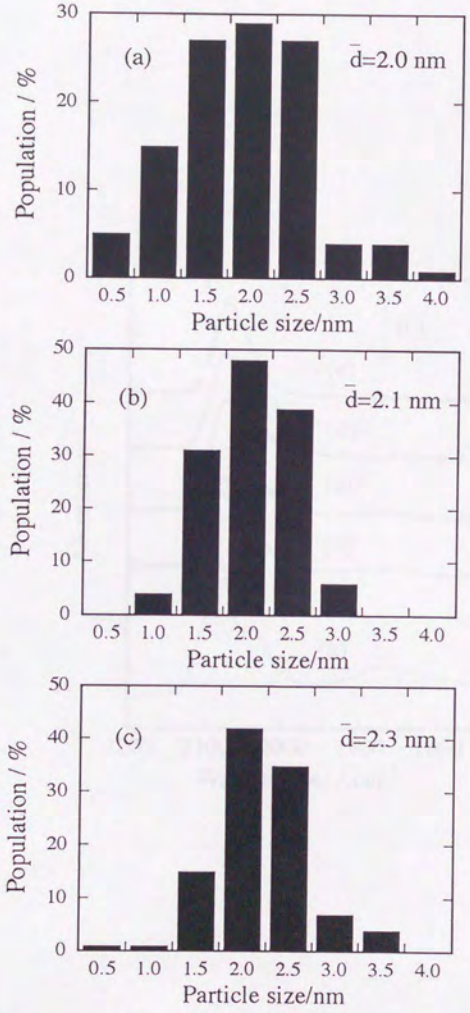

Figure 10. Size distributions of metal particles in $Rh/GeO_2/SiO_2$ by TEM; (a) after first reduction at 423 K, (b) after first reduction at 723 K, (c) after second reduction at 723 K after calcination of (b).

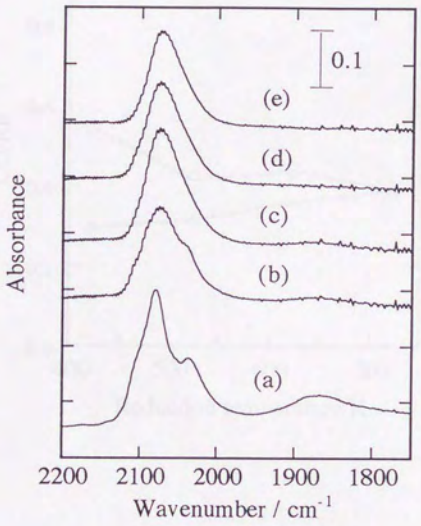

Figure 11. FT-IR spectra; (a) Rh/SiO_2 reduced at 723 K; $Rh/GeO_2/SiO_2$ (1) reduced at (b) 423 K, (c) 623 K, (d) 723 K; $Rh/GeO_2/SiO_2$ (2) reduced at (e) 723 K; CO: 13.3 kPa.

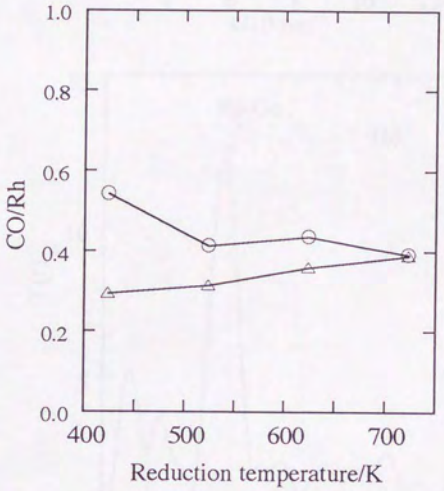

Figure 12. The amount of CO adsorbed on $Rh/GeO_2/SiO_2$ (1) (○) and (2) (△) as a function of the reduction temperature.

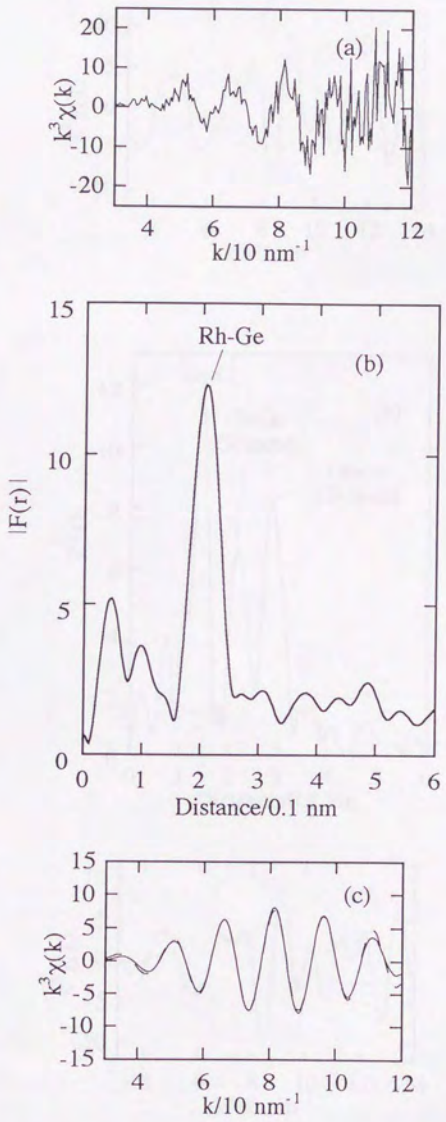

Figure 13. Rh K-edge EXAFS spectra for Rh/GeO_2 reduced at 723 K; (a) $k^3\chi(k)$ oscillation, (b) Fourier transform, (c) curve fitting analysis with Rh-Ge single wave; solid line: observed, dotted line: calculated.

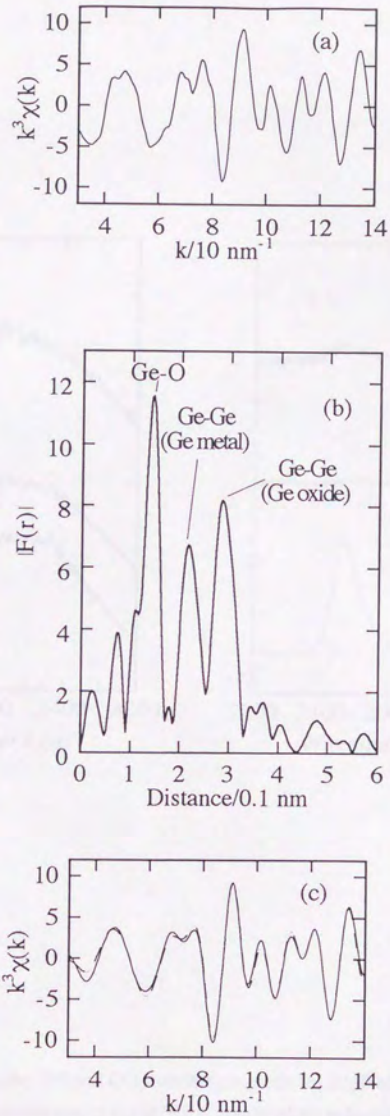

Figure 14. Ge K-edge EXAFS spectra for Rh/GeO_2 reduced at 723 K; (a) $k^3\chi(k)$ oscillation, (b) Fourier transform, (c) curve fitting analysis with three waves (Ge-O, Ge-Ge, Ge-Ge); solid line: observed, dotted line: calculated.

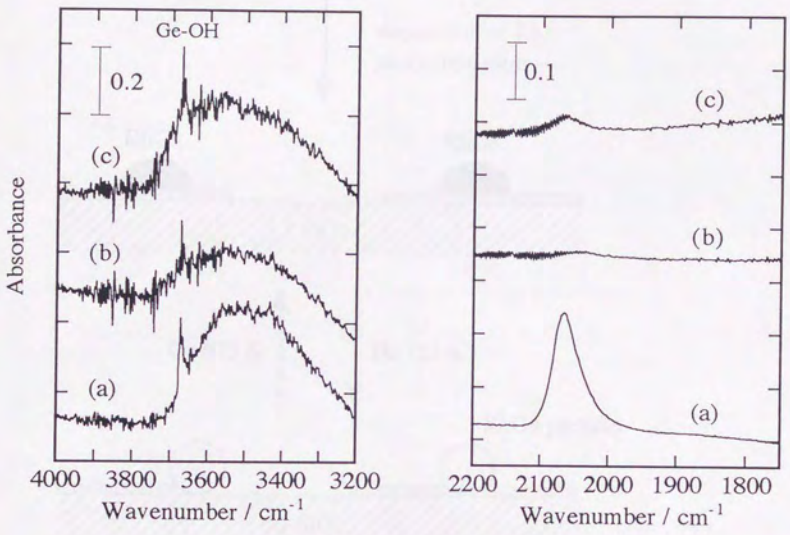

Figure 15. FT-IR spectra in the OH and CO stretching regions for Rh/GeO_2 reduced at 423 K (a) and at 523 K (b); (c) after calcination of (a) at 673 K followed by reduction at 423 K; The spectra were measured under 13.3 kPa of CO.

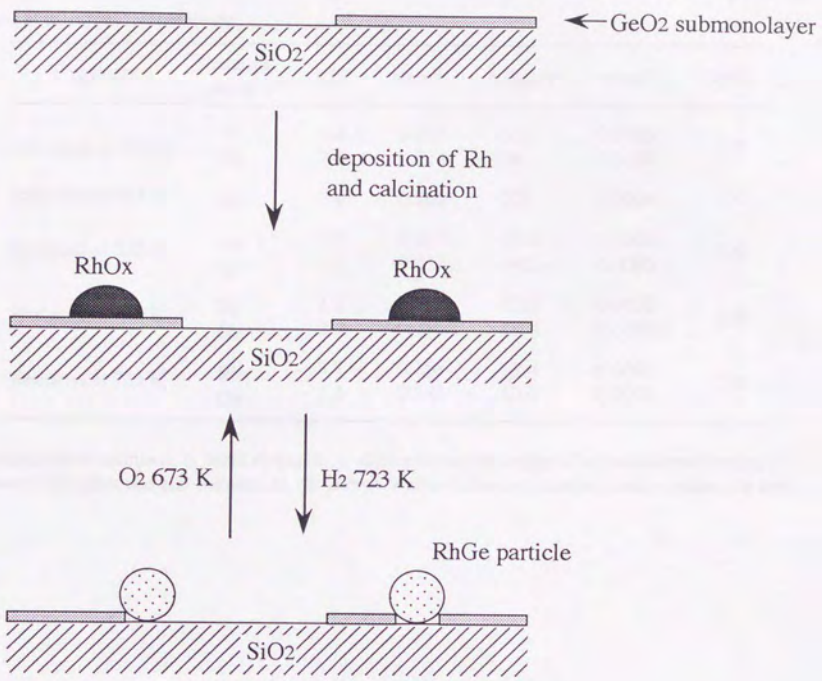

Figure 16. Proposed reversible structural change of Rh species and GeO_2 submonolayers during the reduction and oxidation treatments, where only the majority of the Rh and Ge species is illustrated.

Table 1. Curve fitting results of the Rh K-edge EXAFS data for 2.0 wt% Rh/7.4 wt% GeO_2/SiO_2 (1) reduced at different temperatures.

Treatment	Scatterer atom	CN[a]	r/nm[b]	ΔE_0/eV[c]	σ/nm[d]	Rf/%[e]
Oxidized at 673 K	O	6.3	0.202	-3.1	0.0089	1.7
	Rh	3.4	0.274	1.8	0.0124	
Reduced at 423 K	Rh	7.0	0.266	-7.3	0.0064	1.0
Reduced at 523 K	Rh	3.8	0.264	-13.0	0.0105	0.8
	Ge	1.2	0.237	-14.1	0.0085	
Reduced at 623 K	Rh	3.3	0.264	-15.0	0.0102	0.8
	Ge	2.4	0.236	-18.0	0.0073	
Reduced at 723 K	Rh	3.7	0.266	-12.4	0.0096	1.0
	Ge	1.4	0.242	-10.0	0.0093	

a: coordination number, b: bond distance, c: difference in the origin of photoelectron energy between the reference and the sample, d: Debye-Waller factor, e: residual factor defined in text.

Table 2. Curve fitting results of the Rh K-edge EXAFS data for 2.0 wt% Rh/7.4 wt% GeO_2/SiO_2 (2) reduced at different temperatures.

Treatment	Scatterer atom	CN[a]	r/nm[b]	ΔE_0/eV[c]	σ/nm[d]	Rf/%[e]
Oxidized at 673 K	O	9.2	0.204	-0.5	0.0116	4.1
	Rh	2.3	0.279	6.9	0.0106	
Reduced at 423 K	Rh	3.0	0.265	-14.0	0.0097	0.6
	Ge	1.6	0.241	-11.2	0.0093	
Reduced at 523 K	Rh	2.2	0.263	-18.0	0.0095	0.4
	Ge	1.9	0.241	-12.0	0.0092	
Reduced at 623 K	Rh	2.2	0.262	-16.0	0.0094	0.6
	Ge	2.2	0.238	-13.0	0.0090	
Reduced at 723 K	Rh	2.4	0.262	-14.0	0.0097	1.2
	Ge	2.4	0.239	-13.0	0.0100	

a: coordination number, b: bond distance, c: difference in the origin of photoelectron energy between the reference and the sample, d: Debye-Waller factor, e: residual factor defined in text.

Table 3. Curve fitting results of the Rh K-edge EXAFS spectra for 2.0 wt% Rh/7.4 wt% GeO_2/SiO_2 (1) reduced at 723 K and exposure to O_2 or a mixture of O_2 and H_2O vapor at room temperature.

Exposed gas	Scatterer atom	CN[a]	r/nm[b]	ΔE_0/eV[c]	σ/nm[d]	R_f/%[e]
O_2[f]	O	4.8	0.201	2.8	0.0106	0.6
	Rh	4.5	0.265	-6.1	0.0109	
O_2+H_2O[g]	O	8.7	0.207	2.8	0.0113	1.5
	Rh	2.7	0.276	4.9	0.0110	

a: coordination number, b: bond distance, c: difference in the origin of photoelectron energy between the reference and the sample, d: Debye-Waller factor, e: residual factor, f: O_2 (13.3 kPa) was exposed for 1 h, g: O_2 (13.3 kPa)+H_2O vapor (1.3 kPa) were exposed for 1 h.

Table 4. Curve fitting results of the Ge K-edge EXAFS spectra for 2.0 wt% $Rh/GeO_2/SiO_2$ (1) reduced at 723 K.

Ge loading /wt%	Scatterer atom	CN[a]	r/nm[b]	ΔE_0/eV[c]	σ/nm[d]	R_f/%[e]
1.3	Rh	1.1	0.239	-7.1	0.0086	7.4
(1.3)	(Ge)[f]	(0.7)	(0.250)	(-20.3)	(0.0056)	(25.8)
3.2	Rh	0.7	0.242	-3.6	0.0081	3.1
7.4	Rh	0.5	0.240	-5.4	0.0082	9.9

a: coordination number, b: bond distance, c: difference of the origin of photoelectron energy between the reference and the sample, d: Debye-Waller factor, e: residual factor, f: Ge-Ge bonding was assumed.

Table 5. Curve fitting results of the Rh and Ge K-edge EXAFS data for Rh/bulk-GeO_2 reduced at 723 K

Absorber atom	Scatterer atom	CN[a]	r/nm[b]	ΔE_0/eV[c]	σ/nm[d]	R_f/%[e]
Rh	Ge	4.9	0.246	-6.1	0.0088	1.6
	O	2.1	0.205	-7.1	0.0086	
Ge	Ge	1.0	0.246	-20.3	0.0059	2.0
	Ge	2.1	0.315	2.0	0.0053	

a: coordination number, b: bond distance, c: difference in the origin of photoelectron energy between the reference and the sample, d: Debye-Waller factor, e: residual factor.

Chapter 4 Structural Transformation and Low Pressure Catalysis for Ethyl Acetate Hydrogenation of Rh/GeO_2 submonolayer/SiO_2 Prepared from $Rh_6(CO)_{16}$

Abstract

Catalytic hydrogenation of ethyl acetate was performed on Rh supported GeO_2/SiO_2 (GeO_2 submonolayer supported on SiO_2 surface), where $Rh_6(CO)_{16}$ was used as a precursor for Rh. The activity and selectivity to the ethanol formation was correlated with the structure of Rh determined by EXAFS spectroscopy. The structures of the catalyst were classified to three types depending on the reduction temperatures. They are, the Rh carbonyl cluster, Rh metal, and RhGe alloy. The most active structure for the production of ethanol was Rh metal supported on GeO_2/SiO_2. From the comparison with the catalysis and FT-IR measurement of adsorbed ethyl acetate of Rh supported on bulk-GeO_2, SiO_2 and GeO_2 particles/SiO_2, the direct participation of GeO_2 submonolayer to the reaction was concluded.

4-1 Introduction

monolayer atomic layer oxides have been demonstrated to provide a new kind of supports for metals and also new catalysts [1-6]. Spread of monolayer oxides on e.g. SiO_2 not only increases the surface area of the oxides, but also makes it easy to characterize the topmost surface of oxides relevant to the catalytic phenomena. Metal-support interaction may be well characterized compared to that in metal-bulk oxide systems. As already described in chapter 3, I have prepared Rh/GeO_2 submonolayer/SiO_2 by reaction of $Ge(OMe)_4$ with surface OH groups of SiO_2 followed by calcination at 673 K and by reaction of a Rh dimer complex with isolated OH groups of the obtained GeO_2 submonolayer on SiO_2 followed by reduction with H_2 at 423 to 723 K. It was obtained that Rh and Ge atoms in the $Rh/GeO_2/SiO_2$ behaved in an entirely different manner from

those in Rh/bulk-GeO_2 during the reduction as characterized by EXAFS, XRD and FT-IR. The aim of this study is (1) to prepare Rh/GeO_2/SiO_2 by using $Rh_6(CO)_{16}$ cluster, (2) to examine structural transformations of the Rh/GeO_2/SiO_2 sample during reduction with H_2 at various temperatures, and (3) to apply the new sample to a catalytic reactions.

In this study, I have applied the Rh/GeO_2/SiO_2 catalyst to the several reactions (CO-H_2, NO-CO and hydrogenation of ethyl acetate) to find out the catalytic reaction which makes good use of the characteristic of monolayer support. CO-H_2 and NO-CO reaction are attractive to test because these reactions are known to be greatly influenced by the kind of supports. But, within the tried reactions, the hydrogenation of ethyl acetate to ethanol is most attractive. Ge has the potential to provide hydrogenation reactions that occur on noble metals. For instance, the addition of 3 atom% Ge to Pt particles increases the activity and selectivity in selective hydrogenation of α,β-unsaturated aldehyde to unsaturated alcohol [7]. Catalytic hydrogenation of esters to the corresponding alcohols has been practiced so many years. Copper chromite is a current commercial hydrogenation catalyst and has been applied to the production of diols from diesters or the production of methanol from carbon monoxide and hydrogen by two stage processes [8,9]. In the two steps methanol synthesis, the first step involves CO insertion into the C-O bond of methanol to form methyl formate, and in the following second step a methyl formate is hydrogenated to two methanol molecules. This process is thermodynamically superior to the conventional direct hydrogenation of CO [10-13]. In commercial processes, copper chromite is operated at the pressure as high as 23 MPa and 423-573 K, but this catalyst is not so stable and is deactivated. However thermodynamic calculations show that this reaction can proceed at atmospheric pressure and moderate temperatures lower than 500 K. Recently, several groups have developed new catalysts for the ester hydrogenation. Grey et al. have conducted the hydrogenation reactions in solution by using a soluble anionic ruthenium hydride complex as catalyst [14]. Basset and her co-workers have reported the catalytic property of RhSn alloy catalyst for the acetate hydrogenation at low pressure conditions [15,16]. Wehner et al. used Pd/ZnO which is also

known to be active for methanol synthesis in CO hydrogenation [17]. Deshpande et al. reported a Ru-Sn boride catalyst to be active for the hydrogenation of long chain fatty acids [18]. In addition to the hydrogenation of esters, hydrogenation of acid anhydrides has also been studied; a typical example is the highly regioselective reduction of asymmetrical cyclic carboxylic acid anhydrides to γ-lactonses [19].

I have found the excellent catalytic property of the Rh/GeO_2 submonolayer/SiO_2 sample in the ethyl acetate hydrogenation to ethanol under mild conditions. The activity and selectivity of this catalyst was entirely different from those of Rh/bulk-GeO_2, Rh/SiO_2 and Rh/GeO_2 particles/SiO_2. The new $Rh/GeO_2/SiO_2$ catalyst were characterized by EXAFS, TPD, and FT-IR. The present study demonstrates the advantageous application of inorganic-oxide monolayer as a new class catalyst.

4-2 Experimental

4-2-1 Catalyst Preparation

Preparation of submonolayer GeO_2 supported on SiO_2 was conducted as reported in chapter 2. Loading of Ge in the GeO_2/SiO_2 was fixed at 7.4 wt%. No decolorization of the solution was observed during stirring, which suggests that reaction of $Rh_6(CO)_{16}$ with GeO_2/SiO_2 does not take place significantly at room temperature. Therefore the solvent was removed by evaporation to support $Rh_6(CO)_{16}$. $Rh_6(CO)_{16}$ was also supported on SiO_2 (Aerosil 300) and GeO_2 (hexagonal type; Wako Pure Chem. Co.) in a similar manner to the case of the GeO_2/SiO_2. The loading of Rh in every catalyst was fixed at 2.0 wt%. The samples were reduced for 2 h at given temperatures under 13.3 kPa of hydrogen without calcination of the incipient supported $Rh_6(CO)_{16}$ samples. Hexarhodium hexadecacarbonyl $Rh_6(CO)_{16}$ (purity: 98 %) was purchased from Aldrich Chem. Co. and used without further purification. Chloroform was purified by reflux over 5A Molecular

Sieves and distillation before use as solvent for $Rh_6(CO)_{16}$. A chloroform solution of $Rh_6(CO)_{16}$ was stirred vigorously with the submonolayer GeO_2/SiO_2 under Ar atmosphere at room temperature.

4-2-2 Rh K-edge and Ge K-edge XAFS Measurement

Rh K-edge and Ge K-edge XAFS measurement and analysis were carried out as similar manner reported in section 3-2-2, except for the use of theoretical parameters for the fitting of Rh-C_t (terminal CO in $Rh_6(CO)_{16}$) and Rh-C_b (μ^3-CO in $Rh_6(CO)_{16}$) calculated by FEFF6.0.

4-2-3 Temperature Programmed Desorption

Temperature programmed desorption was carried out under hydrogen (13.3 kPa) in a closed circulating system. The temperature was raised from room temperature up to 773 K at a heating rate of 4 K min^{-1}. The desorbed products were analyzed with a gas chromatograph (Shimadzu GC-8A, Column: Molecular Sieve 5A).

4-2-4 CO-H_2 and NO-CO Reaction

CO-H_2 and NO-CO reactions were conducted with a closed circulating system (dead volume: 210 cm^3). Equimolar mixture of CO and H_2 (total pressure: 26.6 kPa) was reacted with the pre-treated catalyst at 523 K. The products except for methane was collected with liq.N_2 trap and analyzed by Gas chromatograph equipped with DOS and Molecular Sieves 5A columns. NO-CO reaction was conducted with mixture of NO (4.2 kPa) and CO (4.2 kPa) at 423 K. The products were analyzed by Gas chromatograph. The used column are Molecular Sieves 5A (methane) and Unibeads C (the other products).

4-2-5 Catalytic Hydrogenation of Ethyl Acetate

Catalytic hydrogenation reactions of ethyl acetate over 0.1 g of catalyst were conducted in a closed circulating system equipped with a gas chromatograph. Reduction of the catalyst was conducted at hydrogen of 13.3 kPa and given temperatures (423-723 K) for 2 h *in-situ* before use as catalysts, followed by evacuation at the same temperatures. The ethyl acetate was purified by repeated freeze-thaw cycles. The catalytic reactions were conducted under a mixture of 6.6 kPa of hydrogen and 1.3 kPa of ethyl acetate. The reaction temperature was fixed at 473 K. The products were analyzed by a gas chromatograph using a DOS column for analysis of ethanol and acetaldehyde and a VZ-10 column for analysis of methane and ethane.

4-2-6 Measurement of FT-IR spectra

FT-IR spectra were measured on a JASCO FT-IR 230 spectrometer with 2 cm^{-1} resolution. The samples were pressed to their wafers with 20 mm in diameter and placed in a holder in an *in-situ* IR cell combined in a closed circulating system. The samples, $Rh/GeO_2/SiO_2$, GeO_2/SiO_2, GeO_2, and SiO_2 were exposed to 6.6 kPa of ethyl acetate at various temperatures ranging 373-473 K, followed by evacuation.

4-3 Results and Discussion

4-3-1 Structural Change of $Rh_6(CO)_{16}$ during Reduction Treatments Determined by XAFS Spectroscopy

Figure 1 shows Rh K-edge EXAFS spectra $Rh_6(CO)_{16}$ cluster, the incipient supported $Rh_6(CO)_{16}$ on GeO_2/SiO_2, and the $Rh/GeO_2/SiO_2$ samples reduced with H_2 at 423-723 K. The

incipient supported $Rh_6(CO)_{16}$ shows the similar EXAFS data as those for $Rh_6(CO)_{16}$ cluster itself (Figures 1 and 2) and the curve fitting analysis in figure 3 and table 1 reveals that the framework of the Rh carbonyl cluster is retained on the GeO_2/SiO_2 surface. The feature did not change by reduction at 343 K. It was suggested that $Rh_6(CO)_{16}$ preferentially interacts with the GeO_2 submonolayer (1/5 monolayer) rather than the exposed SiO_2 surface as proved by FT-IR as shown in figure 4. Isolated Ge-OH peak at 3676 cm^{-1} decreased and shifted to the lower wavenumber side due to hydrogen bonding with the cluster, while Si-OH peaks at 3745 cm^{-1} did not change significantly upon supporting $Rh_6(CO)_{16}$.

The EXAFS feature changed by reduction with H_2 at 423 K (Figure 1 (c)). The single peak around 0.25 nm (phase shift uncorrected) observed in the Fourier transform shifted toward the shorter length as shown figure 2 (c). The Rh-Rh bond length was determined by curve fitting to be 0.266 nm (Table 1), which is close to the Rh-Rh bond distance of Rh metal (0.269 nm). Besides the decrease in the Rh-Rh bond distance from 0.277 nm to 0.266 nm, the Rh-C_t and Rh-C_b bonding disappeared with $Rh/GeO_2/SiO_2$ reduced at 423 K as shown in table 1.

Desorption of CO from the incipient supported $Rh_6(CO)_{16}$ was examined by TPD under hydrogen as shown in figure 5. A small desorption peak at 390 K may correspond to the change in the EXAFS spectra. However, two major desorption peaks were observed at 550-650 K in figure 5 and the amount of CO desorbed around 390 K was only 8 % of the total amount of desorbed CO in TPD. The desorption feature may be incompatible with the EXAFS results in table 1. The EXAFS data for the samples reduced at the higher temperatures than 423 K demonstrate destruction of the cluster framework accompanied with decarbonylation of the supported $Rh_6(CO)_{16}$ and aggregation of the Rh_6 cluster to small Rh particles with the coordination number of 7.4-7.5 for Rh-Rh bond. The decarbonylation process is not a simple desorption process because the majority of the carbonyls did not desorb below 500 K. I propose that the Rh_6 cluster on GeO_2/SiO_2 is not destructed after full decarbonylation, but transformed to larger clusters by partial decarbonylation. TPD was also carried out $Rh_6(CO)_{16}$ supported on the SiO_2 for

comparison. A small desorption at 390 K was also observed, suggesting desorption at 390 K in $Rh/GeO_2/SiO_2$ is not related with the GeO_2 submonolayer. On the other hand, a major desorption was observed at 590 K on Rh/SiO_2 which differs from $Rh/GeO_2/SiO_2$ where double peaks were observed. It is supposed that in addition to the simple decarbonylation from Rh metal particles at 550 K, the RhGe alloy formation should be closely related with the second desorption peak of CO at 620 K on GeO_2/SiO_2. The mechanism of the partial decarbonylation-induced structural transformation is not clear at present and the structure and shape of the produced Rh clusters/particles can not be characterized by EXAFS and FT-IR.

The peak intensity in the Fourier transform decreased by reduction of the sample at 623 K as shown in figure 2 (e). The curve fitting analysis of the $k^3\chi(k)$ spectrum of this sample using Rh-Rh single wave never reproduced the observed data and good fitting was obtained by the addition of Rh-Ge wave as shown in figure 3 (e). The Rh-Rh and Rh-Ge distances were determined to be 0.268 nm and 0.241 nm, respectively as shown in table 1. The peak in the Fourier transforms for $Rh/GeO_2/SiO_2$ reduced at 723 K (Figure 2 (f)) shifted toward shorter distance. As for this sample, the curve fitting based on Rh-Ge one-wave gave the best result (Figure 3 (f) and Table 1). The fitting was not improved by two-waves (Rh-Ge and Rh-Rh) analysis. These results suggest the formation of RhGe alloy particles on GeO_2/SiO_2. The determined Rh-Ge bond distance was at 0.244 nm which is essentially the same as 0.241 nm for Rh-Ge in the sample reduced at 623 K, while the coordination number of Rh-Ge bond increased from 0.9 to 3.5 as the reduction temperature increased from 623 K to 723 K, respectively. The change in the bonding modes of Rh-Rh and Rh-Ge indicates a gradual RhGe alloy formation of the metallic Rh particles with the reduced GeO_2 submonolayers on SiO_2. These results are different from those on RhGe alloys prepared by the deposition of Rh dimer complex $[Rh(C_5Me_5)Me]_2(\mu\text{-}CH_2)_2$ and successive calcination and reduction treatment, where Rh-Rh bonding was always observed. The reason may be referred to the difference of Rh particle size. The $Rh_6(CO)_{16}$-derived catalyst was prepared by reduction with H_2 without oxidation before the reduction, while the Rh dimer-derived sample was

prepared by reduction after oxidation of the incipient supported species.

Figure 6 shows the XANES spectra of $Rh_6(CO)_{16}$, the incipient supported $Rh_6(CO)_{16}$ and the reduced $Rh/GeO_2/SiO_2$. The peaks at 10 and 35 eV above the threshold energy attenuated with rise of reduction temperature, which is evident in the spectrum of the sample reduced at 723 K. The first peak is related to the electronic transitions from the core level (1s) to the empty states above the Fermi level and the second peak is due to the multiple scattering processes of the outgoing electron [22]. The calculation of multiple scattering in different cluster sizes shows the increase of the second peak with an increase in particle size [23]. As for the observed attenuation of the peak intensity may be due to the formation of RhGe alloy particles where Rh atoms are replaced by Ge atoms and the back scattering of photoelectrons by Ge atoms is less that that by Rh atoms.

Figure 7 shows the Ge K-edge EXAFS spectra of $Rh/GeO_2/SiO_2$ reduced at 723 K. A small peak appears in the EXAFS Fourier transform with the reduction treatment. The curve fitting analysis of the extracted spectra with Ge-Rh single wave gives reasonable result. The fitted Ge-Rh distance is 0.243 nm which agrees well with the measurement from Rh K-edge within experimental error. This result supports the RhGe alloy formation on GeO_2/SiO_2 reduced at high temperature. The influence of RhGe alloy formation is also observed in the XANES spectrum. Small shoulder appears in the spectrum reduced at 723 K which become clearer by subtraction of the spectrum with that of GeO_2/SiO_2 as shown in figure 7 (c). The position corresponds to the metal Ge.

As consequence, $Rh_6(CO)_{16}$ is supported on GeO_2/SiO_2 with retention of the cluster framework below 343 K, the supported $Rh_6(CO)_{16}$ clusters are converted to Rh metallic particles by reduction with H_2 at 423-523 K, and RhGe alloy particles are produced on GeO_2/SiO_2 by reduction above 623 K.

4-3-2 CO-H_2 and NO-CO Reaction

Figure 8 shows the total activity and selectivity toward oxygenates formation in CO-H_2 reaction plotted against the reduction temperature. The reduction temperature could be correlated with the state of Rh particles as stated in the previous section. The total activity of the sample reduced at 723 K decreased to 1/25 of that reduced at 523 K. The RhGe alloy formation with rise of reduction temperature may be reflected to this result. On the other hand, the selectivity to oxygenates increased with reduction temperature up to 90%. The reason of this activity change may come from the alloy formation which cause the suppression of adsorption of hydrogen on Rh surface which accelerated the methanation reaction with CO, where the role of Ge may be the dilution and the scission of surface Rh ensemble.

Figure 9 shows the correlation between activity or selectivity of NO-CO reaction and reduction temperature during pre-treatment step. CO_2, N_2O and N_2 were detected as the reaction products. The activity of every product gradually increased with rise of reduction temperature, reached the maximum at 623 K, and then decreased above this temperature (a). The selectivity to N_2 and N_2O formation derived by the division with CO_2 activity was shown in figure 9 (b). The selectivity to N_2O formation was constant within the whole temperature of reduction, but the selectivity to N_2 continued to increase from 17 % (reduced at 423 K) to 59 % (reduced at 723 K). This result clearly shows the enhancement of Ge to the N_2 formation, probably which is different reason of the promotion of N_2O and CO_2 because its profile differs from the others. For comparison, the reaction was carried out on Rh/SiO_2 reduced at 623 K (the temperature where the most active phase was obtained on Rh/GeO_2/SiO_2) and the results were also plotted in figure 7. The activity and selectivity were close to the Rh/GeO_2/SiO_2 catalyst reduced at 423 K, where alloy formation was not recognized. This result shows that the alloy formation of Ge enhances the activity and increases the selectivity towards N_2 formation, which differs from the result on CO-H_2 reaction where activity was greatly suppressed with rise of reduction temperature. EXAFS spectra were measured on NO exposed RhGe alloy to obtain the information about the active structure of catalyst under the NO-CO reaction. Exposure of CO did not affect the EXAFS results. Figure 10

shows the Fourier transforms and $k^3\chi(k)$ EXAFS spectra of $Rh/GeO_2/SiO_2$ reduced at 723 K, followed by exposure to 2.7 kPa of NO and evacuation as well as its curve fitting result with 3-waves (Rh-Rh, Rh-Ge and Rh-O). The fitted parameters are listed in table 3. The curve fitting results shows the increase of Rh-Rh and decrease of Rh-Ge wave, compared with before introduction of NO. At the same time, Rh-O bond appears, but the Rh-Rh bond, the distance of which corresponds to Rh oxide, was not found. Therefore the oxidation of metal particles may be restricted on the surface of metal particles. This result suggests that the partial oxidation of alloy surface with NO takes place under reaction condition. Though the active phase is not identical with the initial alloy under NO-CO reaction condition, the participation of Ge oxide or Ge metal rest on the alloy surface cannot be excluded, because its existence was confirmed in the EXAFS result.

4-3-3 Catalytic Hydrogenation of Ethyl Acetate to Ethanol on Rh/GeO_2 submonolayer/SiO_2

Figure 11 shows the activity and selectivity of the catalytic hydrogenation of ethyl acetate on $Rh/GeO_2/SiO_2$ as a function of the reduction temperature. For comparison, the results on Rh/GeO_2 and Rh/SiO_2 are shown in figure 11. Further, $Rh_6(CO)_{16}$ supported on three-dimensional GeO_2 particles on SiO_2 (denoted as $Rh/c\text{-}GeO_2/SiO_2$) was also employed as catalyst after reduction with H_2 at various temperatures (Figure 11). Ideally, the reaction proceeds by eq.(1).

$$CH_3COOC_2H_5 + 2\,H_2 \rightarrow 2\,C_2H_5OH \qquad (1)$$

The by-products in the parallel reactions are acetaldehyde or hydrogenolysis products such as methane and ethane. The selectivity to ethanol (S_{C2H5OH}) is defined as carbon-base selectivity which is given by eq.2.

$$S_{C2H5OH} = \frac{r_{C2H5OH}}{r_{C2H5OH} + r_{CH3CHO} + 1/2\,r_{CH4} + r_{C2H6}} \qquad (2)$$

rC_2H_5OH, rCH_3CHO, rCH_4 and rC_2H_6 are the initial rates for the formation of C_2H_5OH, CH_3CHO, CH_4 and C_2H_6 in mol min^{-1} g-cat^{-1}.

$Rh/GeO_2/SiO_2$ showed the highest selectivity for ethanol formation when the catalyst was reduced at 423 K. The $Rh/GeO_2/SiO_2$ catalysts reduced at 423-523 K were not active for ethanol formation. In these catalysts, the Rh is located as metallic particles on GeO_2/SiO_2 as characterized by EXAFS. The activity and selectivity for ethanol formation successively decreased with rise of reduction temperature as shown in figure 11. It is to be noted that the ethanol formation proceeded with high selectivity at such a low hydrogen pressure as 13.3 kPa, which is a considerably moderate condition for this kind of catalytic reactions compared with the conditions operated on copper chromite or other catalysts thus far studied. Acetaldehyde as a by-product was produced on $Rh/GeO_2/SiO_2$ reduced at 623 K and the formation was enhanced by increasing reduction temperature. The temperature of the beginning of acetaldehyde formation agreed with the temperature of the beginning of the RhGe alloy formation.

The catalytic reactions were compared with those on Rh/bulk-GeO_2 and Rh/SiO_2 in figure 11. On Rh/GeO_2 very small amounts of acetaldehyde were detected over the whole temperature range. Thus it is ascertained that Rh/GeO_2 is inactive for the ethyl acetate hydrogenation. The reason of the inactivity of Rh/GeO_2 is attributed to the dissolution of Rh into metallic Ge generated by the reduction of GeO_2 surface to form RhGe alloy particles which are suggested to be located in the GeO_2 bulk and below the surface of GeO_2 support. No adsorption of CO and H_2 was observed on the reduced Rh/GeO_2 samples. The TPD spectrum in figure 5 (c) showed a CO desorption peak at 400 K, suggesting the carbonyls of $Rh_6(CO)_{16}$ on GeO_2 desorb before the RhGe alloy formation.

On Rh/SiO_2 ethane and methane were major products in the whole temperature range of reduction and no ethanol and acetaldehyde was produced as shown in figure 11 (c). The total activity decreased with rise of reduction temperature.

To examine the property of Rh particles on the GeO_2 submonolayer supported on SiO_2 surface, I also compared the catalysis of Rh/GeO_2 submonolayer/SiO_2 with that of Rh/c-GeO_2/SiO_2, where

c-GeO_2 represents crystalline GeO_2 particles dispersed on SiO_2. The c-GeO_2/SiO_2 is prepared by exposing the GeO_2 submonolayer/SiO_2 to 1.3 kPa of H_2O for 1 h at room temperature. In the present study the Rh/GeO_2/SiO_2 reduced at 523 K was exposed to water vapor in the similar condition. The effect of the exposure of H_2O vapor the Rh metal was examined by EXAFS, but the spectral feature did not change in both Fourier transform and $k^3\chi(k)$ oscillation spectra after exposure of H_2O vapor as shown in figure 12. The Rh-Rh coordination number determined by the curve fitting analysis for the Rh/c-GeO_2/SiO_2 was almost the same as that for the original 523 K-reduced Rh/GeO_2/SiO_2 in table 1. This means that the Rh metal does not suffer any effect by exposure to H_2O vapor. The activity and selectivity of the Rh/c-GeO_2/SiO_2 for the ethyl acetate hydrogenation were plotted as a function of reduction temperature in figure 11 (d). A small change in the activity for the formation of methane and acetaldehyde was observed by transformation of the GeO_2 monolayer to the crystalline three-dimensional GeO_2 particles. More drastic effect of the morphological change of GeO_2 on the catalysis was observed with the formation of ethanol which was suppressed drastically as shown in figure 11 (d). Thus, the formation of methane and acetaldehyde is insensitive to the morphology of GeO_2 on SiO_2, while the ethanol is produced preferentially in the presence of the GeO_2 monolayers rather than the GeO_2 particles.

From these results, it is concluded that the most active phase for the ethanol formation from ethyl acetate is the Rh metallic particles deposited on the GeO_2 submonolayer, where the participation of the GeO_2 submonolayer in the catalytic hydroformylation reaction is expected. The Rh particles themselves do not catalyze the selective ethanol formation because the Rh/SiO_2 catalysts were inactive for the ethyl acetate hydrogenation (Figure 11 (c)). The RhGe alloy particles produce acetaldehyde rather than ethanol.

To explore the role of the GeO_2 monolayer on SiO_2 in the ethanol formation, FT-IR spectra of adsorbed ethyl acetate on the GeO_2/SiO_2 and SiO_2 were measured. Figure 13 (a) shows the FT-IR spectra of GeO_2/SiO_2 after exposure of 1.3 kPa of ethyl acetate at 373 K, 423 K and 473 K, followed by the evacuation of the gas phase at the same temperatures. The peaks are observed at

2980, 2934, 2901, 1728, 1391 and 1376 cm^{-1}. The bands at 2980, 2934 and 2901 cm^{-1} and 1391 and 1376 cm^{-1} are assigned to the CH-stretching and CH-bending vibrations, respectively. The band at 1728 cm^{-1}, it is assignable to the C=O stretching mode of unidentate acetate because it agrees with the spectrum of unidentate germyl acetate ester obtained by the dissociative adsorption of acetic acid on GeO_2 [24]. Thus the observed spectra indicate the dissociative adsorption of ethyl acetate to form unidentate acetate on GeO_2/SiO_2. The peak intensity of the adsorbed species became more intense with an increase of adsorption temperature. The similar spectra were observed under the catalytic reaction conditions on $Rh/GeO_2/SiO_2$ at 473 K, and no other species was detected. The peak intensity of the adsorbed species on the GeO_2/SiO_2 without Rh remained unchanged under hydrogen at 473 K, whereas it rapidly reduced on $Rh/GeO_2/SiO_2$ by introducing H_2 to the system. Similar spectra were observed on bulk-GeO_2, which implies that the adsorption mode is inherent in GeO_2. Ethyl acetate dissociates to bidentate acetate and ethanol on TiO_2 [25,26], where the dissociation of ethyl acetate occurs on OH groups at TiO_2 surface which possess Brönsted acidity. Considering the lack of surface acidity on GeO_2/SiO_2, it is plausible that the dissociative adsorption proceeds on Ge-O-Ge sites. Indeed, it has been demonstrated that the dissociative adsorption of acetic acid on GeO_2 was accompanied with scission of Ge-O-Ge bond to form germyl ester and isolated OH groups [24]. Similar explanation has been applied to the chemisorption of methanol on GeO_2 [27]. Ethyl acetate may also adsorb on the Ge-O-Ge sites of GeO_2 submonolayer to form unidentate acetate and ethoxy groups as illustrated in figure 14. On the other hand, ethyl acetate did not adsorb on SiO_2 as shown in figure 13 (b) which coincides with the literature [28].

From these results on the catalytic properties of $Rh/GeO_2/SiO_2$, $Rh/c\text{-}GeO_2/SiO_2$, Rh/GeO_2 and Rh/SiO_2 and the characterization of the catalysts by EXAFS and FT-IR, a possible reaction mechanism of the hydrogenation is stated as follows. Ethyl acetate dissociatively adsorbs to form unidentate acetate and ethoxy on the GeO_2 submonolayers, while hydrogen adsorbs on the Rh metallic particles supported on the GeO_2 overlayers to supply adsorbed hydrogen atoms. The

hydrogen atoms are spiltover from the Rh particles to the GeO_2 submonolayers on which the hydrogenation of the adsorbed species proceeds to produce ethanol as illustrated in figure 14.

4-4 Conclusions

(1) $Rh/GeO_2/SiO_2$ catalysts were prepared by supporting $Rh_6(CO)_{16}$ on GeO_2 submonolayer attached on SiO_2 surface, followed by reduction with H_2 at 423-723 K.

(2) The $Rh/GeO_2/SiO_2$ catalysts reduced at 423-723 K showed high activity and selectivity for the ethyl acetate hydrogenation to produce ethanol. On the contrary, Rh/GeO_2 and Rh/SiO_2 were inactive for the ethanol formation from ethyl acetate.

(3) The GeO_2 submonolayer was much more effective as support for Rh metallic particles than three-dimensional GeO_2 particles dispersed on SiO_2.

(4) Structural change of $Rh_6(CO)_{16}$ on the GeO_2/SiO_2 was followed by EXAFS , TPD and FT-IR. In the samples reduced below 343 K the $Rh_6(CO)_{16}$ cluster framework was retained. By reduction at 423-523 K the carbonoyls partially desorbed and metallic Rh particles were formed. By further reduction above 673 K RhGe alloy particles were formed.

(5) Decrease of total activity as well as increase of the oxygenates selectivity in the $CO-H_2$ reaction and the increase of total activity and selectivity to N_2 in the NO-CO reaction was observed with rise of the reduction temperature.

(6) Ethyl acetate dissociatively adsorbs to form acetate and ethoxy on the GeO_2 submonolayer, while hydrogen adsorbs on Rh metallic particles.

(7) The spillover hydrogen through the Rh surface reacts with the adsorbed species on the GeO_2 submonolayer on SiO_2.

(8) This study demonstrates the significance of the use of monolayer sample as a support for metal in the catalytic hydrogenation of ethyl acetate and exemplifies the advantageous applications of inorganic oxide monolayer.

4-5 References

[1] Y.-C. Xie and Y.-Q. Tang, *Adv. Catal.*, **37** (1988) 1.

[2] M. Niwa, *Shokubai*, **34** (1992) 221.

[3] K. Asakura, M. Aoki, M.and Y. Iwasawa, *Catal. Lett.* **1** (1988) 395.

[4] K. Asakura and Y. Iwasawa, *Chem. Lett.* (1986) 859.

[5] M. Shirai, K. Asakura and Y. Iwasawa, *J. Phys. Chem.*, **95** (1991) 9999.

[6] K. Asakura and Y. Iwasawa, *Chem. Lett.* (1988) 633.

[7] S. Galvagno, Z. Poltarzewski, A. Donato, G. Neri and R. Pietropaolo, *J. Chem. Soc., Chem. Commun.*, (1986) 1729.

[8] W. L. Marsden, M. S. Wainwright and J. B. Friedrich, *Ind. Eng. Chem. Prod. Res. Dev.*, **19** (1980) 551.

[9] M. Shimizu and S. Takeoka, *Chem. Soc. Japan*, **6** (1981) 912.

[10] J. W. Evans, M. S. Wainwright, N. W. Cant and D. L. Trimn, *J. Catal.*, **88** (1984) 203.

[11] J. W. Evans, P. S. Casey, M. S. Wainwright, D. L. Trimn and N. W. Cant, *Appl. Catal.*, **7** (1983) 31.

[12] J. W. Evans, N. W. Cant, D. L. Trimn and M. S. Wainwright, *Appl. Catal.*, **6** (1983) 355.

[13] H.Ono, *Shokubai*, **39** (1997) 50.

[14] R. A. Grey, G. P. Pez, A. Wallo and J. Corsi, *J. Chem. Soc., Chem. Commun.*, (1980) 783.

[15] A. E. Mansour, J. P. Candy, J. P. Bournonvivlle, O. A. Ferretti and J.-M. Basset, *Angew. Chem. Int. Ed. Engl.*, **28** (1989) 347.

[16] J. P. Candy, O. A. Ferretti, G. Mabilon, J. P. Bournonville, A. E. Mansour, J.-M. Basset and G. Martino, *J. Catal.*, **112** (1988) 210.

[17] P. S. Wehner, G. C. Testin and B. L. Gustafson, *J. Catal.*, **88** (1984) 246.

[18] V. M. Deshpande, K. Ramnarayan and C. S. Narasimhan, *J. Catal.*, **121** (1990) 174.

[19] S. Iijima and M. Ichikawa, *J. Catal.*, **94** (1985) 313.

[20] Y. Iwasawa, (eds.) *X-ray Absorption Fine Structure for Catalysts and Surfaces*; World Scientific: Singapore, 1996.

[21] W. H. McMaster, N. Kerr Del Grande, N. Mallet and J. H. Hubell, *Comparison of X-ray Cross Section*; National Technical Information Service: Springfield, 1969.

[22] J. C. J. Bart, *Adv. Catal.*, **34** (2986) 203.

[23] G. N. Grevans, P. J. Durham, F. Diakun and P. Quinn, *Nature* (London) , **294** (1981) 139.

[24] J. C. McManus and M. J. D. Low, *J. Phys. Chem.* **72** (1968) 2378.

[25] A. D. Buckland, J. Graham, R. Rudham and C. H. Rochester, *J. Chem. Soc., Faraday Trans.*, **77** (1981) 2845.

[26] J. Graham, C. H. Rochester and R. Rudham, *J. Chem. Soc., FaradayTrans.*, **77** (1981) 1973.

[27] J. C. McManus, K. Matsushita and M. J. D. Low, *Can. J. Chem.*, **47** (1969) 1077.

[28] N. W. Stephen, N. W. Cross and C. H. Rochester, *J. Chem. Soc., FaradayTrans.1*, **75** (1979) 2865.

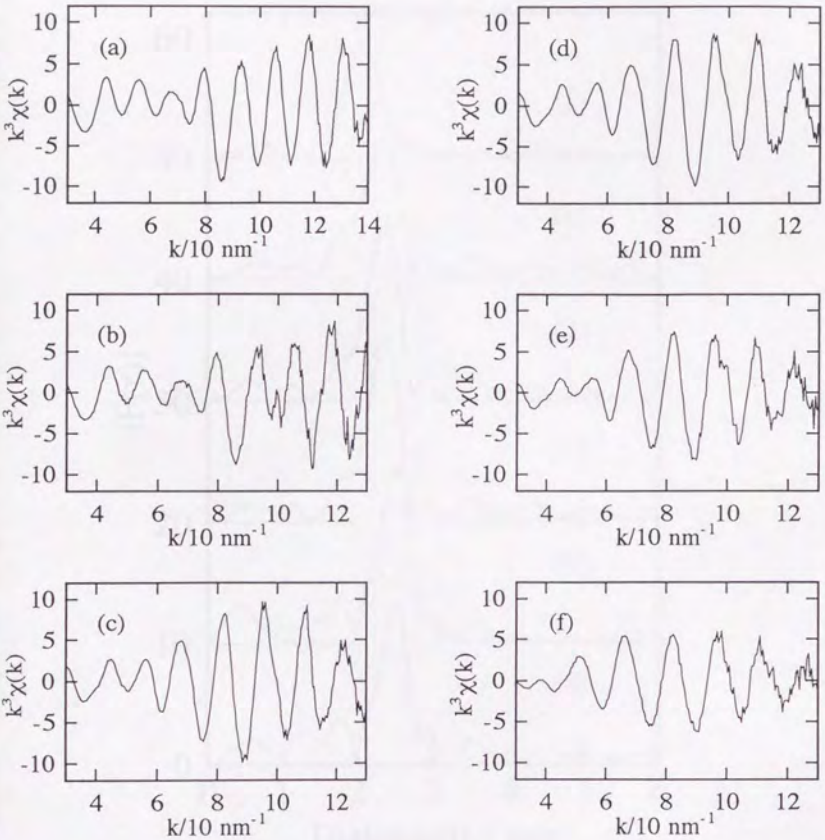

Figure 1. Rh K-edge EXAFS $k^3\chi(k)$ oscillations for $Rh_6(CO)_{16}$ (a) and $Rh/GeO_2/SiO_2$ (b-f); (b) incipient supported $Rh_6(CO)_{16}$, (c) reduced at 423 K, (d) reduced at 523 K, (e) reduced at 623 K, and (f) reduced at 723 K.

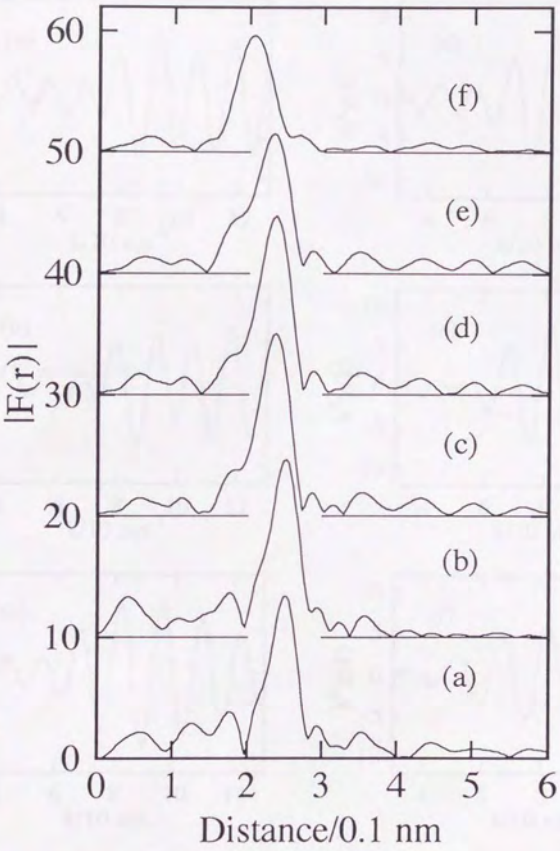

Figure 2. Rh K-edge EXAFS Fourier transforms for $Rh_6(CO)_{16}$ (a) and $Rh/GeO_2/SiO_2$ (b-f); a-f: corresponding to figure 1.

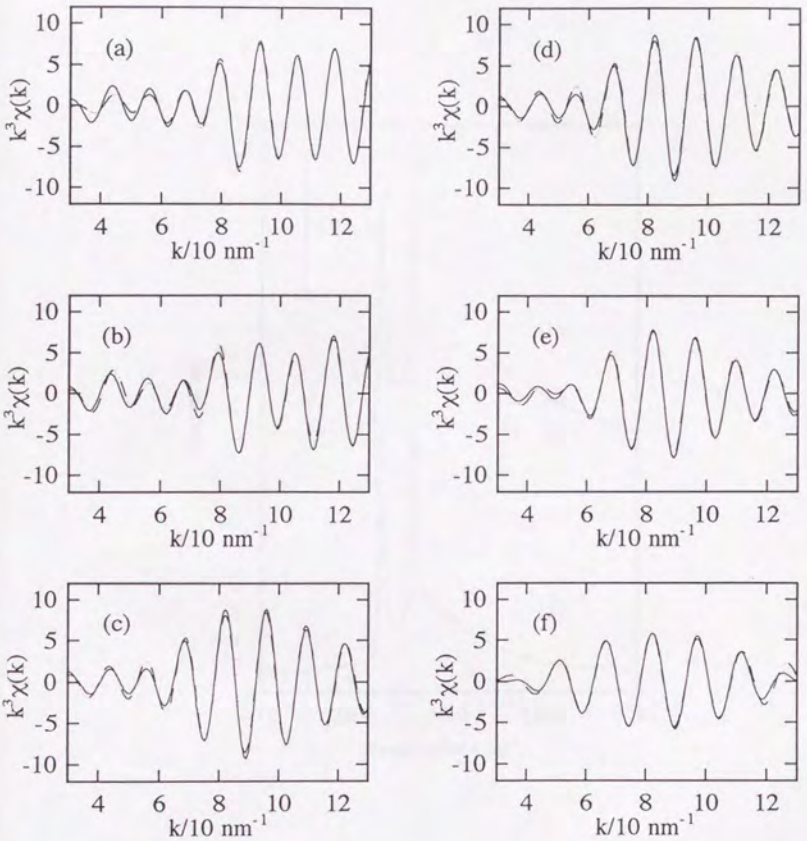

Figure 3. Curve fitting analysis for Rh K-edge EXAFS spectra for $Rh_6(CO)_{16}$ (a) and $Rh/GeO_2/SiO_2$ (b-f); a-f: same as in Figure 1; (a,b): analysis with Rh-C_t, Rh-C_b and Rh-Rh three waves, (c, d): analysis with Rh-Rh single wave, (e): analysis with Rh-Rh and Rh-Ge two waves, (f) analysis with Rh-Ge single wave.

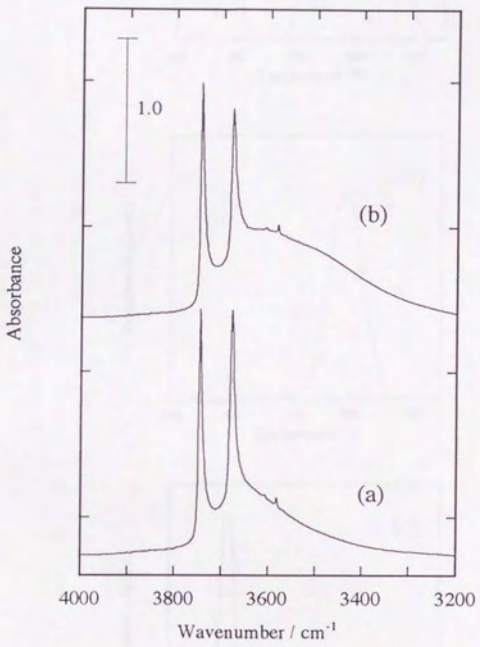

Figure 4. FT-IR spectra of (a) GeO_2/SiO_2, (b) after attachment of $Rh_6(CO)_{16}$ at room temperature.

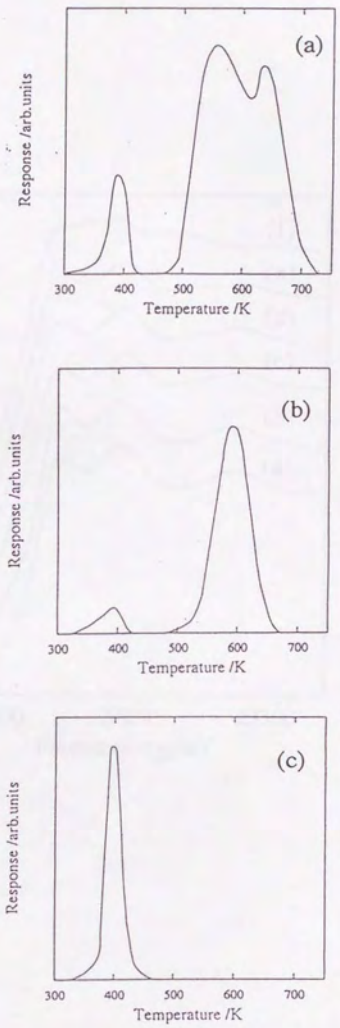

Figure 5. Temperature programmed desorption of CO under 13.3 kPa of H_2; (a) $Rh/GeO_2/SiO_2$, (b) Rh/SiO_2, (c) Rh/GeO_2; heating rate: 4 K min^{-1}.

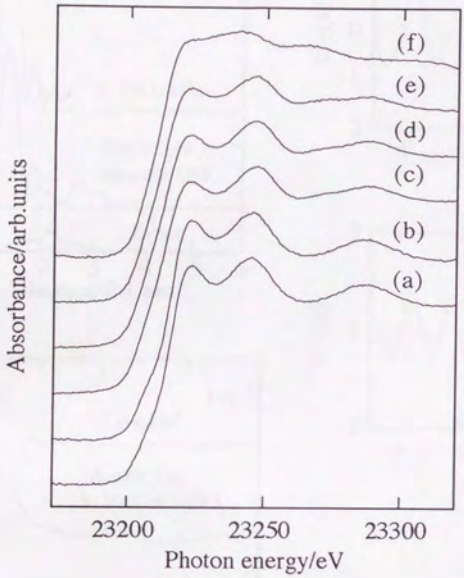

Figure 6. Rh K-edge XANES spectra of (a) $Rh_6(CO)_{16}$ and (b-f) $Rh/GeO_2/SiO_2$; (b) incipient supported species, (c) reduced at 423 K, (d) reduced at 523 K, (e) reduced at 623 K, and (f) reduced at 723 K.

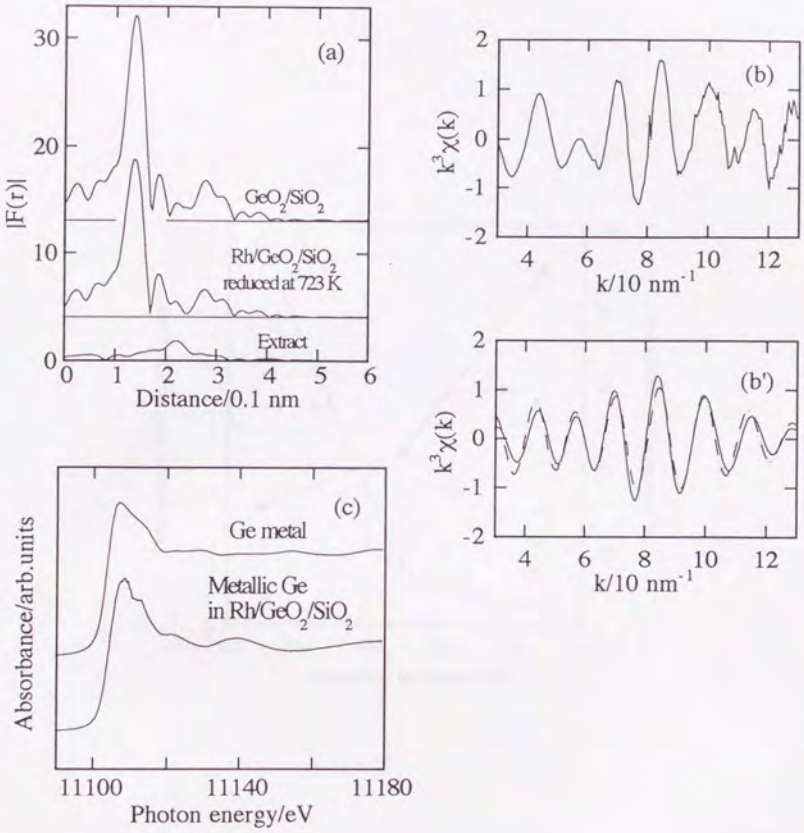

Figure 7. Ge K-edge XAFS spectra: (a) EXAFS Fourier transforms of GeO_2, $Rh/GeO_2/SiO_2$ reduced at 723 K and the spectrum subtracted form the Ge-O oscillation; (b) $k^3\chi(k)$ spectrum and (b') curve fitting analysis with Ge-Rh single wave of the difference spectra of $Rh/GeO_2/SiO_2$ reduced at 723 K after subtraction of the Ge-O oscillation in $Rh/GeO_2/SiO_2$; (c) XANES spectra of $Rh/GeO_2/SiO_2$ reduced at 723 K after subtraction of GeO_2/SiO_2 spectrum and Ge metal powder.

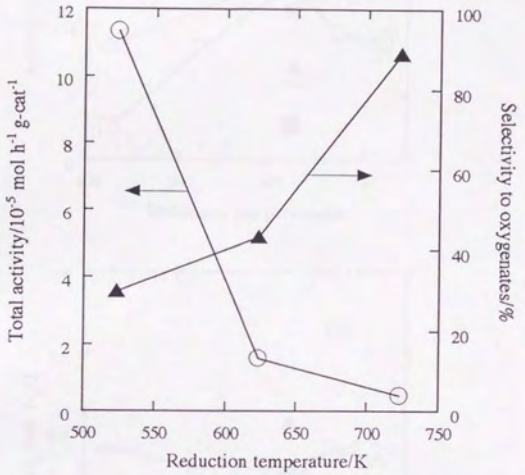

Figure 8. Activity and selectivity to oxygenates of CO-H_2 reaction on Rh/GeO_2/SiO_2 plotted as a function of reduction temperature; reaction temperature: 523 K, pressure: CO 13.3 kPa, H_2 13.3 kPa.

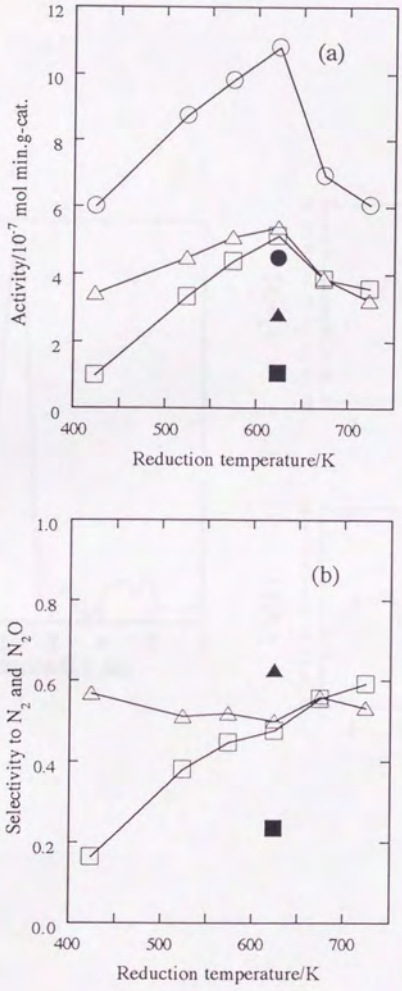

Figure 9. Activity (a) and selectivity (b) of NO-CO reaction on $Rh/GeO_2/SiO_2$ and Rh/SiO_2 plotted as a function of reduction temperature; ○: CO_2, △: N_2O, □: N_2 on $Rh/GeO_2/SiO_2$; ●: CO_2, ▲: N_2O, ■: N_2 on Rh/SiO_2; Selectivity to N_2 and N_2O were defined as r_{N_2}/r_{CO_2} and r_{N_2O}/r_{CO_2}, respectively.

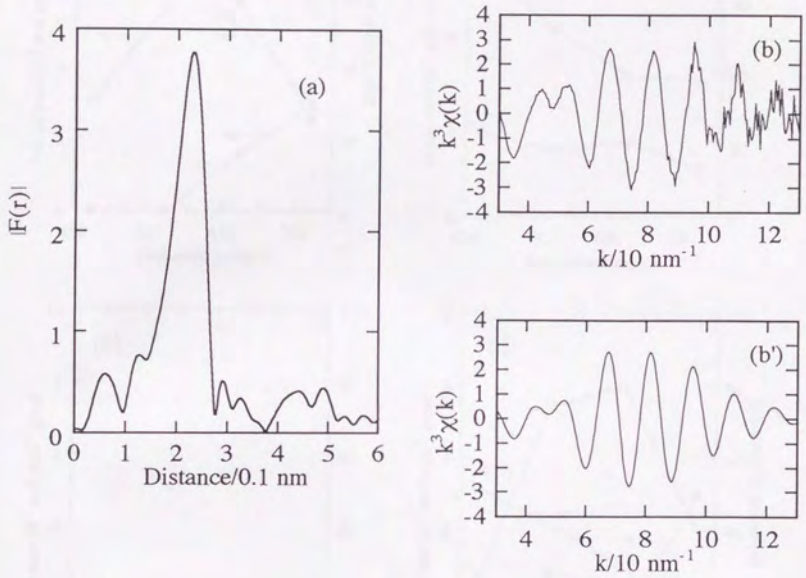

Figure 10. EXAFS spectra of $Rh/GeO_2/SiO_2$ reduced at 723 K and exposed to 2.7 kPa NO, followed by evacuation at room temperature; (a) Fourier transform, (b) $k^3\chi(k)$, and (b') curve fitting analysis with Rh-Rh, Rh-Ge and Rh-O three waves; (solid line: observed, dotted line: calculated).

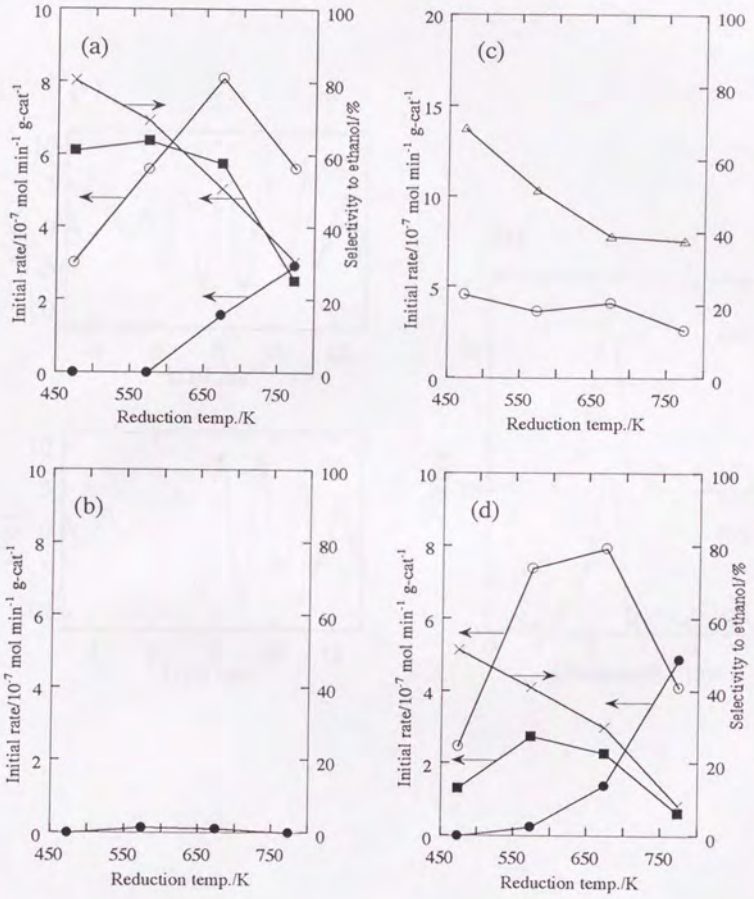

Figure 11. Catalytic activity and selectivity (ethanol formation) of (a) $Rh/GeO_2/SiO_2$, (b) Rh/GeO_2, (c) Rh/SiO_2, and (d) $Rh/c\text{-}GeO_2/SiO_2$ in catalytic hydrogenation of ethyl acetate plotted as a function of reduction temperature; reaction temperature: 473 K, hydrogen pressure: 6.6 kPa, ethyl acetate pressure: 1.3 kPa; ■: ethanol, ●: acetaldehyde, ○: methane, △: ethane and ×: selectivity to ethanol.

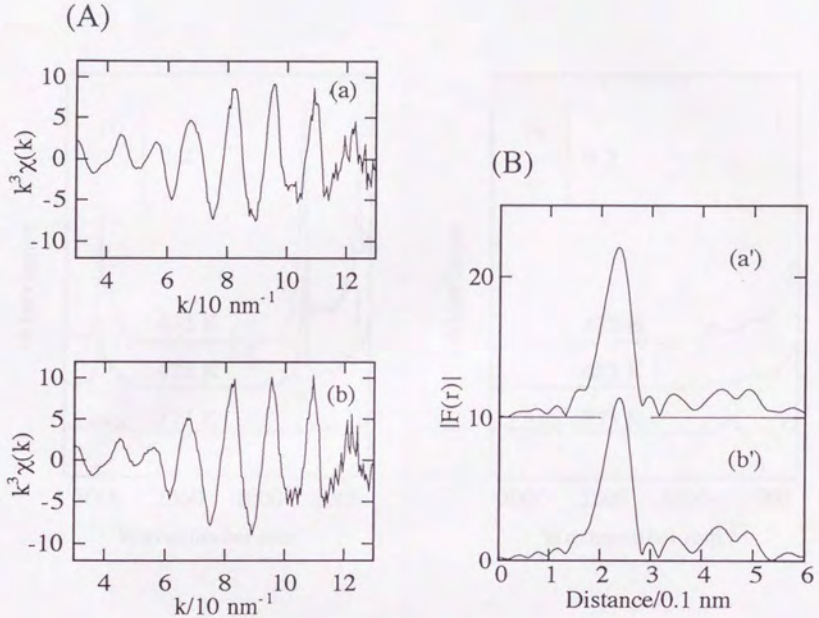

Figure 12. Rh K-edge EXAFS oscillations (A), their Fourier transforms (B) for $Rh/GeO_2/SiO_2$; (a, a') reduced at 4233 K; (b, b') reduced at 423 K, followed by exposed to 1.3 kPa H_2O vapor at room temperature.

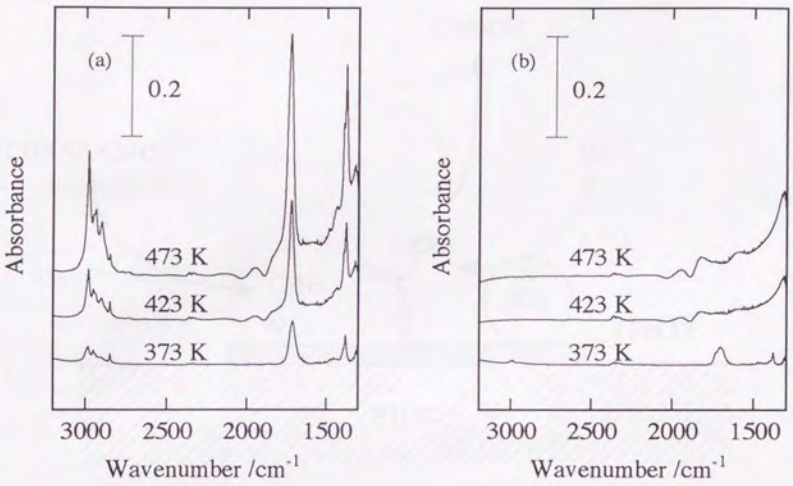

Figure 13. FT-IR spectra of ethyl acetate adsorbed on (a) GeO_2/SiO_2 and (b)SiO_2; the spectra were measured after exposure of 1.3 kPa of ethyl acetate at 373 K, 423 K and 473 K, followed by evacuation of the gas phase at the same temperatures.

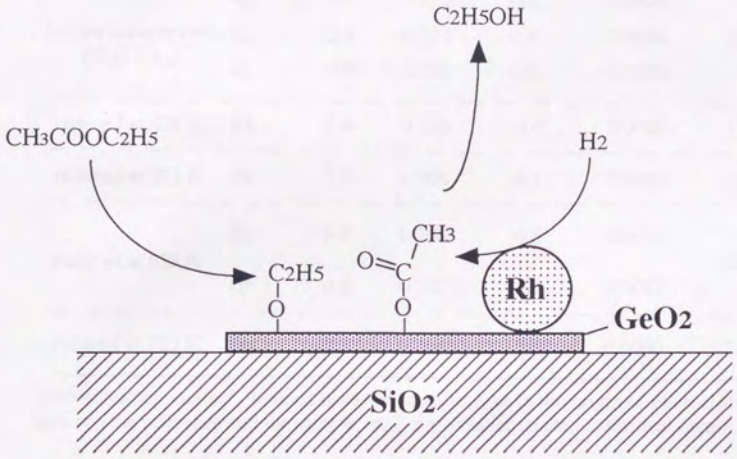

Figure 14. Schematic picture of the ethyl acetate hydrogenation on $Rh/GeO_2/SiO_2$ reduced at 473-523 K.

Table 1. Curve fitting results of Rh K-edge EXAFS spectra for $Rh/GeO_2/SiO_2$.

Sample	Scatterer atom	CN[a]	r/nm[b]	ΔE_0/eV[c]	σ/nm[d]	R_f/%[e]
Incipient supported $Rh_6(CO)_{16}$	C_t	2.1	0.277	0.8	0.0054	5.6
	C_b	2.0	0.277	0.8	0.0054	
	Rh	2.8	0.280	0.9	0.0059	
reduced at 423 K	Rh	7.4	0.266	-9.0	0.0085	1.8
reduced at 523 K	Rh	7.5	0.266	-9.1	0.0085	1.8
reduced at 623 K	Rh	3.7	0.268	-6.6	0.0074	0.9
	Ge	0.9	0.241	-5.9	0.0049	
reduced at 723 K	Ge	3.5	0.244	-5.8	0.0086	2.5

a: coordination number, b: bond distance, c: difference in the origin of photoelectron energy between the reference and the sample, d: Debye-Waller factor, e: residual factor.

Table 2. Curve fitting results of Ge K-edge EXAFS spectra for $Rh/GeO_2/SiO_2$.

Reduction temperature/K	Scatterer atom	CN[a]	r/nm[b]	ΔE_0/eV[c]	σ/nm[d]	R_f/%[e]
723 K	Rh	0.7	0.243	-3.9	0.0099	10.7

a: coordination number, b: bond distance, c: difference in the origin of photoelectron energy between the reference and the sample, d: Debye-Waller factor, e: residual factor.

Table 3. Curve fitting results of Rh K-edge EXAFS spectra for $Rh/GeO_2/SiO_2$ reduced at 723 K and exposed to 2.7 kPa NO, followed by evacuation at rt.

Scatterer atom	CN[a]	R/nm[b]	ΔE_0/eV[c]	σ/nm[d]	R_f/%[e]
O	1.2	0.200	5.0	0.0126	
Rh	2.3	0.267	-12.4	0.0095	0.5
Ge	0.7	0.241	-9.4	0.0088	

a: coordination number, b: bond distance, c: difference in the origin of photoelectron energy between the reference and the sample, d: Debye-Waller factor, e: residual factor.

Chapter 5 General Conclusions

To develop the chemistry of atomic layer oxide and apply to catalyst is a challenging task because it is a relatively new material and it possesses several advantages over previous catalyst support. I have tried to use the monolayer oxide to the metal support to achieve the following tasks. First, to investigate the interaction of support surface and metal. The interest was mainly directed to the structural change of support surface which has not sufficiently exploited so far, because atomic layer oxide is especially suitable for structural investigation with EXAFS spectroscopy. Second, to elucidate the characteristic feature of monolayer oxide which cannot find out on bulk oxide support. And finally, making good use of the character of monolayer oxide, to apply to the actual catalytic reactions.

For the achievement of above purpose, I have studied the Ge oxide deposited on silica for catalyst support. Ge and Si belong to the same group in periodic table, thus GeO_2 was considered to be a good candidate as a substitute of the outermost layer of silica surface. Deposition of GeO_2 was carried out by chemical reaction between $Ge(OMe)_4$ and isolated hydroxyl groups on silica surface. Characterization of the synthesized Ge oxide (GeO_2/SiO_2) with FT-IR, XRD and EXAFS spectroscopies gave several evidences for submonolayer deposition of GeO_2. They were the deposition manner of GeO_2 obtained from IR measurement of OH groups on GeO_2 and SiO_2, the disappearance of diffraction line in XRD measurement and the extreme reduction of Ge-Ge bond intensity observed in EXAFS spectra. Ge loading reached by excess $Ge(OMe)_4$ and silica was 7.4 wt% which corresponds to the 1/5 of the full-monolayer coverage. It was difficult to obtain GeO_2 monolayer with full coverage over silica surface, because the repeated reaction and calcination of $Ge(OMe)_4$ results the growth of GeO_2 with layer-by-layer fashion. The local structure around Ge in GeO_2/SiO_2 was similar to the hexagonal type GeO_2, the structure was similar to silica in that it has tetrahedral coordination of oxygen around germanium.

Then the Rh was deposited on GeO_2/SiO_2 to study how the GeO_2 submonolayer is perturbed

through interaction with deposited Rh. It was reported in chapter 3. The observed phenomenon was RhGe alloy formation during reduction at high temperature, as confirmed by XAFS measured from both elements. For the formation of alloy state, the reduction of GeO_2 to metal Ge is necessary. It was considered to be brought from the existence of Rh particle, probably it plays a role for dissociation of hydrogen and supplies spillover hydrogen to the surface of GeO_2/SiO_2 because no change was observed without Rh. Though a part of GeO_2 submonolayer was intruded to the alloy, the other part of Ge oxide retains its submonolayer structure. Such a structural information could not be captured on bulk-oxide used catalyst, because of the existence of inner part of the oxide. Though, the above RhGe alloy formation was also mensurable from metal, i.e. Rh side, interesting behavior was observed on GeO_2 submonolayer support side. That is the reversible behavior of Ge between reduction and calcination steps. Ge migrated from GeO_2/SiO_2 to form RhGe alloy during reduction, and the Ge alloyed with Rh came back onto SiO_2 surface by calcination of the alloy. Volatile GeO was supposed to be the correlated with the phenomenon. The reversibility was also observed between RhGe alloy and Rh oxide during repeated oxidation and reduction treatments, which was confirmed from EXAFS, FT-IR spectra of adsorbed CO, adsorption amount of CO and particle size measurement with transmission electron microscopy. The above RhGe alloy formation was supposed to be classifiable to the SMSI effect.

For comparison, similar experiments were also conducted on Rh supported on bulk-GeO_2. Though alloy formation was also observed on it, not only the support surface but the inner part of the support was involved to the alloy formation. Therefore, different from $Rh/GeO_2/SiO_2$, it was difficult to directly extract the restricted information on support surface which interacts with Rh, even from the EXAFS measurement from Rh side. Although GeO_2/SiO_2 oxide could not be a simple substitute of GeO_2 support, specific characters of GeO_2/SiO_2 became clear from the comparison with bulk-GeO_2. One of the character of GeO_2/SiO_2 is the reversible behavior of Rh and Ge. Because RhGe alloy formation was irreversible on bulk-GeO_2 as proved by the FT-IR measurement of adsorbed CO on Rh. The reason is the dissolution of Rh into the support. The

origin of the difference was attributed to the difference in the structure and resistibility of Ge oxide to reduction on GeO_2/SiO_2 compared to bulk-GeO_2, which comes from the bond formation between Ge and support.

Finally, I have tried to use the monolayer oxide as catalyst support and find out a catalytic reaction where specific character of monolayer can be applicable. The combined experiments of $Rh/GeO_2/SiO_2$ with Rh/GeO_2, Rh/SiO_2 and $Rh/c\text{-}GeO_2/SiO_2$ showed the significance of submonolayer GeO_2 support to the selective formation of ethanol in the hydrogenation of ethyl acetate. To assign the active structure, structural change of $Rh_6(CO)_{16}$ on GeO_2/SiO_2 support was followed by XAFS measurement. The structure could be classified to three groups according to the reduction temperature, they are, $Rh_6(CO)_{16}$ structure, Rh metal particle formation by partial desorption of CO, and RhGe alloy formation. The most active structure was $Rh/GeO_2/SiO_2$ reduced at 423 K, where Rh metal was supported on GeO_2/SiO_2. The reaction proceed via hydrogenation of dissociated species of ethyl acetate on GeO_2 submonolayer. The beneficial character of submonolayer GeO_2 was applied to the reaction in that the Rh metal could be stably loaded on the support under reaction conditions and it could directly participate in the reaction.

In this thesis, I have opened the way to understand the structural change of support surface, using monolayer support. In addition, this study revealed the several novel aspects of monolayer oxide and exemplified the advantageous catalytic reaction for the good use of monolayer oxide as catalyst support and possibility to develop the new class "monolayer catalyst".

Acknowledgements

I would like to express my gratitude to Professor Yasuhiro Iwasawa of the University of Tokyo, whose detailed, helpful advise and discussions led me to the work of this thesis.

I would like to thank Dr. Kiyotaka Asakura, for his warm-hearted and proper advise and direction to me on XAFS measurement in KEK and discussion for so many hours. Without him, I would hardly continue this work in the laboratory.

I want thank to Dr. Nobuyuki Ichikuni of University of Chiba, who is the graduate of this laboratory, for measurement of transmission electron microscopy of so many samples and helpful discussion for the photographs.

I am deeply grateful to Kiyoshi Isobe at the Institute for Molecular Science, who gave me quite proper advice when I was troubled in the synthesis of Rh dimer complex.

I wish to thank the staffs of this laboratory, namely , Dr. Hiroshi Onishi, Dr. Takehiko Sasaki and Dr. Ken-ichi Fukui, whose valuable question and indication stimulated me, especially in the period of preparation for oral examination.

Finally, I am appreciate to all colleagues and graduates of Iwasawa Laboratory during my master and doctor course. I could enjoy my life in the laboratory with them.

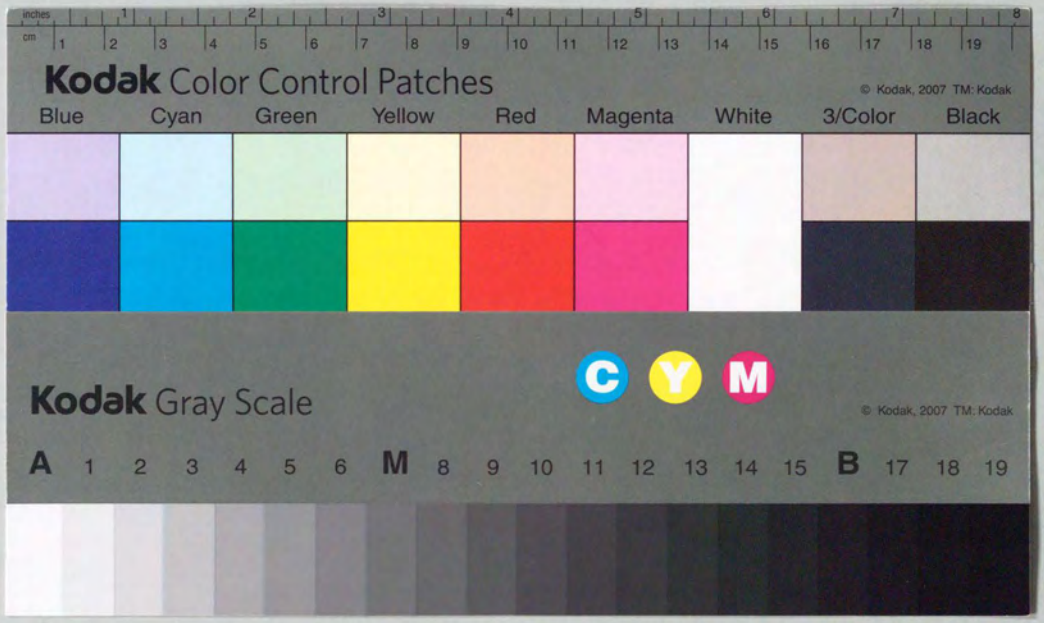
inches
cm
Kodak Color Control Patches
© Kodak, 2007 TM: Kodak
Blue
Cyan
Green
Yellow
Red
Magenta
White
3/Color
Black
Kodak Gray Scale
C
Y
M
© Kodak, 2007 TM: Kodak
A 1 2 3 4 5 6 M 8 9 10 11 12 13 14 15 B 17 18 19